TURUN
YLIOPISTO
UNIVERSITY
OF TURKU

FUNCTIONAL DISULFIDE MACROCYCLES FROM DYNAMIC COMBINATORIAL LIBRARIES

Yonglei Lyu

TURUN YLIOPISTON JULKAISUJA – ANNALES UNIVERSITATIS TURKUENSIS
SARJA – SER. AI OSA – TOM. 723 | ASTRONOMICA – CHEMICA – PHYSICA – MATHEMATICA | TURKU 2024

TURUN
YLIOPISTO
UNIVERSITY
OF TURKU

FUNCTIONAL DISULFIDE MACROCYCLES FROM DYNAMIC COMBINATORIAL LIBRARIES

Yonglei Lyu

TURUN YLIOPISTON JULKAISUJA – ANNALES UNIVERSITATIS TURKUENSIS
SARJA – SER. AI OSA – TOM. 723 | ASTRONOMICA – CHEMICA – PHYSICA – MATHEMATICA | TURKU 2024

University of Turku

Faculty of Science
Department of Chemistry
Chemistry
Doctoral Programme in Exact Sciences

Supervised by

Doctor, Jianwei Li
MediCity Research Laboratory
University of Turku
Turku, Finland

Professor, Tuomas Lönnberg
Department of Chemistry
University of Turku
Turku, Finland

Reviewed by

Professor, Leonard Prins
Department of Chemical Sciences
University of Padova
Padova, Italy

Associate Professor, Rienk Eelkema
Department of Chemical Engineering
Delft University of Technology
Delft, The Netherlands

Opponent

Professor, Riina Aav
Department of Chemistry and Biotechnology
Tallinn University of Technology
Tallinn, Estonia

ISBN 978-951-29-9830-2 (PRINT)
ISBN 978-951-29-9831-9 (PDF)
ISSN 0082-7002 (Print)
ISSN 2343-3175 (Online)
Painosalama, Turku, Finland 2024

UNIVERSITY OF TURKU
Faculty of Science
Department of Chemistry
Chemistry
YONGLEI LYU: Functional Disulfide Macrocycles from Dynamic Combinatorial Libraries
Doctoral Dissertation, 137 pp.
Doctoral Programme in Exact Sciences
August 2024

ABSTRACT

Dynamic combinatorial chemistry (DCC) is an ideal tool used to create complex chemical systems, where a variety of components are produced in a combinatorial way by linking building blocks through reversible chemical bonds under thermodynamic control. When changing experimental conditions or adding templates in the library, the equilibrium is shifted, while some specific components that may have non-covalent interactions with the template will be selected and amplified. The dynamic nature of DCC makes it suitable for exploring new functional molecules, such as catalysts, receptors, drug discovery, and materials.

In this thesis, several building blocks were synthesized for preparing functional macrocycles through DCC. In part 1, a molecular mutualistic relationship was found in a library containing three kinds of building blocks. Thermodynamic and kinetic analysis revealed the details of the emergence of mutualism in the library.

In part 2, a building block containing an arginine group was synthesized, which could self-synthesize into macrocycles, and then assemble with doxorubicin and siRNA to form nanoparticles. The macrocyclic delivery system with high drug loading capacity showed pH- and redox-responsiveness for the release. In addition, the macrocyclic delivery system exhibited good biocompatibility, enhanced cellular uptake ability, and synergistic therapeutic effects against cancer cells.

In part 3, an azobenzene-based building block was synthesized, which could self-synthesize into dimeric macrocycles, and then self-assemble with a bolaform surfactant to form supramolecular hydrogel. The hydrogel demonstrated thermal sensitivity and self-healing capability, and could be processed into the humidity-responsive films with considerable mechanical strength. A series kind of actuators that could programmable move triggered by humidity variation were designed. In addition, a new type of autonomous energy transducer was prepared that could transduce mechanical energy into electricity continuously.

KEYWORDS: Dynamical combinatorial chemistry, macrocycle, catenane, drug delivery, smart materials

TURUN YLIOPISTO
Matemaattis-luonnontieteellinen tiedekunta
Kemian laitos
Kemia
YONGLEI LYU: Funktionaaliset disulfidimakrosyklit dynaamisista kombinatorisista kirjastoista
Väitöskirja, 137 pp.
Eksaktien tieteiden tohtoriohjelma
tohtoriohjelma
Elokuu 2024

TIIVISTELMÄ

Dynaaminen kombinatorinen kemia (DCC) on ihanteellinen työkalu monimutkaisten kemiallisten järjestelmien luomiseen, joissa erilaisia komponentteja tuotetaan kombinatorisella tavalla yhdistämällä rakennuspalikoita palautuvien kemiallisten sidosten avulla termodynaamisen ohjauksen alaisena. Kun muutetaan koeolosuhteita tai lisätään templaatteja kirjastoon, tasapaino siirtyy, kun taas jotkin tietyt komponentit, joilla voi olla ei-kovalenttisia vuorovaikutuksia templaatin kanssa, valitaan ja vahvistetaan. DCC:n dynaaminen luonne tekee siitä sopivan uusien funktionaalisten molekyylien, kuten katalyyttien, reseptoreiden, lääkekehityksen ja materiaalien, tutkimiseen.

Tässä opinnäytetyössä syntetisoitiin useita rakennuspalikoita funktionaalisten makrosyklien valmistamiseksi DCC:n kautta. Osassa 1 löydettiin molekylaarinen vastavuoroinen suhde kirjastosta, joka sisälsi kolmenlaisia rakennuspalikoita. Termodynaaminen ja kineettinen analyysi paljasti yksityiskohtia keskinäisyyden syntymisestä kirjastossa.

Osassa 2 syntetisoitiin arginiiniryhmän sisältävä rakennuspalikka, joka pystyi syntetisoimaan itsensä makrosykleiksi ja sitten koota doksorubisiinin ja siRNA:n kanssa nanohiukkasten muodostamiseksi. Makrosyklinen annostelujärjestelmä, jolla oli korkea lääkelatauskapasiteetti, osoitti pH- ja redox-vastetta vapautumiselle. Lisäksi makrosyklisellä jakelujärjestelmällä oli hyvä biologinen yhteensopivuus, parantunut solujen vastaanottokyky ja synergistiset terapeuttiset vaikutukset syöpäsoluja vastaan.

Osassa 3 syntetisoitiin atsobentseenipohjainen rakennuspalikka, joka pystyi itsesyntetisoimaan dimeerisiksi makrosykleiksi ja sitten koota itsekseen bolaform pinta-aktiivisen aineen kanssa supramolekyylisen hydrogeelin muodostamiseksi. Hydrogeeli osoitti lämpöherkkyyttä ja itsekorjautumiskykyä, ja se voitiin työstää kosteudelle herkäksi kalvoksi, jolla oli huomattava mekaaninen lujuus. Suunniteltiin sarja toimilaitteita, jotka pystyivät ohjelmoitavasti liikkumaan kosteuden vaihtelun laukaisemana. Lisäksi valmistettiin uudenlainen autonominen energiaanturi, joka pystyi muuttamaan mekaanista energiaa sähköksi jatkuvasti.

KEYWORDS: Dynaaminen kombinatorinen kemia, makrosykli, katenaani, lääkeannostelu, älykkäät materiaalit

Table of Contents

Abbreviations

Arg-NH_2	arginine amide
CTAB	cetyltrimethylammonium bromide
CLSM	confocal laser scanning microscopy
COSY	correlation spectroscopy
DCM	dichloromethane
DIPEA	N,N-diisopropylethylamine
DLS	dynamic light scattering
DMSO	dimethyl sulfoxide
DMF	dimethylformamide
DOSY	diffusion ordered spectroscopy
DOX	doxorubicin
DSC	differential scanning calorimetry
ECL	enhanced chemiluminescence
EDC·HCl	N-(3-dimethylaminopropyl)-N′-ethylcarbodiimide hydrochloride
ESI	electrospray ionization
EtOH	ethanol
FA	formic acid
FAM	6-carboxyfluorescein-aminohexyl phosphoramidite
FC	flow cytometry
FE-SEM	field emission scanning electron microscopes
FITC	fluorescein isothiocyanate
FT-IR	fourier-transform infrared spectroscopy
HCl	hydrochloric acid
HOBt	1-hydroxybenzotriazole hydrate
HPLC	high-performance liquid chromatography
H_2O_2	hydrogen peroxide
GSH	glutathione
LC-MS	liquid chromatography-mass spectrometry
MeCN	acetonitrile
MeOH	methanol
MTT	3-(4,5-dimethylthiazol-2-yl)-2,5-diphenyl tetrazolium bromide

NHS	N-hydroxysuccinimide
NMR	nuclear magnetic resonance
NOESY	nuclear overhauser effect spectroscopy
PBS	phosphate-buffered saline
PDA	photodiode array
P-gp	P-glycoprotein
PI	polyimide
PTFE	polytetrafluoroethylene
PVDF	polyvinylidene fluoride
PXRD	powder X-ray diffraction
Q-TOF	Quadrupole Time of Flight
RH	relative humidity
RP	reversed phase
SDS-PAGE	sodium dodecyl sulfate-polyacrylamide gel electrophoresis
siRNA	small interfering RNA
TEM	transmission electron microscopy
TLC	thin-layer chromatography
TEA	triethylamine
TES	triethylsilane
TFA	trifluoroacetic acid
UV	ultra-violet

List of Original Publications

This dissertation is based on the following original publications, which are referred to in the text by their Roman numerals:

I **Lyu, Y.**, Hu, Y., Yang, J., Wang, X., Li, J. Mutualistic Synthesis from Orthogonal Dynamic Covalent Reactions. *Angew. Chem. Int. Ed*. **2024**, e202412020.

II **Lyu, Y.**, Wu, X., Papageorgiou, A. C., Yang, J., Wang, X., Qi, D., Li, J. Dynamic covalent macrocycles co-delivering genes and drugs against drug-resistant cancer. *Cell Reports Physical Science.* **2022**, 3, 101150.

III **Lyu, Y.,** Wu, X., Yang, J., Wang, X., Li, J. Protocol for preparing dynamic covalent macrocycles for co-delivering genes and drugs to cancer cell lines. *STAR Protocol.* **2023**, 4, 102350.

IV **Lyu, Y.**, Yang, J., Shi, X., Weinberger, C., Papageorgiou, A. C., Yu, J., Zeng, H., Tiemann, M., Li, J. Self-Assembly of Phase-Separated Droplets into Ultrasensitive Actuators with Cell-Like Compartments. Submitted.

1 Introduction

1.1 Dynamic combinatorial chemistry

1.1.1 Definition

Combinatorial chemistry is a powerful tool that generates a very large number of different compounds by a collection of small molecules (building blocks).[1] In the combinatorial approach[2] (Figure 1), the selection of those compounds with specific desired properties could be achieved effectively. Compared with traditional chemistry, combinatorial chemistry increases the generating diversity of functional molecules in a controlled setting, and it is widely applied in drug discovery[3] or catalysis development.[4,5]

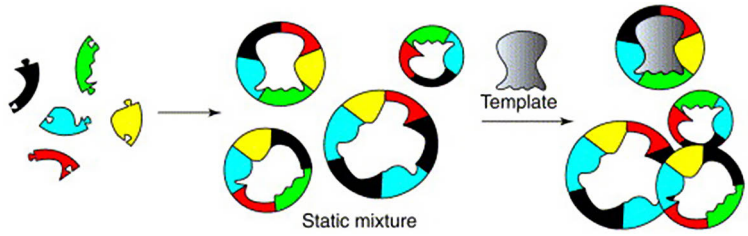

Figure 1. Combinatorial library made from different building blocks. The final composition of the library is fixed. Reprinted with permission from *Drug Discovery Today* **2002,** 7 (2), 117-125.

Dynamic combinatorial chemistry (DCC),[6,7] also known as constitutional dynamic chemistry (CDC),[8,9] is a field of combinatorial chemistry, where simple molecular building blocks can react with each other to form complex compounds in a reversible chemical process under thermodynamic control. In a dynamic combinatorial library (DCL), all the constituents can interconvert due to the existence of reversible covalent or non-covalent bonds between the building blocks. The distribution of constitutes in a DCL tends toward the thermodynamic minimum of the whole system, known as thermodynamic equilibrium. When a DCL is exposed to external influences, the composition will be reorganized, and the equilibrium will

shift to maximize the overall thermodynamic stability of the system by changing the composition of the library in favor of members that are best adapted to the new conditions (Figure 2).[6,10]

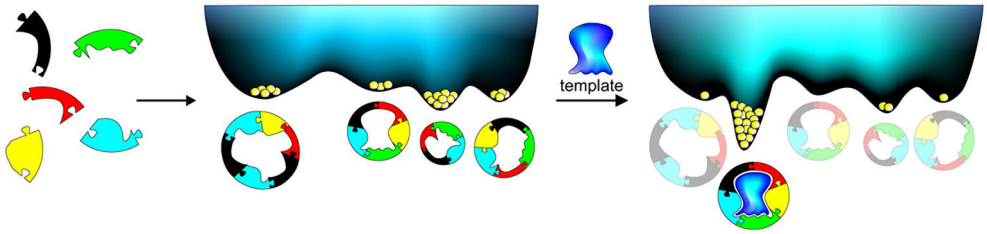

Figure 2. Dynamic combinatorial library made from different building blocks. The distribution of the library compositions depends on the free energy landscape of the library and can be altered by the addition of an external template. Reprinted with permission from *Science* **2002,** 297 (5581), 590-593.

1.1.2 Template effect

1.1.2.1 External template

The state of a DCL is influenced by various external factors, such as temperature,[11] pH,[12] pressure,[11] or molecules[10] of the system. Following a stimulus, the equilibrium of a DCL can be altered until a new distribution of composition with the lowest energy emerges. Among these external factors, the most widely explored strategy for changing the distribution of thermodynamic products in DCLs is to introduce chemical molecules that can strongly bind with building blocks through reversible interactions, including hydrogen bonding,[13] metal-ligand coordination,[14] and electrostatic interaction[15]. For example, when a new species is added to the system, the equilibrium is shifted by the interaction between this template molecule and a specific member in the library, resulting in an increased concentration of the selected species, commonly referred to as "amplification".[16,17] This effect has been utilized to discover receptors and ligands for metal ions[18,19] or biomolecules[20,21] in previous works. It should be noted that, since the equilibrium of DCLs is governed by the lowest overall Gibbs energy, the final distribution is determined by the total sum of the thermodynamic stabilities of all components in the library, rather than the individually most stable one.[16,17,22]

1.1.2.2 Internal template

Templating effects may also arise from internal changes in the DCLs, which is called internal templating. It means that molecular interactions occur between or within the components in the library. If the intramolecular non-covalent interactions occur inside an oligomer, it can be stabilized and amplified to generate a foldamer[23]or supramolecular oligomer assembly[24] (Figure 3). Also, the constitutions in the library can bind intermolecularly and tend to self-assemble into fiber-like assemblies, which result from the self-replication of specific members that can take part in self-assembly.[25,26]

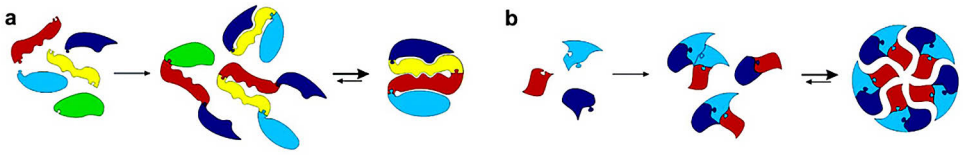

Figure 3. Internal recognition mechanism in DCLs. (a) folded structure formation by intramolecular recognition; (b) self-templating by intermolecular interaction. Reprinted with permission from *Chem. Rev.* **2006,** *106* (9), 3652-3711.

1.2 Reversible chemistry used in DCC

1.2.1 Reactions involving covalent bonds

Compared with traditional combinatorial chemistry, the main feature of DCC is to utilize reversible reactions to mediate the exchange of building blocks between different members in DCLs.[1] For the purpose of exploring novel functional compounds, such as macrocyclic receptors or ligands for small or biomolecules, the experimental conditions of reversible reactions used in DCC including pH and solvent, should be suitable for the selection process between the template and components in the library. Also, a reasonable timescale of the applied reversible reaction is necessary, so that the libraries could respond to external stimuli, and reduce the risk of irreversible side reactions.[6] In addition, the reactions should be carried out under experimental conditions that are compatible with the non-covalent interactions between template and DCL members.[6] Besides, the reversible reactions should be able to be turned off, so that the selection library members can be characterized and isolated for further applications. Scheme 1 summarizes the most popular reversible reactions used for DCC. Here, we only described disulfide exchange and hydrazone exchange, which are used in the experimental part.

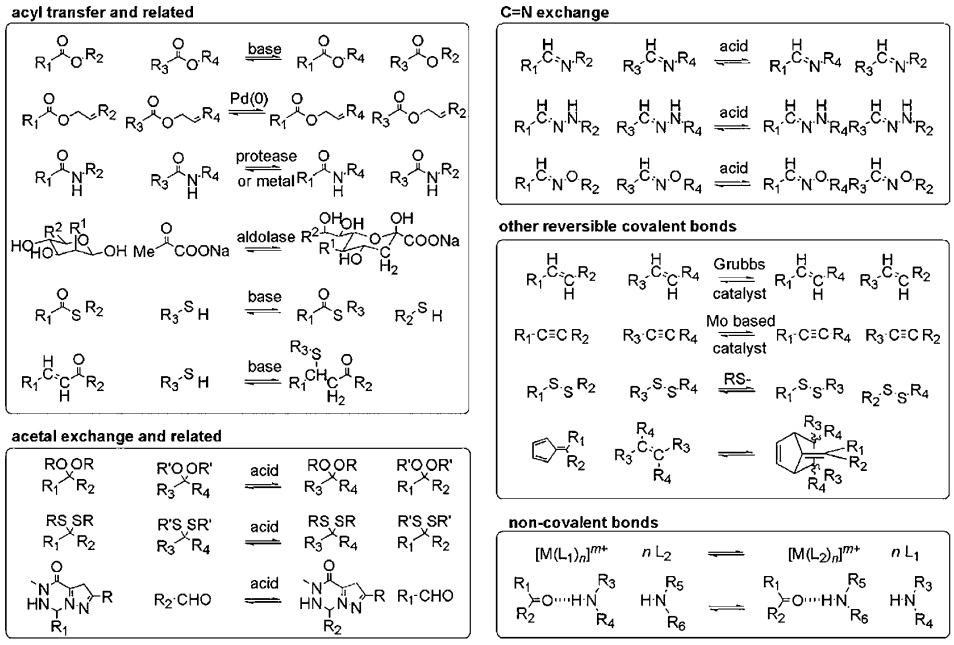

Scheme 1. Overview of reversible reactions utilized in DCC. Reprinted with permission from *Chem. Rev.* **2006,** 106 (9), 3652-3711.

1.2.1.1 Disulfide exchange

Disulfide exchange is one of the most popular reversible reactions employed in the creation of such library members in DCC.[6] In 2000, Sanders's group reported the first example of DCLs containing a large number of disulfide macrocycles synthesized from a variety of simple dithiol building blocks in solution.[27] The essence of the disulfide exchange mechanism involves four steps (Scheme 2):[6,28] the initial ionization of the thiol building blocks to the thiolate anions; the irreversible oxidation of the thiol building blocks into disulfide bond linkage; followed by the oxidation, nucleophilic attack of the thiolate anion on the disulfide bond, resulting in the replacement of one sulfur atom from the disulfide linkage. Since the ionization, oxidation, and exchange reaction are highly pH-dependent in solution, the neutral to mildly basic atmosphere is suitable to generate thiolate anions to be involved in the exchange process. Also, the disulfide exchange reaction can be slowed down after fully oxidizing the thiols to disulfides. Besides, the disulfide exchange process can be "frozen" by lowering the pH, resulting from the protonation of the thiolate anion.

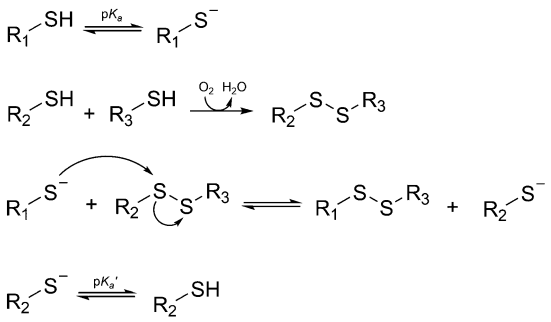

Scheme 2.Mechanism of disulfide formation and disulfide exchange.

1.2.1.2 Hydrazone exchange

Compared with most common imine formation, hydrazones can be more stable and less prone to hydrolysis under neutral conditions in water, because of the mesomeric effect.[29] Hence, hydrazone exchange has become a widely used reversible reaction in dynamic libraries recently, which is the condensation of a hydrazide and an aldehyde. The scheme of hydrazone exchange includes two steps (Scheme 3). In the initial step, a hydrazone is formed through the condensation of an aldehyde and a hydrazide. Then, the carbonyl carbon from the hydrazone group is attacked by a hydrazide group through nucleophilic substitution. The hydrazone reactions become significant under acidic conditions (pH 4 or below) when the aldehyde and the nitrogen atom of the C=N bond become protonation. Alternatively, nucleophilic catalysts such as aniline can be used to accelerate the formation and exchange of hydrazones in DCC.[20,30] It is noticeable that as parent hydrazone is too stable for dynamic libraries, most of the applications in DCC are acyl hydrazone in which the acyl groups moderate the stability by somewhat disfavouring electron delocalization through the molecule.[20, 30-32]

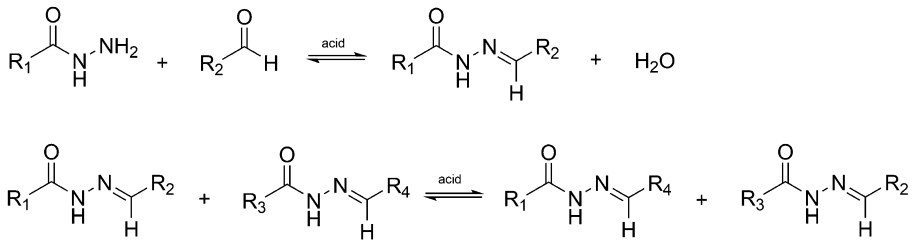

Scheme 3.Mechanism of hydrazone formation and exchange.

1.2.2 Reactions involving non-covalent bonds

Except for the typical covalent reactions, non-covalent bonds (metal-ligand and hydrogen bonding) that take part in the self-assembly of supramolecular architectures have also been exploited in DCC. Timmerman, Reinhoudt, and co-workers first reported a DCL containing hydrogen-bonded assemblies under thermodynamically controlled conditions in 1998.[33] After mixing the individual homomeric assemblies [**1a**]$_3$ and [**1b**]$_3$ in apolar solvents with 5,5-diethylbarbiturate with a ratio of 1:1:2, four different assemblies were formed in the library, which is driven by the formation of 36 cooperative hydrogen bonds (Scheme 4).

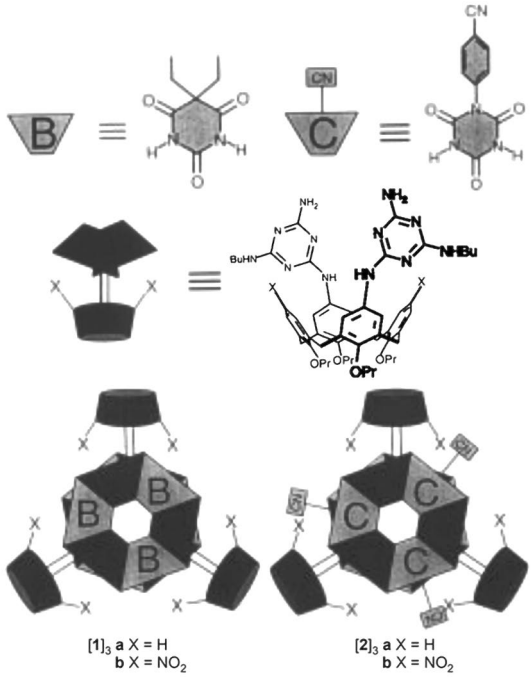

Scheme 4. Schematic representation of hydrogen bonded assemblies [**1**]$_3$ and [**2**]$_3$. Reprinted with permission from *Chem. Commun.*, **1998,** 1021-1022.

To utilize metal-ligand interaction in DCC, the rate of ligand substitution reactions should be fast, which depends on a variety of factors, including the nature of the metal, charge, steric and electronic effect of ligand, and additives.[6] So far, a series of complexes based on Co(II),[34] Ni(II),[35] Pd(II),[36] Ru(II)[37] and Zn(II)[38] ions have been reported to generate DCLs through metal-ligand exchange.

1.3 Application of macrocycles in DCC

1.3.1 Receptor

Making artificial receptors that can bind small molecules through non-covalent interactions still remains challenging, as it needs to devote great effort in design, synthesis, evaluation, optimization, and re-evaluation.[6] Scientists hope to explore an alternative method, and DCC becomes a particularly attractive choice to synthesize receptors, especially macrocyclic receptors. In the mid-1990s, the groups of Sanders,[39] Lehn[40,41] and others[42,43] developed DCC as a novel method to efficiently produce components that can bind target molecules effectively.

Compared with traditional methods for synthesizing macrocyclic receptors, in DCLs the initial di-functional building blocks are self-assembled into the possible macrocycles which are selected to complementary to target molecules (template) under thermodynamic control. Due to the interactions between the template and the components in the library, the preferred members with strong binding will be selected and amplified as a sacrifice of other members. Once the fittest macrocyclic receptors are synthesized and detected in DCLs, they can be either isolated, characterized, or resynthesized by traditional methods. Hence, the main application of DCC is to discover new synthetic receptors for target molecules.

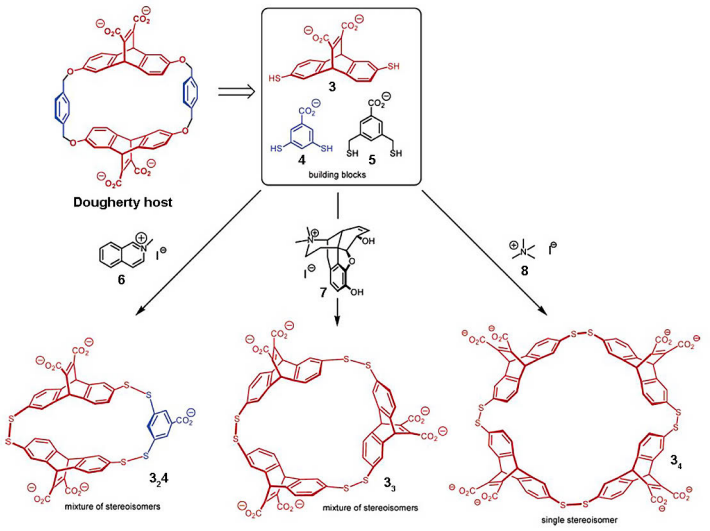

Scheme 5. New receptors were selected and amplified from DCLs containing different dithiol building blocks in presence of ammonium guests. Reprinted with permission from *Chem. Rev.* **2006,** *106* (9), 3652-3711.

Inspired by cyclophane-based macrocycles published by Dougherty and co-workers,[44-46] the group of Sanders and Otto have earlier prepared a series of dithiol building blocks (**3**, **4**, **5**), and analysed the compounds in DCLs in the presence of different ammonium guests (Scheme 5).[47,48] Above expectations, the Dougherty host prefers guest **6**, induce the amplification of a different heterotrimer **9**, rather than analogues of cyclophane host. The binding constant of this disulfide heterotrimer host $\mathbf{3_2 4}$ (2.5×10^5 M^{-1}) was in the same order as the Dougherty host. Besides, when exposed to either the larger guest **7** or smaller guest **8**, the amplification of new receptors in DCLs could happen, and both of them showed high affinities to relative hosts (7.1×10^5 M^{-1} for $\mathbf{7\text{-}3_3}$, 4×10^6 M^{-1} for $\mathbf{8\text{-}3_4}$). In 2019, Waters et al reported a synthetic 5-sided box-like shape receptor capable of selectively recognizing asymmetric dimethylarginine (Rme2a) by using building block **3** and 3,7-dimercapto-naphthalene-2-carboxylic acid via DCC.[49] Using this method, a thioether-linked analogue of the resulting receptor with greater stability was synthesized.

1.3.2 Catalysis

Catalysis is the process of increasing the rate of a chemical reaction by adding a catalyst, which is a substance that speeds up the reaction by lowering the activation energy, making the reactants transform into products easier. To date, several selection-based approaches to discover new synthetic catalysts are being developed. Since the selection of catalysts can be based on the affinity for the transition state of a certain reaction, a stable transition-state analogue (TSA) is designed to mimic how the actual transition state interacts with the catalyst.[50,51]

In DCC, new chemical species are generated by the linkage of small building blocks through reversible reactions under thermodynamic control. When a DCL is exposed to a TSA, the compositions screened for the TSA are stabilized, and the equilibrium of the whole system shifts, resulting in amplifying the strong bind products at the expense of other library members.[6] Based on this approach, DCC can be a fascinating tool in the discovery of synthetic catalysts, as a result, should have the potential to catalysing the corresponding reaction. Sanders, Otto, and co-workers used a library containing building blocks (**3**, **4**, **5**) to search for new catalysts for the Diels-Alder (DA) reaction between acridizinium bromide and cyclopentadiene.[50] In this paper, the product was selected as a TSA, and trimer $\mathbf{3_3}$ was amplified from a library containing equimolar amounts of **3**, **4**, and **5**. After studying the binding of reactants and product to macrocycle $\mathbf{3_3}$, they found that it showed a stronger binding affinity to the product than the cyclopentadiene. Hence, host $\mathbf{3_3}$ should be potential in catalysis. In the kinetic experiments, macrocycle $\mathbf{3_3}$ could accelerate the rate of DA reaction with an approximately 10-fold.

Lehn's group investigated on a co-catalysis strategy of bond-formation, which is achieved by combining metallo- and organo-catalysis in a DCL. In this paper, imine and hydrazone generation from 6-phenyl pyridine-2-carboxaldehyde, *p*-anisidine and N-methyl pyridine hydrazine showed large accelerations in presence of Ag(I) or Zn(II), up to 10^4 for the Zn(II)-(*p*-anisidine)imine complex.[52]

1.3.3 Drug delivery

To improve the delivery and therapeutic efficacy of drugs to specific target sites, a drug system, referred to as a vector/carrier is a technology that has been investigated by researchers in last several decades. A variety of functional delivery systems have been designed, such as polymers,[53,54] liposomes,[55,56] and inorganic nanoparticles,[57,58] among which polymeric carriers are most widely used. However, inefficient release rates and relatively low loading capacity are the main hinders need to overcome for polymer vectors.[59,60] Hence, some researchers have started to explore stable but responsive delivery systems with high drug-loading ability.

In recent years, reversible covalent bonds-based nanomaterials with stimuli-responsive linkers have been used in drug delivery, as they exhibit flexible and responsive exposure to stimuli, while remaining stable under physiological conditions.[61-63] Based on the dynamic features of reversible covalent bonds, some researchers began to design dynamic drug delivery systems directly using DCC. In a DCL, the building blocks can self-synthesize in assemblies or macrocycles linked by reversible bonds under thermal dynamic control, while specific members can be amplified in the presence of an external template. These features can be exploited for designing responsive delivery system.

Our group described a drug delivery system using DCC, in which the octameric disulfide macrocycle was amplified from the dithiol building block **4** after introducing a cationic template and a drug molecule (DOX) during the co-self-assembly process (Figure 4).[64] The resulting nanorods not only showed the extremely high drug loading capability but also could release drug molecules inside the tumor cell rapidly, due to the redox- and pH-responsiveness of disulfide bonds in macrocycles. In addition, the responsive nanorods delivery system exhibited the enhanced ability to fight against DOX-resistant cancer cells both *in vitro* and *in vivo*.

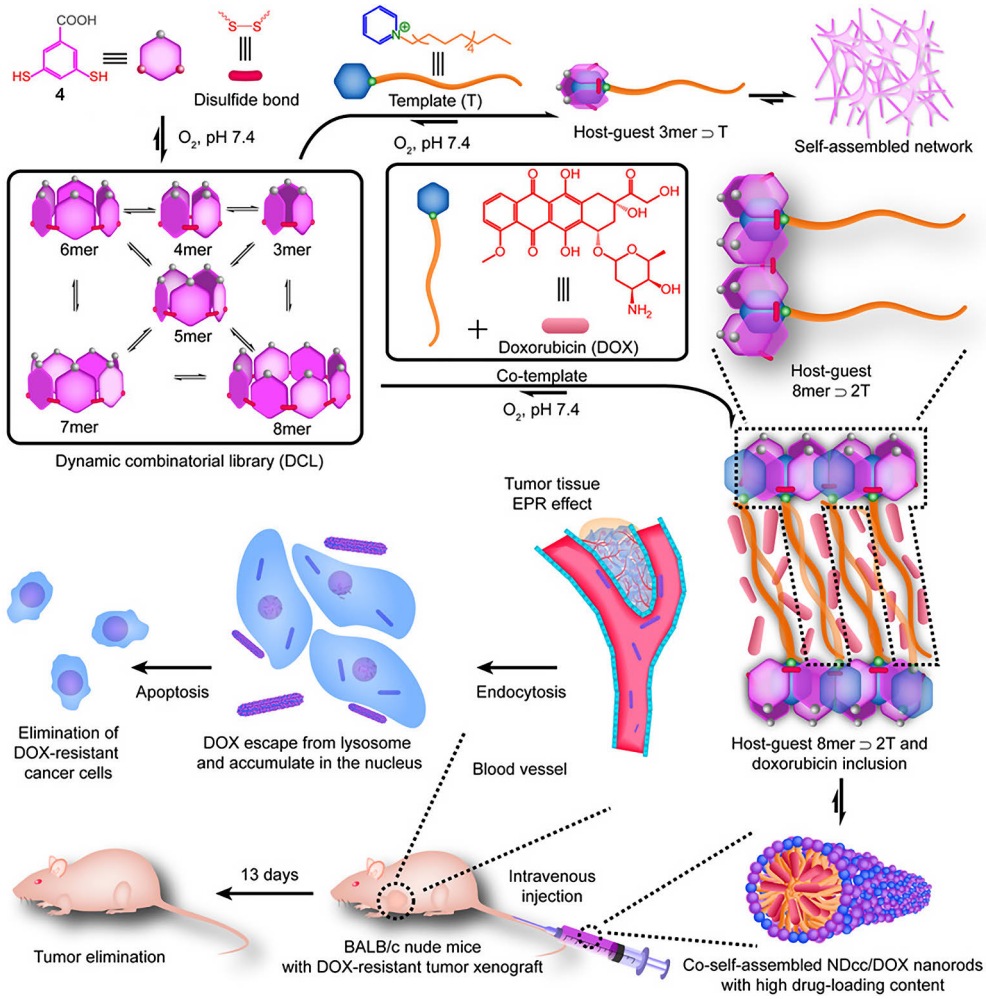

Figure 4. Self-synthesizing nanorods emerging from DCLs against DOX resistant cancer *in vitro* and *in vivo*. Reprinted with permission from *Angew. Chem. Int. Ed.* **2021,** 60 (6), 3062-3070.

1.3.4 Covalent organic frameworks

COFs are two or three-dimensional polymeric materials formed through covalent reactions between organic precursors until porous, stable, and crystalline materials form.[65] Different from classical short-range covalent polymers connected *via* irreversible condensation, COFs show highly ordered crystalline structures through reversible reactions. Because of their well-defined topologies, porous structure, and ease of functionalization, COFs have shown potential in various fields, including catalysis,[66-68] gas storage and separation,[69,70] sensing,[71-73] biomedicine[74,75] and so on.

In 2005, the first two COFs based on dynamic boroxine and catechol/boronate ester linkages were reported by Yaghi and co-workers,[76] a number of distinct COFs architectures have been synthesized. Among these reports, boron-based COFs were the dominant. Dichtel's group utilized a $BF_3{\cdot}OEt_2$-catalysed deprotection protocol to form boronate esters directly from protected catechols and arylboronic acids.[77] Using this method, a crystalline boronate ester-linked COF composed of phthalocyanine macrocycles linked by phenylene bis(boronic acid) linker is fabricated, which has potential in organic photovoltaic devices.[77] Afterward, Yaghi's group successfully synthesized the first crystalline COF-300 linked through imine,[78] followed by COF-42 and COF-43 linked through hydrazone.[79] All these materials were highly crystalline, displayed excellent chemical and thermal stability, and were permanently porous.

Recently, Patra et al succeeded in achieving a transformation of discrete organic imine cage-to-COF film at the liquid-liquid interface directed by dynamic covalent chemistry.[80] After adding aromatic amines linkers, the discrete organic imine cage COF1 in $CDCl_3$ began to unfold and generate imine intermediates, followed by their interface-assisted preorganization and the growth of COF films with high crystallinity and porosity (up to $1790 \pm 80\ m^2g^{-1}$) at interface (Figure 5). Further, the COF films exhibited excellent performance toward the size-selective molecular separation from water and high solvent permeance for polar protic and aprotic solvents.

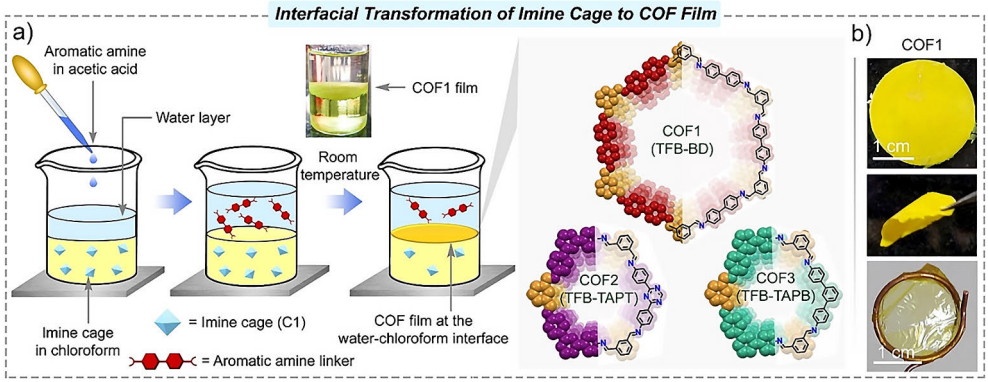

Figure 5. (a) The scheme of acid-catalysed interfacial transformation of the imine cage to COF film in the presence of diverse amine linkers at room temperature. (b) Digital photographs of COF1 films: free-standing film after 24 h of interfacial polymerization (top and middle) and solvent-induced delaminated transparent thin film (bottom). Reprinted with permission from *Angew. Chem. Int. Ed.* **2023,** 62 (23), e202219083.

1.3.5 Soft materials

Soft materials are a class of materials that are deformed or structurally altered by thermal or mechanical stress at about room temperature, as the interactions holding the material together are close to thermal energy, making them reversible and highly responsive to environmental changes. Soft materials include foams, polymers, gels, colloids, and most soft biological materials. There materials are typically composed of individual particles or molecules that are not tightly packed together.

As a branch of soft materials, hydrogel is a three-dimensional network of physically or chemically crosslinked polymers that can entrap and retain a large amount of water.[81,82] Because of the swelling, mechanical, optical, and biocompatible properties, hydrogels have been widely used in biomedicine, food, and industrial materials, etc.[83-85] Different from the polymeric hydrogels made from covalently cross-linked networks of polymers, the network in supramolecular hydrogels is formed due to the non-covalent interactions between the hydrogelators.[82] Recently, researchers found that the self-assembly and self-replication from building blocks into macrocycles through DCC provide an alternative way to form unexpected supramolecular hydrogels.

Otto and coworkers have reported a unique self-replicating model consisting of monodisperse self-assembled nanofibers, which is based on short peptide sequence-derived building blocks that form macrocycles with different sizes.[26] They also found that the length of the fibers could be affected by mechanical agitation or chemical methods, resulting in the production of fibers with controllable lengths and low polydispersity.[86,87] After irradiating the solution containing hexamer fibers with a UV lamp, the hydrogel formed, resulting from disulfide exchange (Scheme 6).[87] Besides, by adding triblock copolymers with negatively charged motifs and salts that can interact with fibers, the mechanical properties of the hydrogel can be tuned precisely.[88]

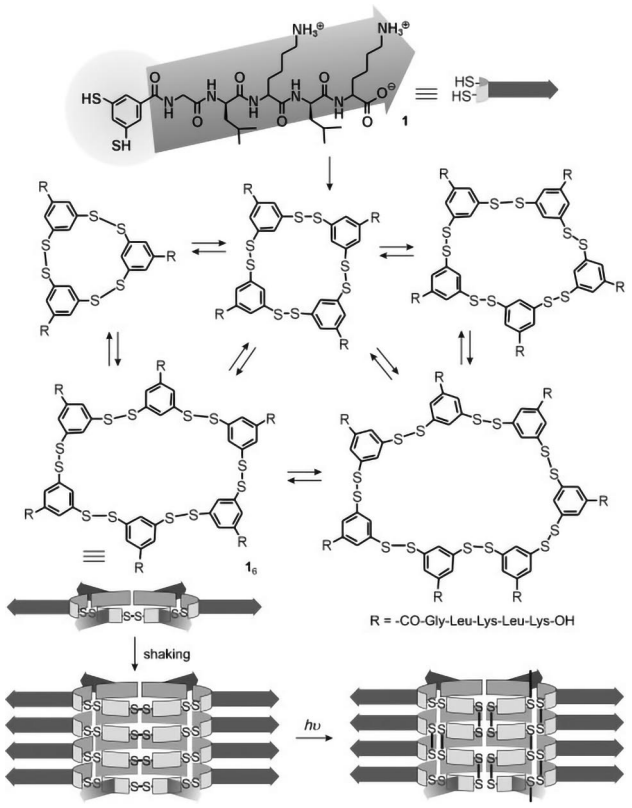

Scheme 6. A DCL made from a short peptide sequence-derived building block gives rise to stacks of hexameric macrocycles which are covalently captured upon photoirradiation (365 nm) to produce a hydrogel. Reprinted with permission from *Angew. Chem. Int. Ed.* **2011,** 50 (36), 8384-8386.

Except the supramolecular hydrogel, some other soft materials have also been found in DCLs. Recently, our group has described a robust and sustainable supramolecular plastic formed by azobenzene-derived macrocycles (**ADM**), which was synthesized from a DCL by a highly selective gelation process with magnesium cation, with cationic surfactant cetyltrimethylammonium bromide (**CTAB**) via liquid-liquid phase separation.[89] The **ADM**/**CTAB** supramolecular material exhibited self-healing properties after absorbing water, while it could be used as an eco-friendly adhesive bonding material in air after releasing water.

2 Aims of the Thesis

Dynamic combinatorial chemistry (DCC) is a method to generate libraries of new molecules or complex structures from simple building blocks through reversible reactions. The library containing these reversibly interconverting components is called a dynamic combinatorial library (DCL), and the distribution of which is determined by the thermodynamic stability of the whole system. When a DCL is exposed to an external stimulus (such as pH, temperature, and specific molecules), the equilibrium will shift and those components whose Gibbs free energy is lowered by interactions can get amplified, allowing the whole library to reach a new equilibrium. Based on these features of DCC, it has been used in identifying ligands and receptors for small or biological molecules and discovering new catalysts for chemical reactions, and it still has the potential to produce functional dynamic macrocyclic molecules in other fields.

This thesis aims to expand the applications of dynamic covalent macrocycles through DCC. In this thesis, several building blocks with specific functional groups are designed to prepare dynamic macrocycle systems through reversible reactions, and some applications are proposed based on their properties.

The aims of this thesis are:

1. To develop a system containing two orthogonal reversible reactions (disulfide exchange and hydrazone exchange) to investigate molecular mutualism, which is the co-synthesis of the minor species in a DCL.

2. To develop a responsive macrocycle-based vector system for co-delivery of the drug and gene to fight against multiple drug resistance (MDR) cancer cells.

3. To produce cell-like compartment embedded supramolecular materials for fabricating smart actuators using dynamic covalent macrocycles.

3 Materials and Methods

3.1 General methods

All the chemicals were purchased from Sigma-Aldrich, TCI, abcr, Fisher Scientific, BLD, or VWR and used without further purification. All the reactions were monitored by thin layer chromatography (TLC) performed on silica gel 60 F_{254} plate (Merck). The synthesis and characterization of novel compounds are described in the original publications.

3.2 Characterization methods

3.2.1 Composition and structure analysis

3.2.1.1 NMR

^{1}H, 2D NMR (COSY, NOESY, DOSY) spectrum of the catenanes or complexes were recorded with deuterium oxide (D_2O) as the solvent, using a Bruker AV500 spectrometer.

3.2.1.2 MS

All ESI-MS spectra of macrocycles or catenanes were performed using a Hybrid-Quadrupole Orbitrap Mass spectrometers (Thermo Scientific) and a micrOTOF-Q (Bruker Daltonics, Bremen, Germany) using direct infusion.

3.2.1.3 HPLC

HPLC analysis of the DCLs was conducted on an Agilent 1100 series HPLC value system equipped with a diode array detector at 254 nm. The separation of the compounds in DCL was performed on a Symmetry C8 column (Waters™) at 25 °C with a gradient mixture of acetonitrile-water (5:95 → 95:5, v/v) with 0.1 % FA (v/v) as the mobile phase; flow rate: 1.0 mL/min.

3.2.1.4 DLS

The size distribution and zeta potential of the nanoparticles or droplets were analysed using a Zetasizer Nano-ZS instrument (Malvern Instruments Ltd., Worcestershire, UK). Each sample was measured three times.

3.2.1.5 UV-Vis

The drug concentration analysis was measured by a Lambda 35 UV/Vis spectrometer (PerkinElmer, U.S.A). The gene concentration analysis was measured by an ND-1000 Spectrophotometer (Thermo Scientific).

3.2.1.6 FT-IR

FT-IR spectrum was recorded using an FTIR-1000 (PerkinElmer, U.S.A) at room temperature. Each sample was recorded with 64 scans from 4000 to 400 cm^{-1} with a resolution of 0.5 cm^{-1}.

3.2.1.7 PXRD

The PXRD spectrum of samples was recorded by using a MicroMax 007 HF X-ray generator equipped with a HyPix-6000HE photon counting detector. The experiments were conducted at Turku Bioscience Centre.

3.2.1.8 CLSM

The morphology of coacervate droplets was observed by CLSM. The samples were stained with Nile red solution, and then dropped in confocal dishes and examined with a Zeiss LSM880 with air scan instrument.

3.2.1.9 TEM

The morphologies of the nanoparticles or droplets were recorded on a JEM-1400 Plus (JEOL Ltd., Japan). The sample was dropped on a carbon film-supported copper grid (size 100 mesh), and then observed after drying in the air.

3.2.1.10 FE-SEM

The surface morphologies of the hydrogels or films were observed by using an Apreo SEM (Thermo Scientific). All the samples were coated with a thin layer (a thickness of 5 nm) of platinum using a sputter coater.

3.2.2 Materials properties measurements

3.2.2.1 DSC

Differential scanning calorimetry (DSC) was performed on a DSC Q2000, TA Instruments differential scanning calorimeter. The calorimetry was operated with a nitrogen flow of 50 cm^3/min. Aluminum crucibles were used for both reference and sample. The measurement was performed from 40 °C to -40 °C at a cooling rate of 5 K/min, and then heating back to 40 °C at a heating rate of 5 K/min.

3.2.2.2 Rheometer

The rheological properties of the hydrogels were conducted on a HAAKE MARS 40 rheometer (Thermo Scientific). The diameter of the parallel plate was 20 mm, and the gap was 1.0 mm. After loading the hydrogel on the plate, silicone oil was covered on the plate to avoid the evaporation of water.

3.2.2.3 Tensile testing

Stress-strain curves of the film were measured by using a homemade tensile tester with a stretching speed of 0.05 mm/s. The thickness of the sample was 20 μm.

4 Results and Discussion

4.1 Molecular mutualistic synthesis in DCC

4.1.1 Introduction

Mutualism is an interaction between individuals of different species that results in beneficial effects on the reproduction or survival of the interacting populations.[90] This concept has been widely understood to operate on levels of ecosystems, organisms, cells, and even molecules.[91] A typical example of molecular mutualism is the relationship between RNA and protein, where RNA carries out protein synthesis in the ribosome and protein (polymerases) catalyses the condensation of nucleotides to make RNA.[92,93] Such cooperative relationships must have influenced prebiotic chemical evolution, which is crucial to exploring the origin of life.

Among hypotheses about the origin of life, "RNA-peptide coevolution" suggests that life may start from these two biopolymers due to their cooperative synergies in biology. [93-97] Inspired by this, their mutualistic functions have been explored in synthetic systems. Lynn et al. ascertained that the recurring pattern of nucleic acid phosphates was a contributing factor to the compatibility, stability, and uniform consistency of the end cross-β formation.[98] Similarly, Williams, Leman, and others have reported the potential for cationic proto-peptides to steer their interactions with RNA molecules, fostering mutual stability.[92] These studies have investigated how peptides could promote folding or functions of RNA,[99-102] while the evidence that can demonstrate how the two molecules originated concurrently is quite few. Pioneers like Sutherland and Powner have shown that precursors to RNA and peptides can be generated by chemical reactions in prebiotic conditions.[103,104] Therefore, to further strengthen this hypothesis from a perspective in synthetic chemistry, it is imperative to explore the potential for the products of two reactions to mutually enhance each other's synthesis.

In the first part of thesis, we designed two DCLs contains three kinds of building blocks, azobenzene-derived dithiol building block **1**, β-cyclodextrin derived aldehyde **CD**, and adipic dihydrazide **L** (Figure 6).[105] These building blocks could take part in two orthogonal reversible chemical reactions, respectively (Scheme 7a - b). When these two libraries were performed together at the same experimental

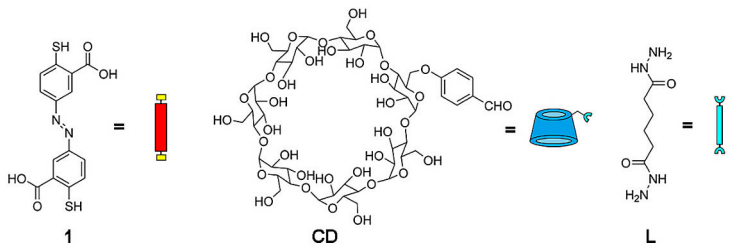

Figure 6. Molecular structure of building blocks **1**, **CD** and **L** in DCLs.

conditions, two species in DCLs that were minor products from the respective DCLs became the major products due to the reduction in Gibbs energy levels arising from the formation of a complex "handcuffs" catenane (Scheme 7c). These results suggested that the two species functioned as templates for each other's co-amplification through noncovalent binding between different libraries, demonstrating a mutualistic relationship in synthesis. Moreover, the inert reaction (hydrazone formation) could be powered on by another active reaction (disulfide exchange) in the pair of orthogonal reactions. Such a reciprocal synthesis stands for a way of coevolution of species in complex chemical systems, shedding some light on the hypothesis of "RNA-peptide coevolution" for the origin of life.

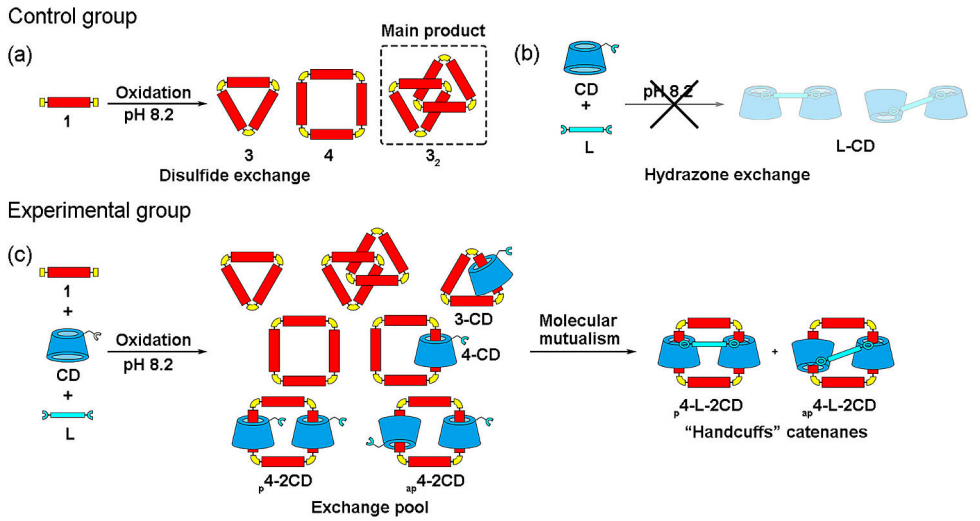

Scheme 7. Schematic illustration DCLs containing a mixture of different compositions. (a) Disulfide exchange (**1**); (b) hydrazone exchange (**1** + **L**); (c) disulfide and hydrazone exchange (**1** + **CD** + **L**).

4.1.2 Experimental Section

4.1.2.1 Synthesis of building block **1** and **CD**

Building block **1** is an azobenzene-derived compound, and its synthetic procedure followed the previous literature.[106] The building block **1** contains two thiol groups that can take part in disulfide exchange, and two carboxylic acid groups for increasing the solubility in solution.

Building block **CD** is mono[6-*O*-(4-formyl-phenyl)]-*β*-cyclodextrin and its synthetic procedure followed the previous reports.[107,108] The building block **CD** contains an aldehyde group that can react with hydrazide to form dynamic hydrazone bond.

4.1.2.2 Coefficients of building block **1** and **CD**

To convert HPLC-UV peak areas into concentration, a series of libraries containing building block **1** were prepared with different concentrations (0, 0.25, 0.5, 1, 1.5, 2 mM) in borate buffer. Then, 20 μL of library samples were diluted with 80 μL of DMSO prior to analysis. The total peak area of the HPLC chromatogram was determined and plotted against the concentration of building block **1**. The slope of the linear fit of the data gave a value for C_1 of 4880.86 mAU·min·mM^{-1}. Using the same method, the coefficient C_2 of building block **CD** was calculated as 3811.06 mAU·min·mM^{-1}. For building block **L**, there was no absorbance at 254 nm in HPLC.

4.1.2.3 Evaluation of equilibrium constants

In the procedure of evaluating equilibrium constants, two sets of DCLs (control group: **1** + **CD**, experimental group: **1** + **CD** + **L**) were set up, with the concentration of building block **1** (1 mM), **CD** (0, 0.5, 1.0, 1.5, 2.0, 2.5, 3.0, 3.5, 4.0 mM), and **L** (0 and 1 mM), respectively. When all the DCLs were fully oxidized and equilibrated, the concentrations of DCL components were determined by HPLC. 20 μL of library samples were diluted with 80 μL of DMSO prior to analysis and the HPLC-UV peak areas of components **3**, **4**, **3$_2$**, **4-2CD**, **4-CD**, **3-CD**, and **4-L-2CD** were integrated using Chemstation software from Agilent.

4.1.2.4 Kinetics of thiol oxidation

To measure the rate of the thiol oxidation model, 2-mercaptobenzoic acid was used. 2-mercaptobenzoic acid was dissolved in borate buffer (50 mM, pH 8.2) at a concentration of 2.0 mM. The thiol oxidation is overall first-order reaction. We

analysed the kinetics based on the reaction **M** → **M₂**, which was measured by using HPLC. The molar absorptivity of thiol **M** was determined as 7253.1 mAU·min·mM^{-1}. The rate constant for the thiol oxidation was then obtained by analysing the change in the concentration of **M** with time.

4.1.2.5 Kinetics of breakage of catenane

To measure the rate of breakage model, catenane **3₂** was used. **3₂** was dissolved in borate buffer (50 mM, pH 8.2) at a concentration of 0.3 mM. We analysed the kinetics based on the reaction **3₂** → 2**3**, which was measured by using HPLC. The molar absorptivity of catenane **3₂** was determined as 29285.2 mAU·min·mM^{-1}. The rate constant for breakage of catenane was then obtained by analysing the change in the concentration of **3₂** with time.

4.1.2.6 Kinetics of thiol-disulfide exchange

To measure the rate of the thiol-disulfide exchange model, we prepared 5-nitro-2-mercaptobenzoic acid **A** and a disulfide molecule **D₂**. **A** and **D₂** were dissolved in borate buffer (50 mM, pH 8.2) at a concentration of 1.5 mM. We analysed the kinetics based on the reaction **A** + **D₂** → **AD** + **D**, which was measured by using HPLC. The peak area of **A** and **D₂** was measured at 254 nm. The molar absorptivity of **A** and **D₂** were determined as 2346.5 mAU·min·mM^{-1} and 3806.3 mAU·min·mM^{-1}, separately. The rate constant for thiol-disulfide exchange was then obtained by analysing the change in the concentration of **D₂** with time.

4.1.2.7 Kinetics of hydrazone formation

To measure the rate of breakage model, **4-2CD** and building block **L** were used. **4-2CD** and **L** were dissolved in borate buffer (50 mM, pH 8.2) at a concentration of 0.4 mM, respectively. We analysed the kinetics based on the reaction **4-2CD** + **L**→ **4-L-2CD**, which was measured by using HPLC. The molar absorptivity of **4-2CD** was determined as 27145.5 mAU·min·mM^{-1}. The rate constant for the hydrazone formation was then obtained by analysing the change in the concentration of **4-2CD** with time.

4.1.3 DCL preparation and analysis of components

A disulfide DCL was prepared from a well-studied azobenzene-derived dithiol building block **1** (1.5 mM) in borate buffer at pH 8.2. After stirring 8 days in the air, the library was analysed by LC-MS. The results showed that building block **1** was fully

oxidised into a dominant product catenane $\mathbf{3_2}$ which was interlocked by two trimeric macrocycles **3**, and two minor species trimer **3** and tetramer **4** (see Figure 7a), corresponding to the previous report.[106] Then, a DCL containing the equivalent amounts of building block **1** and **CD** (1.5 mM) was prepared at the same condition. After fully oxidization, LC-MS showed that three new peaks appeared, which were correspond to catenane **4-2CD** containing a tetrameric disulfide macrocycle interlocked by two aldehyde **CD**s, catenane **4-CD**, and **3-CD** consisting of tetrameric or trimeric disulfide macrocycle but interlocked by one aldehyde **CD**, respectively (Figure 7c, f-h). Besides, a hydrazone DCL was made from the aldehyde building block **CD** (1.5 mM) and an adipic dihydrazide building block **L** (1.5 mM) in the aqueous solution at the same condition (Figure 7b). However, the expected hydrazone product **L-2CD** didn't appear, since the hydrazone formation is thermodynamically and kinetically unfavourable in water at the slightly basic pH.[109-111]

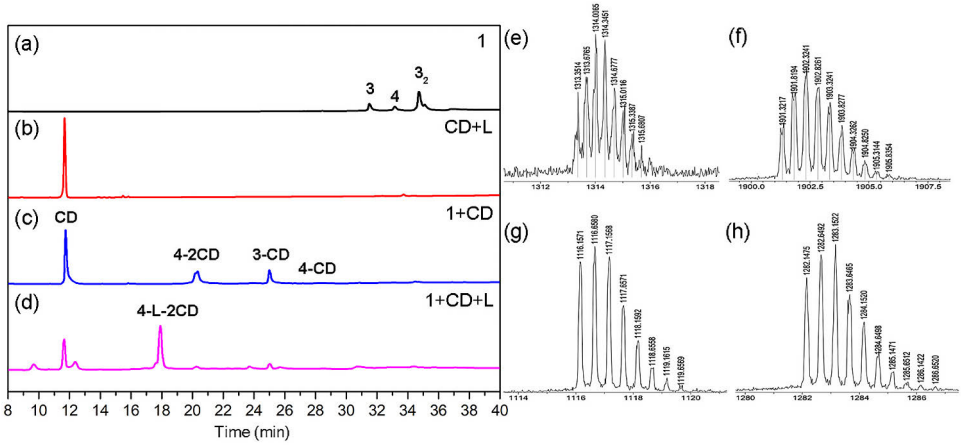

Figure 7. Partial HPLC traces of a DCL composed of (a) 1.5 mM of **1**; (b) 1.5 mM of **CD** and **L**; (c) 1.5 mM of **1** and **CD**; (d) 1.5 mM of **1**, **CD** and **L**; ESI-MS spectrum of (e) **4-L-2CD**, expected m/z for $[\mathbf{4\text{-}L\text{-}2CD}]^{3-}$ = 1313.6120; (f) **4-2CD**, expected m/z for $[\mathbf{4\text{-}2CD}]^{2-}$ = 1902.3766; (g) **3-CD**, expected m/z for $[\mathbf{3\text{-}CD}]^{2-}$ = 1116.6807; (h) **4-CD**, expected m/z for $[\mathbf{4\text{-}CD}]^{2-}$ = 1282.6769.

When the two DCLs were combined together with the same concentration ([**1**] = [**CD**] = [**L**] =1.5 mM) in the same condition (pH 8.2), HPLC analysis showed a new dominant peak appeared, and the MS analysis of this new peak was the sum of that of the disulfide tetramer **4** and that of the linear hydrazone **L-2CD** obtained by the condensation of one molecule of **L** and two molecules of **CD** (Figure 7d and e). Considering that the **CD** could interlock with azobenzene via host-guest interaction in water, the new product peak should be corresponded to a "handcuffs" catenane **4-L-2CD** interlocked by hybrid species, the disulfide **4** and a linear hydrazone **L-2CD**. This

neat production showed that the minor species **4** and **L-2CD** from the respective DCL dominated the complex chemical system when the two libraries were performed together, demonstrating that the **4** and **L-2CD** were a pair of mutualistic molecules.

Due to the remarkable co-amplification of **4** and **L-2CD**, which should be mutually benefited from their binding, the interlocked structure should remain stable during the purification process from the reaction mixture. Hence, we isolated both of **4-2CD** and **4-L-2CD** as a mixture of isomers, including the parallel (head-to-head) and anti-parallel (head-to-tail) conformation[106,112] using preparative HPLC. The interlocked structures **4-2CD** and **4-L-2CD** remain stable enough to be comprehensively characterised by a number of ^{1}H NMR spectroscopic experiments. The DOSY spectrum of **4-L-2CD** showed that both **4** and **L-2CD** had the same diffusion rate constant at 2.795×10^{-10} m^2 s^{-1} (Figure 8b), which confirmed the interlocked structure of **4-L-2CD**. In the ^{1}H NMR spectrum of **4-L-2CD** (Figure 8a), there were four sets of signals (A, B, and C) for tetramer **4**, as the local symmetry of azobenzene was affected by the interlocked **L-2CD**.[113-117] The presence of only one

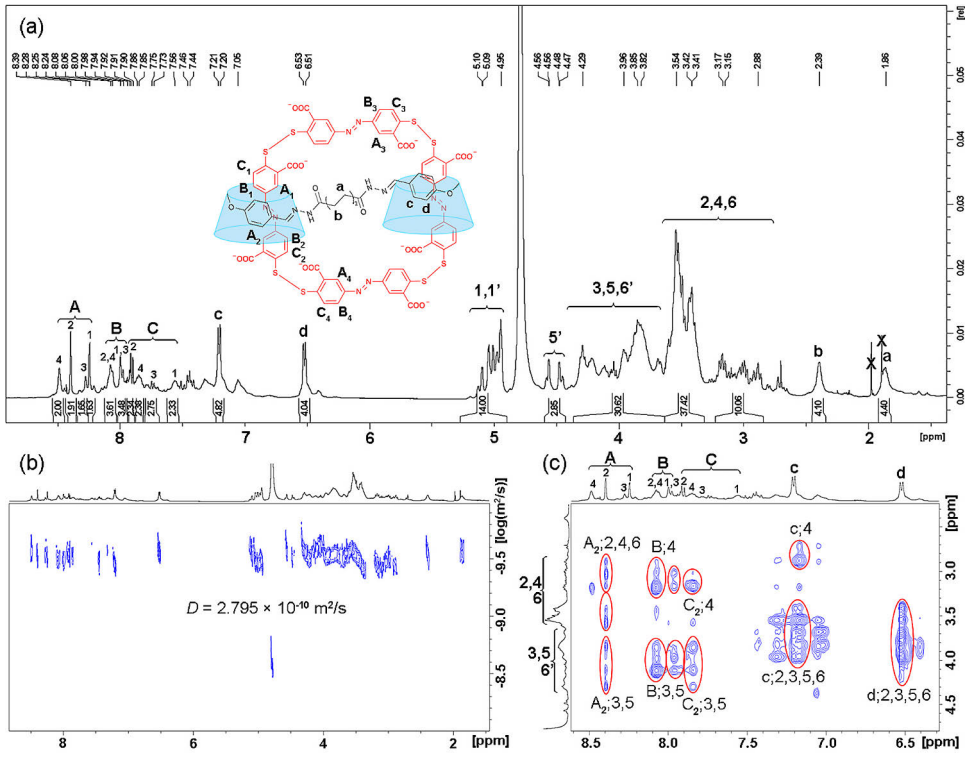

Figure 8. NMR analysis of catenanes **4-L-2CD**. (a) ^{1}H NMR spectra of **4-L-2CD**. (D_2O, pD = 8.2, 500MHz, 298K); (b) the 2D DOSY spectra of **4-L-2CD**. (D_2O, pD = 8.2, 500MHz, 298K); (c) part of 2D ^{1}H-^{1}H NOESY spectra of **4-L-2CD**. (D_2O, pD = 8.2, 500MHz, 298K). Reprinted with permission from *Angew. Chem. Int. Ed.* **2024**, e202412020.

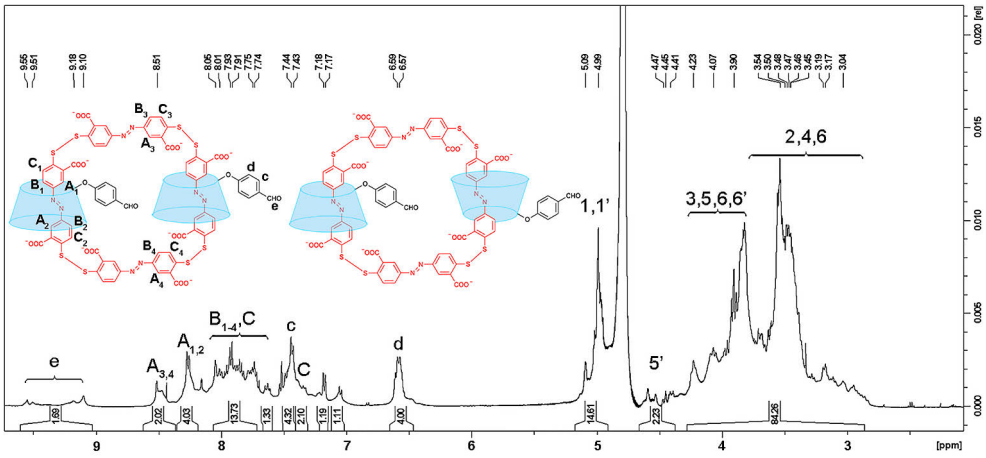

Figure 9. ^{1}H NMR analysis of catenanes **4-2CD** (D_2O, pD = 8.2, 500MHz, 298K). Reprinted with permission from *Angew. Chem. Int. Ed.* **2024**, e202412020.

set of phenyl signals of **L-2CD** at 7.21 and 6.51 ppm was consistent with a symmetrical structure, indicating that the parallel conformation $_{p}$**4-L-2CD** was the dominant product in the mixture.[114] The sharp peaks at 8.24 and 8.39 ppm were assigned to the protons A_1 and A_2 of azobenzene units included inside the **CD**, as they experienced varying degrees of shielding from the **CD** cavity. In the NOESY spectrum (Figure 8c), NOE signals were observed between A_2-3,5,6, B-3,4,5, and C_2-3,4,6, confirming the part of tetramer **4** was mechanically encapsulated in the **CD** cavity in **4-L-2CD**. On the other hand, the ^{1}H NMR spectrum of **4-2CD** showed two sets of phenyl signals of **CD** at 7.44 and 6.59 ppm, indicating two possible isomers, with either a head-to-head or head-to-tail orientation of two **CD**s, have been obtained (Figure 9). Compared with catenanes **4-2CD**, protons c and d on phenyl moieties of **4-L-2CD** were shifted upfield (from δ = 7.44 to 7.21 ppm for c and from δ = 6.59 to 6.51 ppm for d), due to the formation of hydrazone bonds. Besides, some small peaks appeared at 7.05 and 6.41 ppm, which had NOE signals with the **CD** cavity. These may be attributed to the protons of the phenyl group in anti-parallel conformation $_{ap}$**4-L-2CD**.[105]

4.1.4 Determination of equilibrium constants of catenanes

4.1.4.1 Determination of concentrations of catenanes

To unravel the mechanism behind the mutualistic synthesis in DCL based on disulfide and hydrazone exchange, the equilibrium constants of catenanes formation in DCL were determined by HPLC. Since all the components of catenanes in the DCL had UV

absorption and appeared as well-separated peaks in the HPLC, their concentrations can be quantified by peak areas. According to the previous report on building block **1** and unmodified cyclodextrin, catenation does not affect the UV spectra of the macrocycles involved.[106] Besides, the total peak area of each DCL was almost equal to the sum of that of building block **1** and **CD**. Therefore, the concentrations of the library members could be obtained from peak areas by using Equation 1.

$$[\boldsymbol{x-yCD}] = A_{[\boldsymbol{x-yCD}]}/(xC_1 + yC_2) \quad (1)$$

Where C_1 = 4880.86 mAU·min·mM^{-1} and C_2 = 3811.06 mAU·min·mM^{-1} were the coefficients relating peak areas of **1** and **CD** obtained to their corresponding concentrations; x and y represent the number of building blocks **1** and **CD** in catenanes, respectively. For example, the concentration of catenane **3-CD** was calculated as: $[\boldsymbol{3-CD}] = A_{[\boldsymbol{3-CD}]}/(3 * 4880.86 + 1 * 3811.06)$.

4.1.4.2 Determination of equilibrium constants in the library (**1** + **CD**)

In order to obtain accurate estimates of the equilibrium constants in the system, we first set up the control group (**1** + **CD**), which contained the building block **1** (1 mM) and the building block **CD** (0 - 4 mM) in borate buffer (50 mM, pH 8.2) as the starting point to investigate their complex equilibrium of the system. After the DCLs were totally oxidized, the peak area of each library species is listed below in Table 1, and the concentrations of these members were calculated by using Equation 1, which were listed in Table 2. As we were interested primarily in the equilibrium constants of binding templates to different catenane **x-yCD**, these were the only species that were explicitly considered. The other species in the system (overoxidized sulfinic acid side product) were not included in the table.

Table 1. HPLC-UV peak areas (mAU·min) for members of DCLs that were made from building blocks **1** (1 mM) with varying concentrations of **CD** (M) as a template in 50 mM borate buffer at pH = 8.2.

	HPLC-UV peak area (mAU·min)								
CD (M) / Member	**0**	**5.00E-04**	**1.00E-03**	**1.50E-03**	**2.00E-03**	**2.50E-03**	**3.00E-03**	**3.50E-03**	**4.00E-03**
4-2CD	0.0	2832.1	3326.2	3652.9	3678.8	3711.0	3773.9	3836	3910.9
4-CD	0.0	190.8	171.1	39.8	125.5	117.2	115.6	110.2	107.3
3-CD	0.0	1590.1	1786.8	1694.2	1690.0	1662.6	1659.9	1641.4	1539.2
3	246.8	117.1	101.7	87.3	70.6	67.4	55.1	53.7	53.9
4	374.3	80.5	82.8	67.3	84.6	81.6	52.1	49.0	48.1
3_2	4259.7	322.6	362.1	401.4	367.0	331.7	324.3	321.4	325.3

Table 2. Calculated concentrations for members of DCLs (M) that were made from building blocks **1** (1 mM) with varying concentrations of **CD** (M) as a template in 50 mM borate buffer at pH = 8.2.

	Calculated concentration of members (M)								
CD (M) / Member	**0**	**5.00E-04**	**1.00E-03**	**1.50E-03**	**2.00E-03**	**2.50E-03**	**3.00E-03**	**3.50E-03**	**4.00E-03**
4-2CD	0.00E+00	1.04E-04	1.23E-04	1.35E-04	1.36E-04	1.37E-04	1.39E-04	1.41E-04	1.44E-04
4-CD	0.00E+00	8.18E-06	7.33E-06	5.99E-06	5.38E-06	5.02E-06	4.95E-06	4.72E-06	4.60E-06
3-CD	0.00E+00	8.62E-05	9.68E-05	9.18E-05	9.16E-05	9.01E-05	8.99E-05	8.89E-05	8.34E-05
3	1.69E-05	8.00E-06	6.94E-06	5.96E-06	4.82E-06	4.61E-06	3.76E-06	3.66E-06	3.68E-06
4	1.92E-05	4.12E-06	4.24E-06	3.45E-06	4.33E-06	4.18E-06	2.67E-06	2.51E-06	2.46E-06
3_2	1.45E-04	1.10E-05	1.24E-05	1.37E-05	1.25E-05	1.30E-05	1.11E-05	1.10E-05	1.11E-05

Then, a simple model of the control group (**1** + **CD**) that was able to produce a good fit in the presence of a series of catenanes was established in Figure 10a. It is noticeable that these equilibria do not represent realistic reaction pathways, since disulfide reduction does not occur under the condition of our experiments. Therefore, only specific equilibrium constants that are fitted include those that relate library members to their appropriate building blocks. Since the concentrations of the components in the libraries could be calculated, we can use Equation 2 to calculate the equilibrium constant.

$$K_{catenane} = [catenane]/[macrocycle][CD] \quad (2)$$

For example, the equilibrium constant of $K_{3\text{-}CD}$ is equal to [**3-CD**] [**3**]$^{-1}$ [**CD**]$^{-1}$, while the equilibrium constant of $K_{4\text{-}2CD}$ is equal to [**4-2CD**] [**4-CD**]$^{-1}$ [**CD**]$^{-1}$. Then, to iterate and adjust the values of the equilibrium constants until the error between observed and fitted data was minimal, the dataset of quantified concentrations from HPLC peak areas in the control group was fitted to the model in Figure 10a by using *DCLFit* software, which has been implemented in previous works.[106,118,119] We used the ordinary least squares error method, Nelder Mead Simplex minimizer, and repeated the procedure 500 times using the Monte-Carlo approach to ensure that the global error minimum was found. The comparisons between observed concentration and fitted profiles of catenanes in the control group (**1** + **CD**) were shown in Figure 10b-d. As the peak areas in DCLs cannot be normalized into a certain value, the equilibrium constants were calculated by averaging. The difference between observed data and fitted data probably resulted from the error in the measurement.

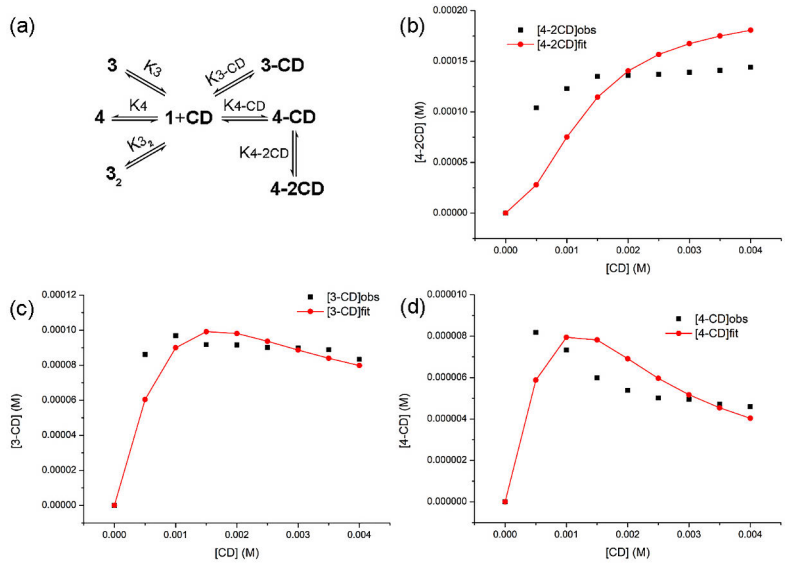

Figure 10. (a) The model used to fit the library distributions in control group (**1** + **CD**); the relationship between the concentrations of catenanes and the aldehyde **CD** (0 - 4 mM) in the control group (**1** + **CD**). (b) **4-2CD**; (c) **3-CD**; (d) **4-CD**. Black represents the observed data in HPLC, red represents the fitted data in *DCLfit*.

The equilibrium constants of catenanes in the control group (**1** + **CD**) were shown in Table 5. The association constant for the first binding of **CD** to the tetramer **4** (log $K_{4\text{-}CD}$) was 3.01 ± 0.30, whereas the binding constant for incorporating the second **CD** to yield **4-2CD** (log $K_{4\text{-}2CD}$) was 4.11 ± 0.09, implying that the tetramer **4** had the cavity suitably for the interaction with two **CD** to form catenane **4-2CD**, while the trimer **3** cavity was large enough to fit only one **CD**. Besides, in the molecular dynamic (MD) simulation of the system, **4-2CD** had a lower binding energy than that of **4-CD**.[105] These results proved that in the library of (**1** + **CD**), catenane **4-2CD** was a thermodynamically favorable product, which may become the prerequisite to catalyse hydrazone formation in the library (**1** + **CD** + **L**).

4.1.4.3 Determination of equilibrium constants in the library (**1** + **L** + **CD**)

To further confirm pre-organised **4-2CD** was crucial to catalyse the mutualistic synthesis of its two minor components, **4** and **L-2CD**, the experimental group (**1** + **CD** + **L**), a series of DCLs consisting of the building block **1** (1 mM), hydrazide **L** (1 mM), and the aldehyde **CD** (0-4 mM), were analysed by HPLC after oxidation (Table 3). The concentrations of these members were calculated by using Equation 1, which was listed in Table 4. Repeating the same analysis for (**1** + **L** + **CD**), the

equilibrium constants of **4-2CD**, **4-CD**, and **3-2CD** were obtained in Table 5 using Equation 2, which were close to those in the control group.

Table 3. HPLC-UV peak areas (mAU·min) for members of DCLs that were made from building blocks **1** (1 mM) and **L** (1 mM) with varying concentrations of **CD** (M) as a template in 50 mM borate buffer at pH = 8.2.

	HPLC-UV peak area (mAU·min)								
CD (M) / Member	**0**	**5.00E-04**	**1.00E-03**	**1.50E-03**	**2.00E-03**	**2.50E-03**	**3.00E-03**	**3.50E-03**	**4.00E-03**
4-L-2CD	0.0	3508.1	4383.6	4628.4	4851.1	5043.5	5105.3	5248.3	5258.4
4-2CD	0.0	353.2	461.2	436.1	430.1	405.8	401.6	391.7	397.8
4-CD	0.0	120.7	85.7	64.1	58.3	53.4	46.4	33.9	23.5
3-CD	0.0	445.8	363.3	297.8	237.1	229.0	210.7	200.5	192.8
3	246.8	183.7	104.2	68.9	63.1	59.8	57.9	44.5	39.3
4	374.3	34.5	92.9	47.8	33.7	36.6	37.3	36.6	33.3
3_2	4259.7	498.8	395.1	326.8	287.9	316.4	308.3	323.6	316.7

Table 4. Calculated concentrations for members of DCLs (M) that were made from building blocks **1** (1 mM) and **L** (1 mM) with varying concentrations of **CD** (M) as a template in 50 mM borate buffer at pH = 8.2.

	Calculated concentration of members (M)								
CD (M) / Member	**0**	**5.00E-04**	**1.00E-03**	**1.50E-03**	**2.00E-03**	**2.50E-03**	**3.00E-03**	**3.50E-03**	**4.00E-03**
4-L-2CD	0.00E+00	1.29E-04	1.61E-04	1.70E-04	1.78E-04	1.86E-04	1.88E-04	1.93E-04	1.94E-04
4-2CD	0.00E+00	1.30E-05	1.70E-05	1.61E-05	1.58E-05	1.49E-05	1.48E-05	1.44E-05	1.47E-05
4-CD	0.00E+00	5.17E-06	3.67E-06	2.75E-06	2.50E-06	2.29E-06	1.99E-06	1.45E-06	1.01E-06
3-CD	0.00E+00	2.42E-05	1.97E-05	1.61E-05	1.28E-05	1.24E-05	1.40E-05	1.09E-05	1.04E-05
3	1.69E-05	1.25E-05	7.12E-06	4.71E-06	4.31E-06	4.08E-06	3.95E-06	3.04E-06	2.68E-06
4	1.92E-05	6.89E-06	4.76E-06	2.45E-06	1.73E-06	1.87E-06	1.91E-06	1.87E-06	1.71E-06
3_2	1.45E-04	1.70E-05	1.35E-05	1.12E-05	9.83E-06	1.08E-05	1.05E-05	1.10E-05	1.3E-05

Since the concentrations of free **L** and **L-2CD** were not readily detectable in the present DCLs, the equilibrium constant of hydrazone formation (**L** + 2**CD** → **L-2CD**) cannot be calculated using Equation 2. Hence, we iterated the dataset in *DCLfit* and obtained a fitted constant of 1.16 ± 0.02 for **4-L-2CD**, while **L-2CD** could not be synthesized directly by only **L** and **CD** (Figure 11-12). The difference between observed data and fitted data of **4-CD** mainly resulted from the error in the measurement. These results demonstrated that the pre-organised catenane **4-2CD** structures could effectively catalyse the hydrazone formation at pH 8.2, while the formation of **L-2CD** made tetramer **4** stable through the formation of the complex handcuffs catenane **4-L-2CD** in DCL. Hence, **4** and **L-2CD** were a pair of mutualistic molecules, leading to the high yield of "handcuffs" catenane **4-L-2CD**.[105]

Table 5. Equilibrium constants of libraries for catenane formation[105]

	Log K[a]			
	4-L-2CD	**4-2CD**	**4-CD**	**3-CD**
1 + CD[b]	/	4.19 ± 0.16	2.98 ± 0.25	4.06 ± 0.16
Fitting[c]	/	4.11 ± 0.09	3.01 ± 0.30	4.02 ± 0.10
1 + CD + L[b]	/	4.07 ± 0.11	3.24 ± 0.24	3.79 ± 0.28
Fitting[c]	1.16 ± 0.02	4.00 ± 0.12	3.20 ± 0.04	3.92 ± 0.08

[a] Corresponding binding constant *K* are in M^{-1}.
[b] Equilibrium constants are calculated from Equation 2. Data are expressed as mean values ± SD.
[c] Equilibrium constants are fitted by *DCLfit*.

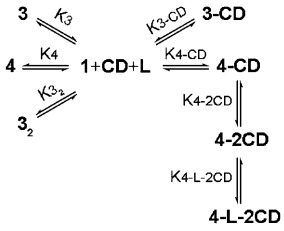

Figure 11. The model used to fit the library distributions in control group (**1** + **CD** + **L**).

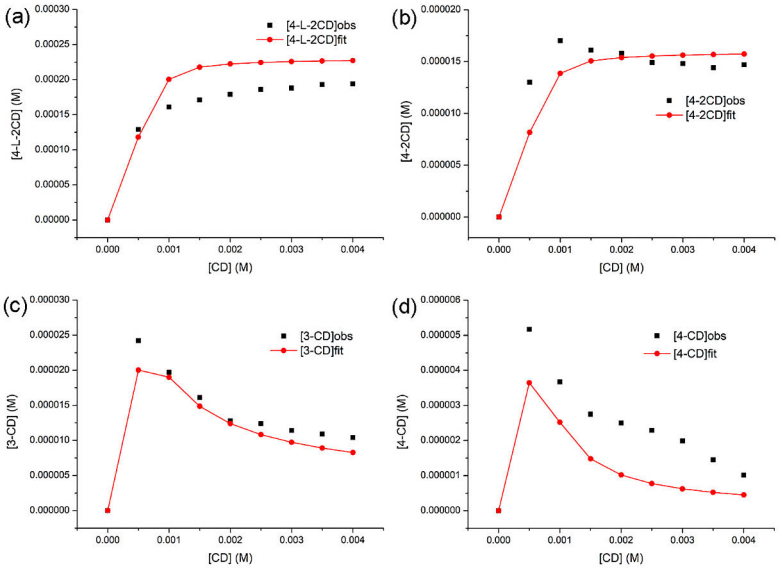

Figure 12. The relationship between the concentrations of catenanes and the aldehyde **CD** (0 - 4 mM) in the control group (**1** + **CD** + **L**). (a) **4-L-2CD**; (b) **4-2CD**; (c) **3-CD**; (d) **4-CD**. Black represents the observed data in HPLC, red represents the fitted data in *DCLfit*.

4.1.5 Kinetics analysis of the system

We started by investigating a DCL composed of **1** (1.5 mM) in borate buffer (50 mM, pH 8.2). The composition of the mixture was monitored over time using HPLC. A rapid increase in the amount of catenane $\mathbf{3_2}$ (around 76 %) was followed by a slight decrease after 36 h, which coincided with the gradual concentration growth of **3**, probably attributed to the breakage of $\mathbf{3_2}$ (Figure 13a). In the DCL containing an equimolar of solution **1** and **CD** (1.5 mM), the species **4-CD** formed rapidly in 12 h, followed by decreasing to 1.6 %, while **4-2CD** became the dominant species after 24 h (Figure 13b). The phenomenon should be attributed to the high affinity between one molecular disulfide tetramer **4** and two molecular **CD**s. Then, in the DCL containing 1.5 mM **1**, **CD**, and **L** at the same condition, once **4-L-2CD** emerged, it grew dramatically over 50 % in 36 h at the expense of other species, suggesting that **4-L-CD** rich state was a stable system (Figure 13c).

To further investigate the mutualistic relation of **4** and **L-2CD** in the library, we constructed the model as a set of ordinary differential equations (ODEs), where three building blocks (**1**, **CD**, and **L**) have influences on each other in DCL (Table 6). In the model, building block **1** is oxidized to give non-assembled trimer **3**, tetramer **4**, and catenanes $\mathbf{3_2}$. Dimer **2** is metastable and will be consumed quickly during oxidization (Table 6 reaction 1 to 3). These steps are modelled as first order in overall building block concentration, as observed experimentally for thiol oxidation. The

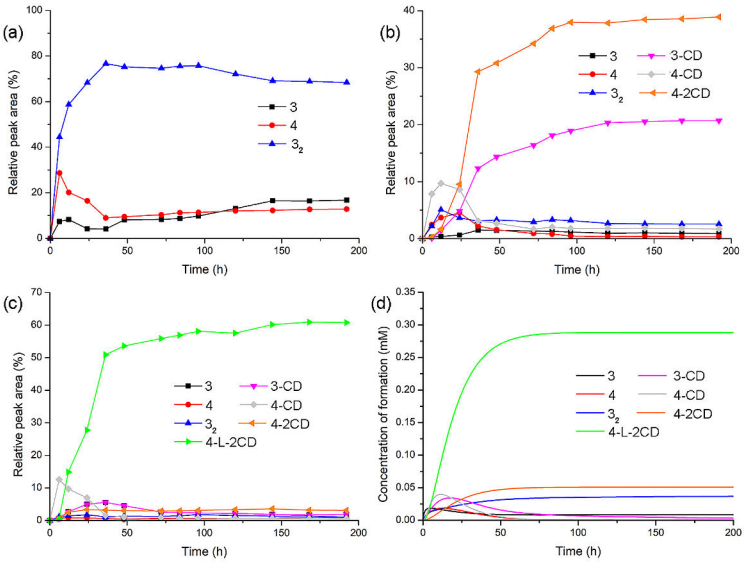

Figure 13. Kinetics study of catenane formation in DCLs in borate buffer (50 mM, pH 8.2). (a) 1.5 mM of **1**; (b) 1.5 mM of **1** and **CD**; (c) 1.5 mM of **1**, **CD** and **L**; (d) kinetic modelling results of the catenanes in DCL containing 1.5 mM of **1**, **CD**, and **L**. Reprinted with permission from *Angew. Chem. Int. Ed.* **2024**, e202412020.

thiol-disulfide exchange process, by which macrocycles and catenane can interconvert via disulfide exchange (reaction 4 to 7). These exchange reactions involve multiple steps but are approximated by single rate laws that are second order in a building block and macrocycle (based on the fact that the rate law for the disulfide exchange reaction has this form). The breakage of catenane also occurs during this process (reaction 8). Due to the host-guest interaction of azobenzene and β-CD, macrocycles (**3** and **4**) will be combined with **CD** to form different complex structures (**3-CD**, **4-CD**, **4-2CD**), and interconvert may also occur (reaction 9-12). The existence of hydrazide **L**, makes the hydrazone formation possible (reaction 13-14).

Then, we determined the majority of the involved rate constants and reaction orders experimentally, including the rates of thiol oxidation, thiol-disulfide exchange, breakage of catenane, and hydrazone formation (Figure 14). These experimentally measured data were used to parameterize this kinetic model,[120,121] with which we analysed the reactions through pathways.

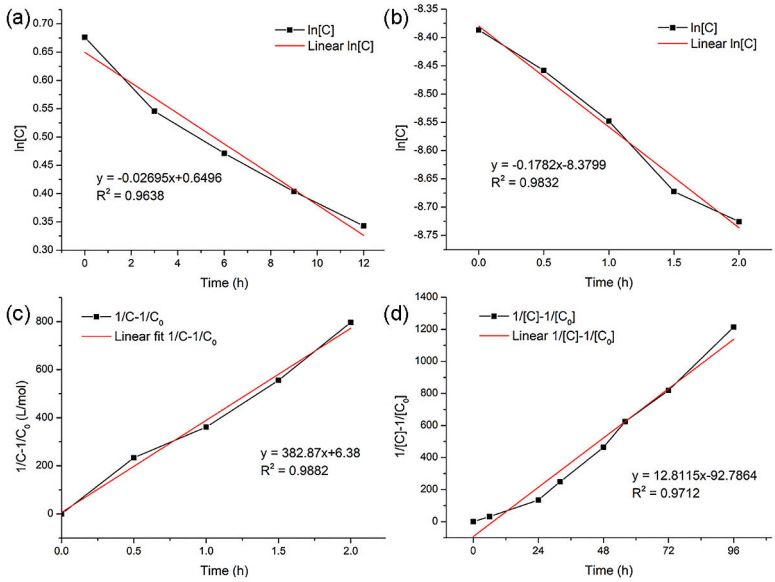

Figure 14. Kinetic data of (a) oxidation of thiol of **M**. The fitting rate constant was 0.2695 h^{-1}; (b) the breakage of catenane **3₂**. The fitting rate constant was 0.1782 h^{-1}; (c) thiol-disulfide exchange of **A** and **D₂**. The fitting rate constant was 382.87 M^{-1} h^{-1}; (d) hydrazone formation. The fitting rate constant was 12.81 M^{-1} h^{-1}. Reprinted with permission from *Angew. Chem. Int. Ed.* **2024**, e202412020.

Table 6. Reactions and rate equations considered in the kinetic model. Rate equations are given from the point of view of the reactants, and the ODEs are constructed using the equations and the stoichiometry of the reactions. Rate constant values used for kinetic simulations.

No	Reaction	Rate equation	Value
1	**1** + 1/2**O₂** → **2**	k^{ox1} [**1**]	0.02831 h^{-1}
2	**2** + 1/2**O₂** → **3**	k^{ox2} [**2**]	338.5 h^{-1}
3	**2** + 1/2**O₂** → **4**	k^{ox3} [**2**]	0.09266 h^{-1}
4	**3** + **1** → **4**	k^{ex4} [**1**] [**3**]	0.2918 M^{-1} h^{-1}
5	**4** + **2** → **23**	k^{ex5} [**2**] [**4**]	1.589×10^{-5} M^{-1} h^{-1}
6	**23** → **3₂**	k^{ex6} [**3**]^2	0.7698 M^{-1} h^{-1}
7	**1** + **3₂** → **3** + **4**	k^{ex7} [**1**] [**3₂**]	0.7179 M^{-1} h^{-1}
8	**3₂** → **23**	k^{break8} [**3₂**]	0.1796 h^{-1}
9	**3** + **CD** ⇌ **3-CD**	k^{c9} [**3**] [**CD**]	0.1467 M^{-1} h^{-1}
		k^{-c9} [**3-CD**]	0.09037 h^{-1}
10	**4** + **CD** ⇌ **4-CD**	k^{c10} [**4**] [**CD**]	0.9753 M^{-1} h^{-1}
		k^{-c10} [**4-CD**]	0.5897 h^{-1}
11	**4** + 2**CD** ⇌ **4-2CD**	k^{c11}[**4**] [**CD**]	0.4652 M^{-1} h^{-1}
		k^{-c11}[**4-2CD**]	2.6054×10^{-5} h^{-1}
12	**1** + **3-CD** ⇌ **4-CD**	k^{ex12} [**1**] [**3-CD**]	7.8855×10^{-10} M^{-1} h^{-1}
		k^{-ex12} [**4-CD**]	0.01844 h^{-1}
13	**4-2CD** + **L** ⇌ **4-L-2CD**	k^{h3} [**4-2CD**] [**L**]	14.9493 M^{-1} h^{-1}
		k^{-h3} [**4-L-2CD**]	3.1866 h^{-1}
14	**CD** + **H₂O** → **CD-H₂O**	k^{h4} [**CD**]	0.007808 h^{-1}

The experimental kinetic analysis of hydrazone formation showed that the reaction **4-2CD** + **L** → **4-L-2CD** in solution occurred rapidly and the rate constant of hydrazone formation was measured as k = 12.81 M^{-1} h^{-1}, which was close to the calculated value 14.95 M^{-1} h^{-1} (Table 6, Figure 13d) using the kinetic model for the hybrid library. The high reaction rate of the hydrazone formation offered a potentially fast competing pathway to equilibrium, suggesting that the thermodynamic stable **4-2CD** from a disulfide library acted as the transition state to promote the hydrazone formation.[105]

4.1.6 Conclusion

In this chapter, we have demonstrated the concept of molecular mutualistic synthesis involving species from orthogonal reversible chemical reactions (disulfide exchange and hydrazone exchange). When these reactions occurred concurrently in a DCL, two initially minor products, disulfide tetramer **4** and linear hydrazone **L-2CD** became predominant. Specifically, the building block **CD** from the inert reaction (hydrazone exchange) served as a template at first, selectively amplifying a minor library species (tetramer **4**) from the active reaction (disulfide exchange). This process led to the formation of a thermodynamically stable catenane **4-2CD** through non-covalent binding. This catenane, acting as a transition state, catalysed the inert reaction between its associated reactant **CD** and the other freely present reactant dihydrazide **L** in the solution. This interaction resulted in the dominant products **4-L-2CD**, of which both reactions aiding each other's formation, demonstrating a mutualistic relationship. We envision this challenge can be addressed by adjusting noncovalent affinities among species in new molecular systems to enable these species to cross-catalyse the orthogonal reactions more effectively.

4.2 Dynamic covalent macrocycles for drug and gene co-delivery

4.2.1 Introduction

Over the last few decades, multiple drug resistance (MDR), a major challenge in cancer treatment, often occurs during the course of treatment or upon recurrence of the disease after traditional chemotherapy.[122] Researchers have investigated many different mechanisms responsible for the MDR of cancer cells during chemotherapy, including enhanced efflux of drugs, the mutation of oncogenes, activated cell growth factors, and elevated metabolism of xenobiotics.[122-124] Among these mechanisms, the most widely studied are those associated with drug efflux mechanisms involving adenosine triphosphate-binding (ATP-binding) cassette (ABC) membrane transporters.[125] P-glycoprotein (P-gp/ABCB1), a 170 kDa plasma membrane protein encoded by the MDR1 gene, is correlated with the reversal of the MDR phenotype in many different types of cancers, resulting in the lack of response to chemotherapies and poor prognoses in breast and ovarian cancers.[125-127] To overcome MDR at the genetic level, combination therapy with effective anti-cancer drugs and functional genes, such as siRNA, is a powerful tool in cancer treatment.[128-130]

To achieve the simultaneous delivery of siRNA and anti-cancer drugs to MDR cancer cells, several strategies for designing vectors have been reported, such as polymer-based carriers,[131] inorganic nanoparticles,[132] and liposomes.[133] Among these carriers, polymeric delivery systems are most widely used due to their stability and availability of different synthetic routes. Yet, this strategy has individual disadvantages. For example, the drug loading capabilities of polymeric carriers are relatively low,[134] and it is challenging to control the effective release of drug and genes in cancer cells.[59,135,136]

In the second part of the thesis, a simple building block **2** containing thiol groups was synthesized, which could self-synthesize into macrocycles through disulfide exchange.[137] After adding the anti-cancer drug DOX and siRNA, the macrocycles could self-assemble into nanoparticles under thermodynamic control. Various techniques were utilized to characterize this macrocycles-based co-delivery system, and its enhanced cellular uptake ability and anti-MDR cancer cells efficiency have been investigated.

4.2.2 Experimental Section

4.2.2.1 Synthesis of building block **2**

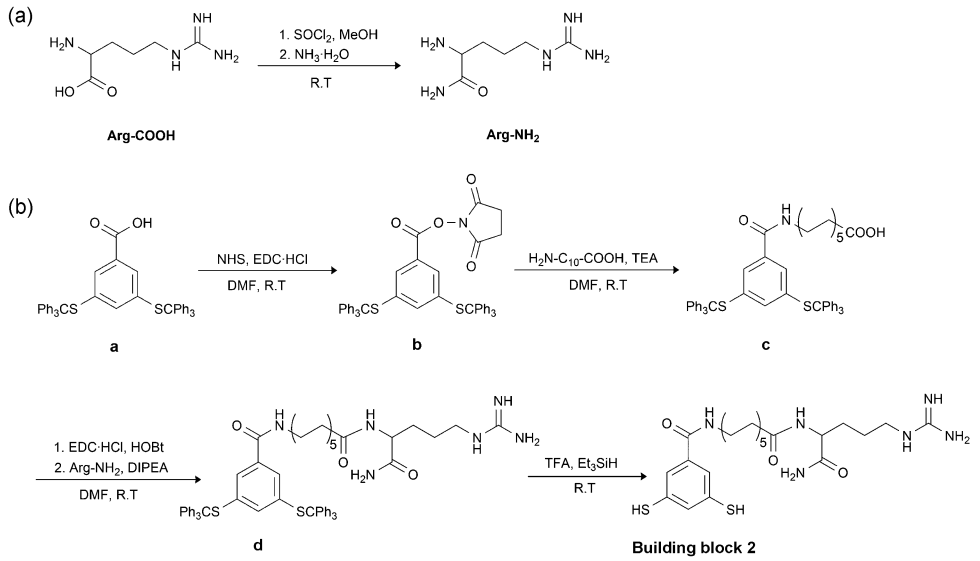

Scheme 8. Synthetic route of (a) Arg-NH_2; (b) building block **2**.

The starting compound 3,5-bis(tritylthio)benzoic acid **a** was synthesized according to the previous described procedure.[138] Then compound **a** was activated by NHS, after mixing with coupling reagent EDC·HCl in DMF, giving 3,5-bis(tritylthio)benzoic acid-*N*-hydroxysuccinimide ester **b**. The NHS-activated acid **b** and 11-aminoundecanoic acid were dissolved in DMF with TEA, and then the reaction was conducted overnight to generate 11-[3,5-bis(tritylthio)benzoyl)amino]undecanoic acid **c**. Subsequently, condensation of Arg-NH_2[139] and compound **c** afford 11-[3,5-bis(tritylthio)benzoyl)amino]undecanoyl-arginine amide **d**. Finally, after being treated with TFA and TES, compound **d** gave the building block **2** (Scheme 8).

4.2.2.2 Preparation of $\mathbf{2_3}$+$\mathbf{2_4}$/DOX nanofibers

DOX (100 mg) was accurately measured and dissolved in 1 mL of deionized water. Building block **2** (0.21 mg) was accurately measured and dissolved in pH 7.4 PBS (1 mL), and then DOX solution (2 μL) was introduced into the mixture. After full oxidation, the prepared $\mathbf{2_3}$+$\mathbf{2_4}$/DOX nanofibers were purified by dialysis for 1 day.

4.2.2.3 Preparation of $\mathbf{2_3}$+$\mathbf{2_4}$/DOX/siRNA nanoballs

Typically, 2 mg of $\mathbf{2_3}$+$\mathbf{2_4}$/DOX was dissolved in 1 mL PBS and sonication for 10 min. Then, the $\mathbf{2_3}$+$\mathbf{2_4}$/DOX solution was incubated with siRNA for 1 h at different N/P ratios (0, 1, 2, 3, 4, 5, 6, 8, 10, 15, and 20) to form the $\mathbf{2_3}$+$\mathbf{2_4}$/DOX/siRNA nanoballs. The N/P ratio represents the molar ratio of cationic nitrogen in $\mathbf{2_3}$+$\mathbf{2_4}$/DOX to phosphate in siRNA. The complex solutions at different N/P ratios were added into Amicon Ultra-4 centrifugal filter devices (50 kD, Millipore, Massachusetts) and centrifuged (speed: 5000 rpm, time: 10 min).

4.2.2.4 Agarose gel electrophoresis analysis

The $\mathbf{2_3}$+$\mathbf{2_4}$/DOX/siRNA nanoballs solutions at different N/P ratios (0, 1, 2, 3, 4, 5, 6, 8, 10, 15, and 20) were sampled in an agarose gel plate (2% (w/v), ethidium bromide (0.5 mg/mL)) which was submerged in an electrophoresis tank filled with an appropriate amount of Tris-acetate-EDTA buffer. The system was running for 20 min at 120 V. Then, a Bio-Rad Imager was used to obtain the visual result.

In resistance to heparin replacement experiment, $\mathbf{2_3}$+$\mathbf{2_4}$/DOX/siRNA solutions at different N/P ratios (0, 1, 2, 3, 4, 5, 6, 8, 10, 15, and 20) were mixed with heparin (heparin/siRNA (IU/mg) = 10) for 10 min. After that, the mixtures were incubated at 25 °C for 60 min. Then, the samples were electrophoresed at 120 V for 20 min.

4.2.2.5 *In vitro* release of $\mathbf{2_3}$+$\mathbf{2_4}$/DOX/siRNA in response to pH/redox stimuli

Phosphate buffers at different pH (7.4 and 5.5) with/without 5 mM GSH were selected as the media to simulate biological and early/late endosomal conditions. The $\mathbf{2_3}$+$\mathbf{2_4}$/DOX/siRNA solutions were added into dialysis bags and put into a conical flask with 10 mL PBS solution at different pH (7.4 and 5.5) with/without 5 mM GSH. The flasks were then placed into a shaking incubator for 72 h at 37 °C. At a scheduled point, the sample was taken out and an equal medium was added. The amount of DOX in the medium was measured and analysed by UV-Vis spectrophotometer at 480 nm. The release of siRNA from the $\mathbf{2_3}$+$\mathbf{2_4}$/DOX/siRNA was detected with a ND-1000 as described before.

4.2.2.6 Cell proliferation for cytotoxicity

Breast cancer cell line (MCF-7S), MDR ovarian cancer cell line (NCI/ADR-RES), and human embryonic kidney 293 cell line (HEK293) were cultured in the medium and used to determine the cytotoxicity of $\mathbf{2_3}$+$\mathbf{2_4}$/DOX/siRNA nanoparticles. In brief, different cells (8×10^3 cells·well^{-1}) were seeded onto 96-well flat bottom plates

(Corning) and incubated overnight. Then, the cell culture mediums containing different concentrations of drug or **2**$_3$+**2**$_4$/DOX/siRNA nanoparticles were added into the plates. After incubation for 24/48 h, the prepared MTT solution (5 mg/mL, 10 μL·well^{-1}) was added into each well of the plates. After incubation for 3-4 h, the medium in each well was removed carefully, and then DMSO (100 μL·well^{-1}) was added into the plate. The absorbance at 570 nm was recorded using a Cytation 5 imaging reader (BioTek, U.S.A).

4.2.2.7 Hemolytic evaluation

Red blood cells were collected from a human blood sample by centrifugation (1200 rpm, 5 min), followed by rinsing with PBS three times. 100 μL of red blood cell stock solution was added into a 96-well plate, and then treated with different concentrations of **2**$_3$+**2**$_4$/DOX/siRNA nanoparticles for 2 h. After that, the supernatant in each well was collected, and the absorbance at 570 nm was recorded using a Cytation 5 imaging reader (BioTek, U.S.A).

4.2.2.8 Cell uptake studied by CLSM

The cellular uptake of drug and siRNA was observed by CLSM. NCI/ADR-RES cells (5×10^4 cells·well^{-1}) were seeded in a 6-well plate (Corning) that contained a coverslip in each well overnight. Then, the cell culture mediums containing DOX, FAM-siRNA, **2**$_3$+**2**$_4$/DOX nanofibers, and **2**$_3$+**2**$_4$/DOX/siRNA nanoparticles solution were added into the plates carefully. After incubation for 4 h, NCI/ADR-RES cells were washed with PBS to remove the samples. 4% paraformaldehyde (1 mL·well^{-1}) was added into the plate and incubated for 10 min to fix the cells, followed by rinsing with PBS. The cell nuclei were stained with the Hoechst 33342 solution (10 μg/mL, 200 μL·well^{-1}) for 10 min and rinsed with PBS. The coverslip was placed on the glass slide with mounting medium, dried, and sealed with clear nail polish. The samples were observed with a Zeiss LSM880.

4.2.2.9 Cell uptake studied by FC

For the FC detection, the same procedure as for CLSM, DOX, **2**$_3$+**2**$_4$/DOX nanofibers, and **2**$_3$+**2**$_4$/DOX/siRNA nanoparticles solutions were added into 6-well plates. After incubation for 4 h, NCI/ADR-RES cells were washed with PBS three times to remove the samples. After that, the cells were detached by trypsin-EDTA, collected, and resuspended in the tubes containing 1 mL of PBS. The fluorescence analysis of samples was conducted on a BD LSRFortessa.

4.2.2.10 *In vitro* gene silencing

Western blot was utilized to evaluate P-gp expression levels in NCI/ADR-RES cells. In brief, NCI/ADR-RES cells (10^5 cells·well^{-1}) were seeded in a 6-well plate overnight. Then, the cell culture medium containing DOX, siRNA, and **2**$_3$+**2**$_4$/DOX/siRNA solution were added into the plates carefully. After incubation, the cells were rinsed with pre-cooled PBS to remove samples. Lysis buffer (100 μL·well^{-1}) was added into the plate, then agitated the plate for 20 min at 4 °C, followed by centrifuge (15000 rpm, 20 min). The supernatant was collected and the concentration of protein was measured by the BCA protein kit. After electrophoresis with SDS-PAGE, the separated proteins were transferred onto the PVDF membrane. After sealing with the blocking buffer for 1 h, the membranes were incubated with P-gp mouse monoclonal antibody overnight. After washing with buffer three times, the membranes were incubated with the secondary antibody solution for 1 h, and the bands were visualized by Enhanced chemiluminescence (ECL) on a film.

4.2.2.11 Apoptotic analysis

NCI/ADR-RES cells (10^5 cells·well^{-1}) were seeded in the 6-well plate overnight. Then, the cell culture medium containing DOX, siRNA, **2**$_3$+**2**$_4$, **2**$_3$+**2**$_4$/DOX nanofibers and **2**$_3$+**2**$_4$/DOX/siRNA nanoparticles solution were added into the plates. After incubation for 24 h, the cells were detached by trypsin-EDTA, collected, and rinsed with PBS twice. The cell pellets in each well were resuspended in Annexin binding buffer (200 μL), followed by the addition of Annexin V-FITC (5 μL·well^{-1}) to stain for 15 min. Then, propidium iodide (PI) solution (5 μL·well^{-1}) was added to stain for 15 min. Finally, the cell suspensions were added into tubes containing 800 μL of PBS. The fluorescence analysis of samples was conducted on a BD LSRFortessa.

4.2.3 Synthesis of building block **2**

We used 3,5-bis(tritylthio)benzoic acid as the starting material to synthesize a dithiol building block **2**. As shown in Scheme 8, a hydrophobic segment functionalized with an arginine was attached to building block **2**. The hydrophobic segment was supposed to encapsulate anti-cancer drug molecule DOX and increase self-assembly ability, owing to hydrophobic effects. The arginine part could improve the cell penetration and nuclear localization of the target nanocarriers. To overcome the negative effects caused by MDR, anti-P-gp siRNA was chosen to inhibit the expression of pump proteins, which could be loaded by arginine moiety through ionic interaction.

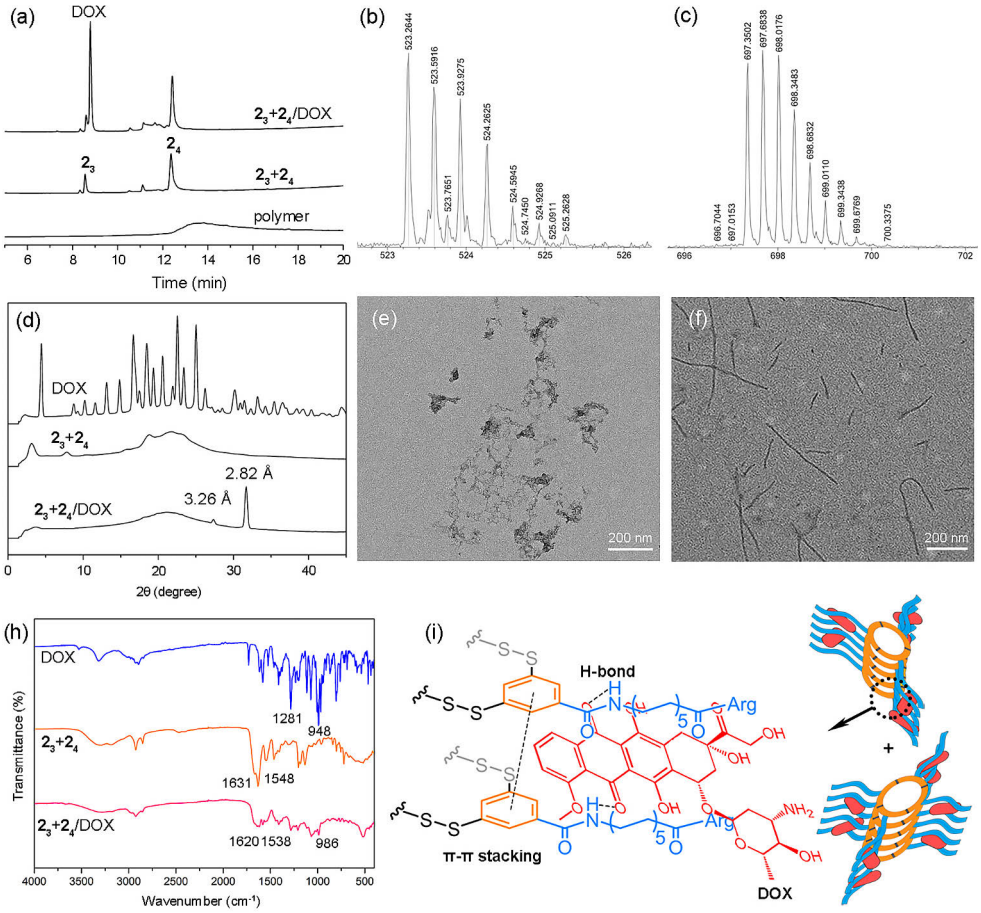

Figure 15. (a) HPLC analysis of **2₃+2₄**/DOX, **2₃+2₄** and polymer rapid oxidized by H_2O_2 in PBS buffer (pH 7.4); (b) ESI-MS spectrum of **2₃**; (c) ESI-MS spectrum of **2₄**; (d) PXRD of DOX, **2₃+2₄** and **2₃+2₄**/DOX; (e) TEM image of **2₃+2₄**. Scale bar, 200 nm; (f) TEM image of **2₃+2₄**/DOX nanofibers. Scale bar, 200 nm; (h) FT-IR spectra of DOX, **2₃+2₄** and **2₃+2₄**/DOX; (i) an illustration of the self-assembled nanostructure of **2₃+2₄**/DOX nanofibers. Reprinted with permission from *Cell Rep. Phys. Sci.* **2022,** *3* (11), 101150.

4.2.4 Preparation of **2₃+2₄**/DOX nanofibers

Subsequently, a library of **2** (0.4 mM) with DOX (0.25 mM) was prepared in a vial with PBS buffer (pH 7.4), and the solution was cloudy at first but became gradually clear after 7 days. After removing free DOX by dialysis, the LC-MS result of the library indicated that building block **2** was mainly oxidized into trimeric and tetrameric macrocycles (Figure 15a-c). The drug loading content (DLC) of the delivery system was determined by UV, which was approximately 30.2%.

However, in the kinetic control group, building block **2** was rapidly oxidized in the same solution using H_2O_2, and the mixture was colorless after dialysis, indicating

that the DOX was not loaded. Moreover, a broad peak was observed in the HPLC of this mixture (Figure 15a), where the disulfide polymer could be reduced to building block **2** after adding excess amounts of reductant dithiothreitol (DTT). These results demonstrated that building block **2** could produce the self-assembling macrocycles with the DOX during the slow oxidative process, which can efficiently encapsulate the DOX molecules with a high DLC.

The morphology of **2$_3$**+**2$_4$**/DOX nanostructure was observed using TEM. In Figure 15f, the macrocycles (**2$_3$**+**2$_4$**) co-self-assembled with DOX to form nanofibers with a diameter of approximately 6 nm, which was nearly identical to the size (approximately 4.8 nm) of the macrocycles determined by Chem3D, suggesting that the macrocycles stacked into fibers. Moreover, the analysis of PXRD indicated a semi-crystalline nature of **2$_3$**+**2$_4$**/DOX nanofibers (Figure 15d). The new peak at 27.33° corresponded to the π-π stacking distance of 3.26 Å between macrocycles, and the peak at 31.70° resulted from the interaction of the hydrophobic chains in macrocycles.[140] Besides, the signal of DOX in the spectra almost disappeared, indicating that DOX was fully encapsulated as non-crystalline within the nanofibers. These results demonstrate that the involvement of DOX aligned with the arrangement of the macrocycles.

To further investigate the arrangement of DOX with macrocycles in the system, FT-IR spectrum was measured. After loading with DOX, the absorption bands of carbonyl groups at 1631 cm^{-1} and amide groups at 1548 cm^{-1} of **2$_3$**+**2$_4$** shifted to 1620 and 1538 cm^{-1}, respectively, indicating the presence of hydrogen bonds between DOX and the hydrophobic parts of **2$_3$+2$_4$** (Figure 15h).[141-143] Considering the amphiphilicity of DOX, we proposed that DOX molecules may be buried in the hydrophobic branches of the macrocycles but adjacent to the arginine moiety (Figure 15i).

4.2.5 Preparation of **2$_3$+2$_4$**/DOX/siRNA nanoparticles

2$_3$+**2$_4$**/DOX/siRNA co-delivery system was prepared by mixing **2$_3$**+**2$_4$**/DOX nanofibers with siRNA. As the main interaction for loading siRNA was ionic interaction between the guanidine and the phosphate groups, their ratio would be crucial to the loading process, which was demonstrated by agarose gel electrophoresis (Figure 16a-b). The N/P ratio corresponds to the ratio between the cationic nitrogen (N) of macrocycles and the phosphate group (P) of siRNA. The results showed that when the N/P ratio was over 4, the **2$_3$**+**2$_4$**/DOX could completely retard the siRNA migration. Moreover, in a heparin decomplexation experiment, when the N/P ratio was over 6, **2$_3$**+**2$_4$**/DOX/siRNA could withstand the replacement of the anionic heparin. Therefore, we regarded the optimized N/P ratio as 6 for the subsequent experiment.

After loading with siRNA with this ratio, the TEM analysis showed that the **2$_3$**+**2$_4$**/DOX/siRNA nanoparticles (d ≈ 260 nm) appeared through electrostatic

interaction between **2**$_3$+**2**$_4$/DOX nanofibers and siRNA (Figure 16c-d), and the size of which was in agreement with the Z-average size (298.1 ± 37.1) measured by DLS. Besides, the zeta potential of the nanoparticles was 16.93 ± 0.06 mV, revealing that the nanostructure was positively charged.

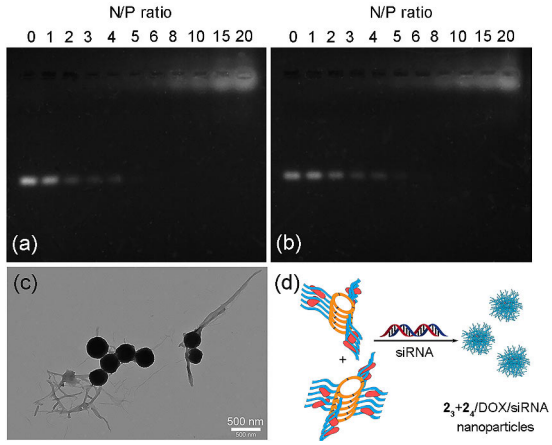

Figure 16. (a) Agarose gel electrophoresis test of **2**$_3$+**2**$_4$/DOX/siRNA at the various N/P ratios; (b) gel retardation test of **2**$_3$+**2**$_4$/DOX/siRNA assay at the various N/P ratios in the presence of heparin; (c) TEM image of **2**$_3$+**2**$_4$/DOX/siRNA nanoparticles. Scale bar, 500 nm; (d) schematic illustration of **2**$_3$+**2**$_4$/DOX/siRNA nanoparticles formation. Reprinted with permission from *Cell Rep. Phys. Sci.* **2022,** *3* (11), 101150.

4.2.6 Redox- and pH-responsiveness of **2**$_3$+**2**$_4$/DOX/siRNA

Once the **2**$_3$+**2**$_4$/DOX/siRNA co-delivery system was obtained, we continued to test its responsiveness, and we considered pH and redox stimuli for the release. In comparison with the normal cells, the cancer cells' microenvironment is more acidic, where the phosphate groups of siRNA tend to protonate, weakening the ionic interaction between siRNA and the macrocycles. In addition, the higher concentration of GSH in cancer cells (>5 mM) can reduce the disulfide bonds of macrocycles into building block **2**, resulting in the break of nanostructure and releasing DOX and siRNA.[144,145] Thus, by adjusting the concentration of GSH in buffers with different pH values, the release behaviors of **2**$_3$+**2**$_4$/DOX/siRNA nanoparticles were studied. Figure 17a shows that, in the presence of 5 mM of GSH at pH 5.5, almost 60 % of DOX could be released within 12 h. In contrast, the cumulative leakage of DOX was quite limited in the other groups. Besides, a similar release behavior could be observed in the release of FAM-siRNA (Figure 17b). These results demonstrate that **2**$_3$+**2**$_4$/DOX/siRNA co-delivery system has an efficient responsive release of the drug and gene but is stable in normal conditions, which is a desirable characteristic for co-delivery in cancer cells.

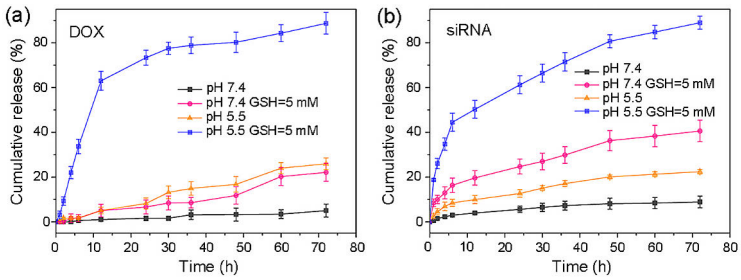

Figure 17. Drug and gene release performance of **2_3+2_4**/DOX/siRNA co-delivery system. (a) DOX release curve and (b) siRNA release curve from **5_3** + **5_4**/DOX/siRNA nanoparticles in PBS (7.4 or 5.5) in the absence or presence of GSH (5 mM). Data are expressed as mean values ± SD. Reprinted with permission from *Cell Rep. Phys. Sci.* **2022,** *3* (11), 101150.

4.2.7 Biocompatibility of **2_3+2_4**/DOX/siRNA

Then, to evaluate the safety and biocompatibility of **2_3**+**2_4**/DOX/siRNA system, a hemolytic study was conducted between the **2_3**+**2_4**/DOX/siRNA nanoparticles and blood components (Figure 18a). The results showed that the hemolytic activity of the delivery system was less than 5% even at the concentration of 8 mg/mL, demonstrating the excellent blood compatibility of the co-delivery system. Furthermore, the cytotoxicity of macrocycles (**2_3**+**2_4**) to human embryonic kidney (HEK293) cell line was measured, and no significant cytotoxicity was observed even though the concentration was up to 0.2 mM (Figure 18b). These results showed that the **2_3**+**2_4**/DOX/siRNA nanoparticles have good biocompatibility which can be used for intravenous administration.

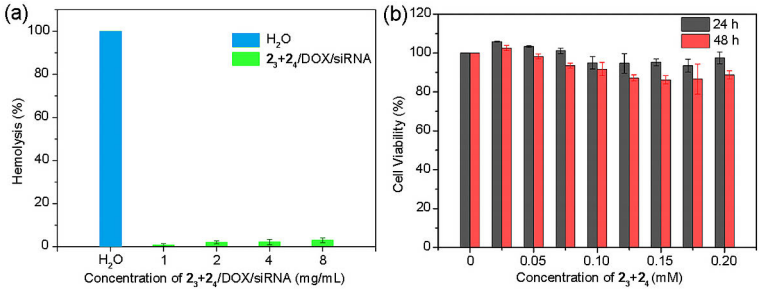

Figure 18. (a) *In vitro* hemolysis assay for **2_3+2_4**/DOX/siRNA nanoparticles; (b) *in vitro* biocompatibility of **2_3+2_4** at different concentrations incubated with HEK293 cells. Data are expressed as mean values ± SD. Reprinted with permission from *Cell Rep. Phys. Sci.* **2022,** *3* (11), 101150.

4.2.8 *In vitro* co-delivery of **2$_3$** + **2$_4$**/DOX/siRNA

To evaluate the ability of **2$_3$**+**2$_4$**/DOX/siRNA system to deliver DOX and siRNA into drug-resistant NCI/ADR-RES cells, CLSM and FC were used to measure the samples. As shown in Figure 19a, in comparison to the naked FAM-siRNA, FAM-siRNAs were delivered into cells at extremely high cellular uptake levels through the endocytosis of **2$_3$**+**2$_4$**/DOX/FAM-siRNA nanoparticles, resulting from the high positive surface charge of the nanoballs that could enhance the interaction between the carrier and the cell membrane. Similarly, the DOX signal intensity of **2$_3$**+**2$_4$**/DOX/FAM-siRNA was significantly higher than that of the free DOX, which confirmed that DOX had partly and effectively entered the nuclei (Figure 19a-b). These results prove that the macrocycle system could efficiently deliver siRNA and DOX into NCI/ADR-RES cells.

To investigate if the system could deliver and transfect P-gp siRNA into MDR cancer cells successfully, the western blotting assay was utilized to assess the gene expression. As shown in Figure 19c, a significant downregulation of P-gp expression was observed in **2$_3$**+**2$_4$**/DOX/siRNA group, which indicated that the nanoparticle can effectively transport P-gp siRNA into NCI/ADR-RES cells, resulting in silencing the expression of P-gp. Based on these results, the **2$_3$**+**2$_4$**/DOX/siRNA co-delivery system may have enhanced ability to kill MDR cancer cell through the combined effects of drug and gene therapy.

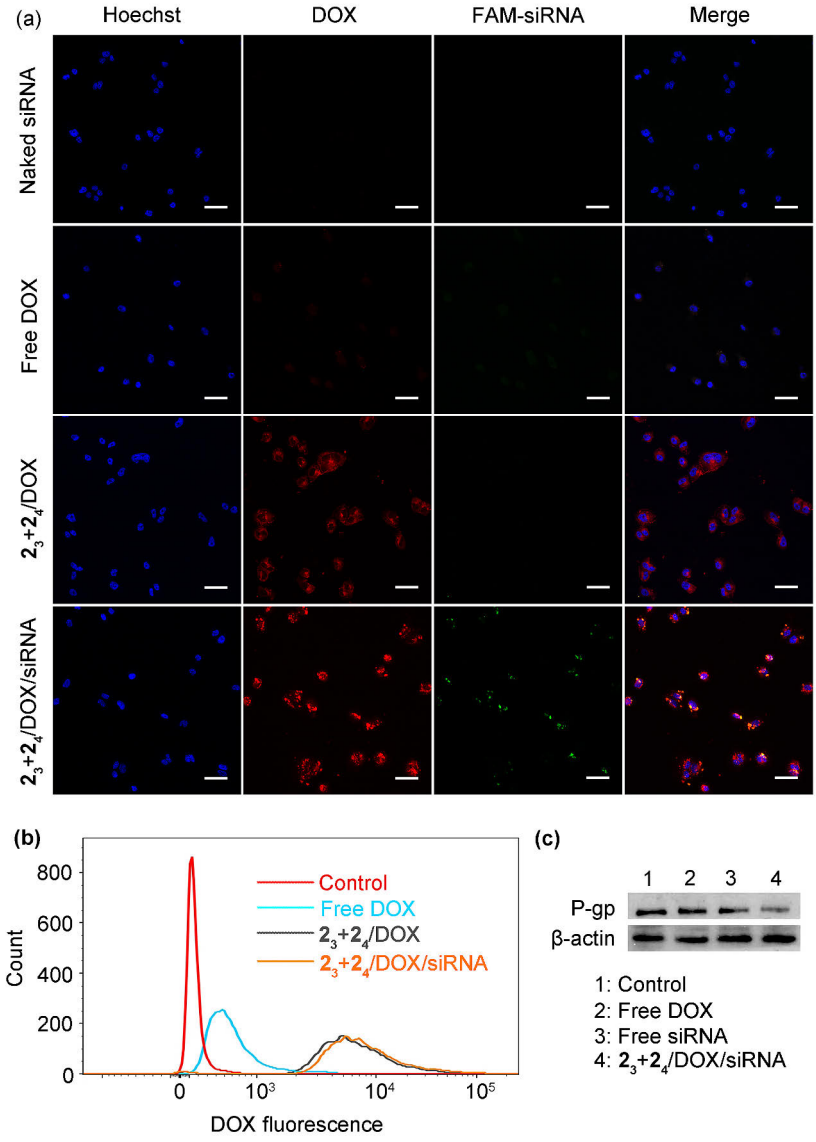

Figure 19. Cell uptake studies of **2_3+2_4**/DOX/siRNA co-delivery system. (a) CLSM images of NCI/ADR-RES cells incubated with free DOX, FAM-siRNA, **2_3+2_4**/DOX and **2_3+2_4**/DOX/siRNA for 4 h. The cell nuclei were stained with Hoechst 33342. Scale bar, 50 μm; (b) flow cytometry curves of NCI/ADR-RES cells incubated with free DOX, **2_3+2_4**/DOX and **2_3+2_4**/DOX/siRNA by measuring DOX fluorescence using PerCP channel; (c) western blot analysis measured the effect of siRNA-mediated knockdown of P-gp expression in NCI/ADR-RES cells. β-actin was used as an internal control. Reprinted with permission from *Cell Rep. Phys. Sci.* **2022,** *3* (11), 101150.

4.2.9 *In vitro* anti-cancer cells of $\mathbf{2_3}$+$\mathbf{2_4}$/DOX/siRNA

To evaluate the combined chemo and gene therapeutic performance of $\mathbf{2_3}$+$\mathbf{2_4}$/DOX/siRNA co-delivery system in MDR cancer cells, the NCI/ADR-RES cells were incubated with free DOX, $\mathbf{2_3}$+$\mathbf{2_4}$/DOX nanofibers, and $\mathbf{2_3}$+$\mathbf{2_4}$/DOX/siRNA nanoparticles for 48 h, respectively to evaluate cell viability. When the concentrations of DOX were low, both $\mathbf{2_3}$+$\mathbf{2_4}$/DOX and $\mathbf{2_3}$+$\mathbf{2_4}$/DOX/siRNA showed better anti-tumor ability than free DOX (Figure 20a). When the concentration of DOX increased to 100 μg/mL, the viability of cells exposed to $\mathbf{2_3}$+$\mathbf{2_4}$/DOX/siRNA nanoparticles was 21.6 %, which was lower than that of cells exposed to $\mathbf{2_3}$+$\mathbf{2_4}$/DOX nanofibers (36.6 %), resulting from the success in delivery of siRNA silencing the expression of P-gp in cells. These results indicated the synergistic effect of DOX and siRNA on cells, demonstrating the enhanced anti-cancer cells efficacy of $\mathbf{2_3}$+$\mathbf{2_4}$/DOX/siRNA co-delivery system. Besides, in the MCF-7S cells, which were in the absence of pump activity, the cytotoxicity of nanofibers and nanoparticles were similar, which were higher than that of free DOX (Figure 20b).

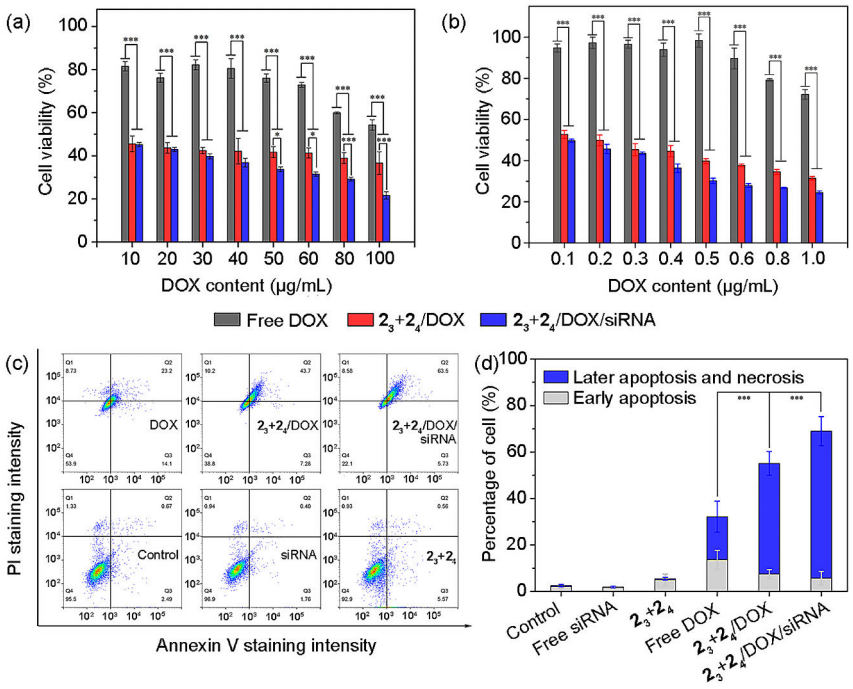

Figure 20. (a) Cell viabilities of NCI/ADR-RES cells exposed to free DOX, $\mathbf{2_3}$+$\mathbf{2_4}$/DOX, and $\mathbf{2_3}$+$\mathbf{2_4}$/DOX/siRNA for 48 h; (b) cell viabilities of MCF-7S cells exposed to free DOX, $\mathbf{2_3}$+$\mathbf{2_4}$/DOX, and $\mathbf{2_3}$+$\mathbf{2_4}$/DOX/siRNA for 24 h; (c) apoptotic effect of free DOX, siRNA, $\mathbf{2_3}$+$\mathbf{2_4}$, $\mathbf{2_3}$+$\mathbf{2_4}$/DOX, and $\mathbf{2_3}$+$\mathbf{2_4}$/DOX/siRNA on NCI/ADR-RES cells; (d) apoptosis rate and cell viability from flow cytometry test (n = 3). Data are expressed as mean values ± SD. *P<0.05, **P<0.01, and ***P<0.001. Reprinted with permission from *Cell Rep. Phys. Sci.* **2022,** *3* (11), 101150.

To further confirm the anti-MDR cancer cells effect of the nanoparticle system, Annexin V-FITC and PI were used to stain the cells incubated with different formations to determine their apoptotic efficiency by flow cytometer (Figure 20c-d). The proportion of later apoptosis and necrosis in NCR/ADR-RES cells treated with **2**$_3$+**2**$_4$/DOX/siRNA nanoparticles was 63.3 %, which was higher than that in **2**$_3$+**2**$_4$/DOX nanofibers (47.6 %) and free DOX (6.8 %). The phenomenon can be attributed to the successful delivery of siRNA, which suppressed the over-expression of pump protein in cells, resulting in the increase of accumulation of DOX and inducing cell apoptosis.[137] It should also be noted that the macrocycles (**2**$_3$+**2**$_4$) showed extremely low cytotoxicity in cells, which was similar to free siRNA.

4.2.10 Conclusion

In this chapter, we constructed a responsive macrocycle co-delivery system that delivers drugs and genes to targeted MDR cancer cells. To enhance the loading capacity of the delivery system, the arginine-modified building block **2** had ample time to allow the thiol/disulfide exchange reaction to take place and reach an equilibrium, during which the disulfide macrocycle carriers (**2**$_3$+**2**$_4$) self-assembled with the DOX to form nanofiber with high DLC. However, when the reaction was significantly accelerated, disulfide polymers were obtained from the same building block, but they were not able to encapsulate the drug. The utility of our macrocycle system was demonstrated by further loading siRNA, and the resulting co-delivery system displayed the controllable release of drug and gene, as well as improved synergistic efficacy against NCI/ADR-RES cells *in vitro*.

4.3 Fabrication of moisture-responsive actuators using dynamic covalent macrocycles and surfactants via liquid-liquid phase separation

4.3.1 Introduction

Living tissues and organs are characterized by their intricate three-dimensional (3D) structures, made up of specialized cells that interact and collaborate, enabling complex functions within a unified system. The exceptional adaptability and functionality of these 3D biological architectures have motivated extensive research into creating macroscopic materials embedded with cell-like compartments. These materials are expected to transform fields like catalysis,[146-148] sensing,[149] microreactors,[150] wearable technology,[151] and soft robotics.[152]

Conventionally, microfluidic techniques and 3D printing have been employed to fabricate these compartmentalized materials by arranging droplets into tissue-like structures.[153-155] However, these resulting materials often lack the mechanical strength required for the development of responsive smart devices,[156] due to the low density of solute molecules within the compartments. Hence, researchers have therefore explored the use of droplets generated through liquid-liquid phase separation (LLPS) to enhance the stiffness of materials, given that LLPS droplets transition from a dilute to a dense phase following thermodynamic principles.[157-159]

To achieve this objective, Ostwald ripening and coalescence, where larger droplets grow at the expense of smaller ones, undermining the materials' structural integrity and uniformity due to thermodynamic instability, is the barrier to be broken down.[160-162] Recent efforts have concentrated on methods such as external forces, surface engineering, and chemical fueling to stabilize these phase-separated droplets.[163-165] However, these approaches only offer a temporary solution; once the external energy supply stops, phenomena like Ostwald ripening and droplet coalescence resume. Over time, as the system approaches thermodynamic equilibrium, the structural integrity may falter, leading to droplet disruption.

Addressing the limitations inherent in these approaches, we propose a thermodynamic approach - a multivalent ionic hierarchical self-assembly strategy. In this system, an anionic azobenzene-derived macrocycle (**ADM**)[89] and a bolaform surfactant pentadecane-1,15-bis(trimethylammonium bromide) (**A15**) were employed to take part in the formation of coacervates with net charges (Figure 21), preventing Ostwald ripening and coalescence by finely tuning the charge ratio among components to balance repulsive forces and interactions with water. Then, the charged droplets subsequently form a colloidal hydrogel through the secondary self-assembly. This hydrogel can be processed into the moisture-responsive actuator containing cell-like compartments. Remarkably, the materials can be fabricated into

different types of actuators, which could transfer moisture change into mechanical energy. Besides, this spontaneous self-assembly process, requiring no external intervention, closely emulates natural biological tissue development processes. It highlights the immense potential of utilizing small molecules for the self-organized creation of functional structures, marking an advancement in the quest to replicate the complexity and efficiency of biological systems with synthetic materials.

4.3.2 Experimental section

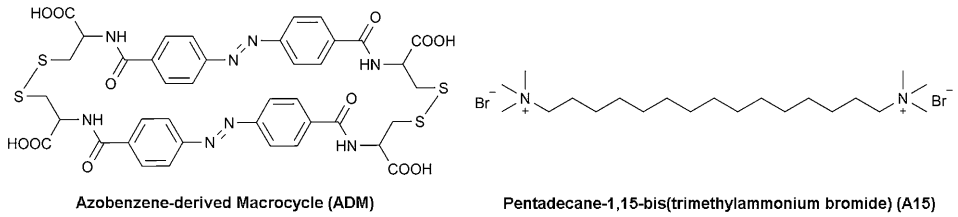

Figure 21. Molecular structure of azobenzene-derived macrocycle (**ADM**) and pentadecane-1,15-bis(trimethylammonium bromide) (**A15**).

4.3.2.1 Synthesis of macrocycles **ADM**

Azobenzene-derived macrocycle (**ADM**) was synthesized according to the previous literature.[89] The **ADM** stock solution was prepared by dissolving the sample (94.81 mg) into 800 μL of H_2O, then add NaOH solution (2000 mM, 200 μL) dropwise until totally dissolved. The final concentration of **ADM** stock solution was 100 mM.

4.3.2.2 Synthesis of bolaform surfactant **A15**

Pentadecane-1,15-bis(trimethylammonium bromide) (**A15**) was synthesized by dissolving 1,15-dibromo pentadecane in EtOH, followed by adding trimethylamine EtOH solution and reacting. The final product **A15** was obtained without purification. The **A15** stock solution was prepared by dissolving the sample (48.62 mg) into 1 mL of H_2O, and the final concentration of **A15** stock solution was 100 mM.

4.3.2.3 Preparation of **ADM**/**A15** supramolecular hydrogel

ADM/**A15** hydrogel was prepared by mixing the stock solution of **ADM** (100 mM) and **A15** (100 mM) equivalently and adjusting it into different concentrations if needed. The mixture was heated in a water bath at 60 °C until dissolved, followed by cooling to room temperature, then the orange transparent hydrogel was formed.

4.3.2.4 Preparation of **ADM/A15** film and **ADM/A15**/PI bilayer actuators

The **ADM/A15** film was fabricated by drop-coating **ADM/A15** hydrogel (30 mM) solution on a PTFE plate, followed by placing the sample in the fume hood overnight. The film was cut into different sizes of strips for experiments (Figure 22a). The **ADM/A15**/PI bilayer actuators were fabricated by drop-coating **ADM/A15** hydrogel (30 mM) solution on a PI film. After evaporating the water in the fume hood overnight, the bilayer film was cut into different shapes for experiments (Figure 22b).

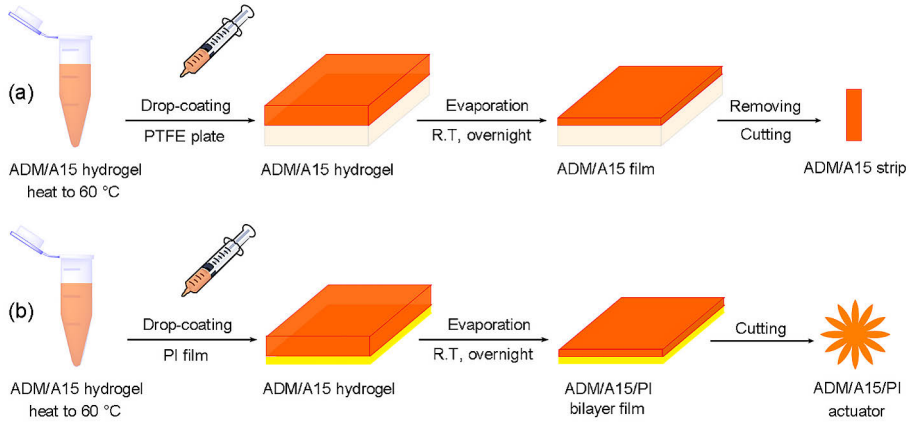

Figure 22. (a) Preparation of **ADM/A15** film; (b) preparation of **ADM/A15**/PI bilayer film.

4.3.2.5 Evaluation of humidity responsiveness of **ADM/A15** film under different RH environments

A chamber with a square hole was prepared (internal dimensions = 8.5 cm × 10.5 cm × 7 cm), and Relative Humidity (RH) in it was controlled by a humidifier and monitored by a hygrometer (Figure 23). The film was vertically taped on the edge of the hole. The processes of deformation were monitored by a camera. The performance of films under different RH was evaluated three times. Outside the chamber, RH was 30 % at room temperature.

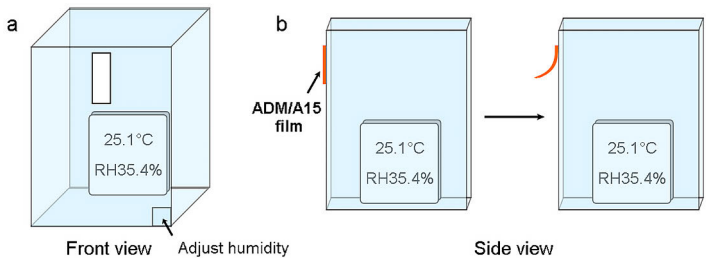

Figure 23. The glass chamber for humidity responsiveness tests. (a) Front view; (b) side view.

4.3.2.6 Evaluations of performance of piezoelectric **ADM**/**A15**/PVDF actuator

In a chamber, the prepared **ADM**/**A15** film was coupled with a commercial piezoelectric PVDF transducer (length: 4.0 cm, width: 1.6 cm), which was connected with an electrochemical workstation (PalmSens4) and monitored by using the Open Circuit Voltage-Time method. The humidity of the chamber was controlled by a humidifier and monitored by a hygrometer. In the absorption process, moisture flow was introduced inside the chamber to maintain a condition equivalent to RH = 70% environment. In the desorption process, air was introduced inside the chamber and finally the RH reached to 30%. All data were collected during three adsorption-desorption cycles.

4.3.3 Preparation of **ADM**/**A15** supramolecular hydrogel

A group of aqueous samples containing **ADM** (10 mM) and **A15** with different mole ratios were prepared (Figure 24a), and a transparent supramolecular hydrogel was obtained when the ratio of **ADM**/**A15** = 1:1. In contrast, the others were either solution or precipitation, indicating the critical role of the **ADM**/**A15** ratio in selective gelation. In another group of **ADM**/**A15** = 1:1 with different concentrations, the hydrogel could form when the concentration was higher than 10 mM (Figure 24b), indicating the critical gel concentration (CGC) was 1.64 wt%.

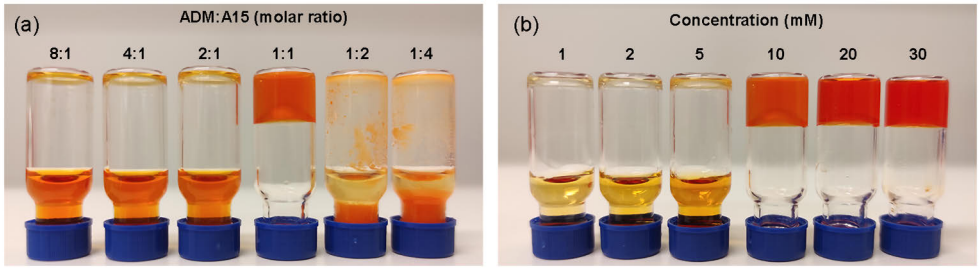

Figure 24. (a) The appearance of **ADM** (10 mM) to **A15** (pH = 11, H_2O) with different ratios after solution preparation; (b) the appearance of **ADM**/**A15** = 1/1 with different concentration (pH = 11, H_2O).

4.3.4 Structure analysis of **ADM**/**A15** supramolecular hydrogel

4.3.4.1 NMR analysis

To further understand the temperature responsiveness and molecular interactions between **ADM** and **A15** in the hydrogel, ^{1}H NMR was used to characterize the **ADM**/**A15** hydrogel. The record NMR spectra showed a significant reduction in **A15** signals within the gel state at 298 K, suggesting the self-aggregation of **A15**. Upon a gradual temperature increase to 323 K, the gel melted and distinct NMR peaks became apparent (Figure 25a). The integration of proton signals for **ADM** and **A15** at a 1: 1 mole ratio provided definitive evidence for the disassembly of the gel phase. The DOSY results revealed the presence of a single aggregate type in the solution (Figure 25b), and the diffusion coefficient of the **ADM**/**A15** complex ($D = 5.747\times10^{-10}$ m^2 s^{-1}) was notably lower than that of pure **ADM** ($D = 7.344\times10^{-10}$ m^2 s^{-1}) and **A15** ($D = 1.103\times10^{-9}$ m^2 s^{-1}) in separate solutions under the same conditions. These results indicated the stability of the **ADM**/**A15** complex when the hydrogel transitioned into a solution. In the NOESY spectrum (Figure 25c), there was a strong correlation between protons a and b from azobenzene moieties and protons 1 and 2 of **A15** because of the strong electrostatic interaction. These results demonstrated that the alkyl chain of **A15** crosses the **ADM** macrocycle, giving rise to a host-guest substructure for subsequent supramolecular polymerization leading to LLPS (Figure 25f).

4.3.4.2 FT-IR and PXRD analysis

In the analysis of PXRD, a semi-crystalline nature appeared in lyophilized **ADM**/**A15** hydrogels (Figure 25d). The peaks at 21.44° and 22.83° correspond to the π-π stacking distance of 4.14 Å and 3.89 Å, respectively. The longer distances may be attributed to the interpenetration of the alkyl chain of **A15** into the **ADM** macrocycle.[89] In the FT-IR spectrum of the lyophilized **ADM**/**A15** hydrogel (Figure 25e), the absorption of Amide I band at 1635 cm^{-1} ($\nu_{C=O}$), Amide II band at 1520 cm^{-1} (β_{N-H}) and Amide III band 1296 cm^{-1} (ν_{C-N}) of **ADM** shifted to 1594, 1490 and 1284 cm^{-1}, respectively, and a strong and broad band at 3372 cm^{-1} attributed to the O-H stretching appeared. These results indicated that hydrogen bonds between H_2O and **ADM** exist in the hydrogel.

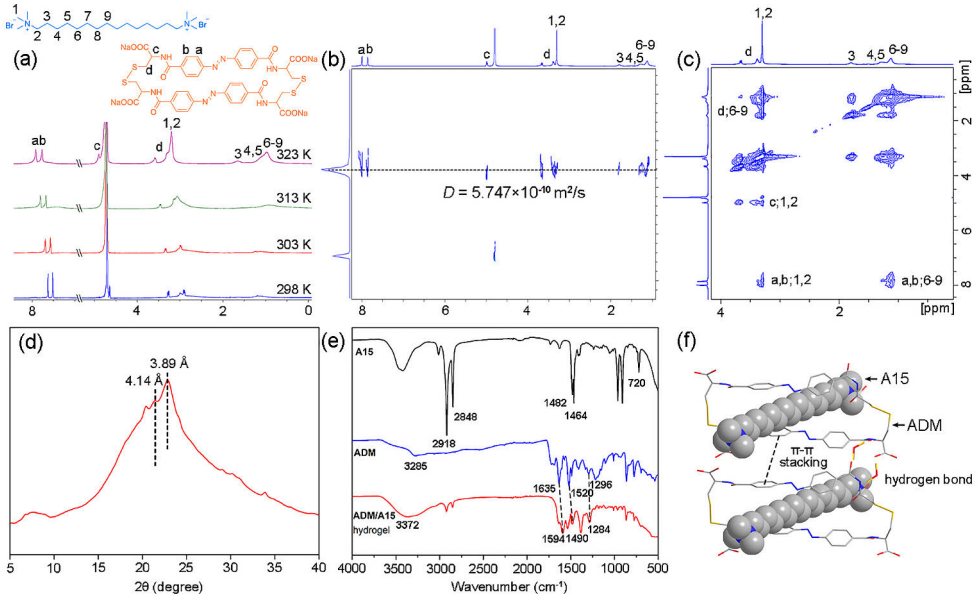

Figure 25. (a) ^{1}H NMR spectra of **ADM** (10 mM)/**A15** = 1/1 (pD = 11, D_2O) at different temperatures; (b) DOSY spectrum of **ADM** (10 mM)/**A15** = 1/1 (pD = 11, D_2O, 323 K); (c) partial 2D NOESY spectra of **ADM** (10 mM)/**A15** = 1/1 (pD = 11, D_2O, 323 K); (d) PXRD of lyophilic bulk **ADM**/**A15** supramolecular hydrogel; (e) FT-IR spectrum of **ADM**/**A15** supramolecular hydrogel in dry; (f) chemical structure illustration of **ADM**/**A15** complex.

4.3.4.3 Microscopy analysis

To analyse the substructure of the supramolecular hydrogel, the **ADM**/**A15** hydrogel was dyed with Nile red and then observed by CLSM. In Figure 26a, discrete spherical LLPS droplets were observed within the hydrogel, and their shape and size remained stable after immobilization. This observation was corroborated by the TEM, which revealed the detailed morphology of the droplets with a diameter consistently around 2 μm (Figure 26b). Contrary to previous studies on LLPS,[89] the droplets maintained a steady diameter of approximately 2 μm over an extended period of 30 days, Then, lyophilized **ADM**/**A15** hydrogel was characterized by using FE-SEM. The surface of the materials was the network structure responsible for gelation (Figure 26c).

To investigate the reason for the stable dispersion of droplets within the solution, the dilute solution of **ADM** (0.05 mM)/**A15** was dyed and observed by CLSM, and the dispersed droplets were also observed (Figure 26d). The difference in the size of droplets in hydrogel and dilute solution may be attributed to the gelation limiting the growth of the droplets. In DLS measurements, a zeta potential of **ADM**/**A15** dilute solution was -26.1 ± 3.3 mV for the droplets, in accordance with the excess negative charges at the **ADM**/**A15** stoichiometric ratio. Based on these results, we inferred that the repulsive forces between the droplets hindered the merging of droplets within the solution (Figure 26e).

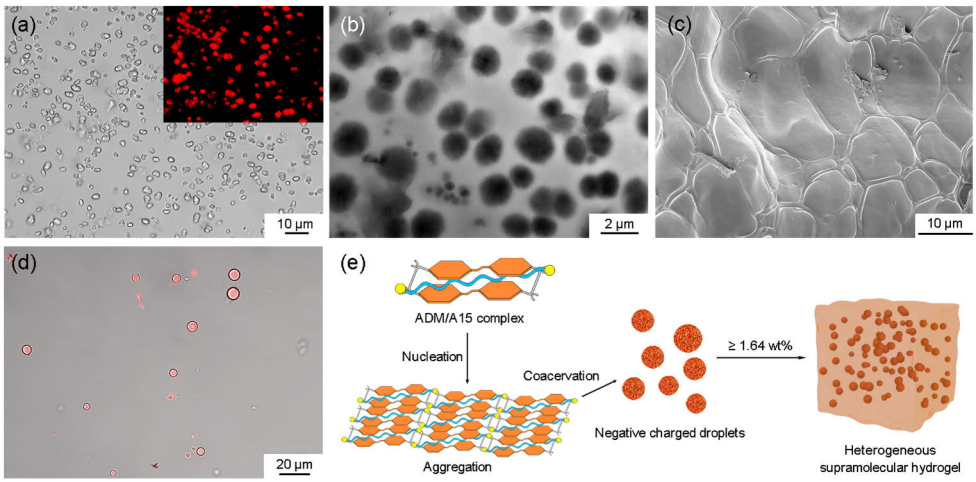

Figure 26. (a) Confocal micrograph of **ADM**/**A15** hydrogel (10 mM) stained with Nile red (1 μM), 63 ×, bar 10 μm; (b) TEM image of **ADM**/**A15** hydrogel (10 mM), bar 2 μm; (c) FE-SEM image of bulk **ADM**/**A15** hydrogel, bar 10 μm; (d) confocal micrograph of **ADM**/**A15** solution (0.5 mM) stained with Nile red (1 μM), 40 ×, bar 20 μm; (e) an illustration of the self-assembly between **ADM** and **A15** to form coacervate immobilizing in supramolecular hydrogel in one-pot strategy.

4.3.4.4 Dehydration behaviours and DSC analysis

We have shown that water molecules play a crucial role in the multivalent ionic hierarchical self-assembly process leading to gel formation, reversible to this hydration behaviour of the complex supramolecular system, we switched to examine the dehydration behaviour of the **ADM**/**A15** hydrogel. When exposed to air, all hydrogel samples could form an elastic film within 6 hours, retaining approximately 7.4 % water content (Figure 27a).

Then, DSC analysis revealed two distinct water states within the hydrogels: non-freezable bound and freezable water (Figure 27b). The part of water molecules that melts at a temperature close to 0 °C is assigned to non-freezable water, of which the mass could be obtained as Equation 3:

$$Wc = Q/\Delta H \tag{3}$$

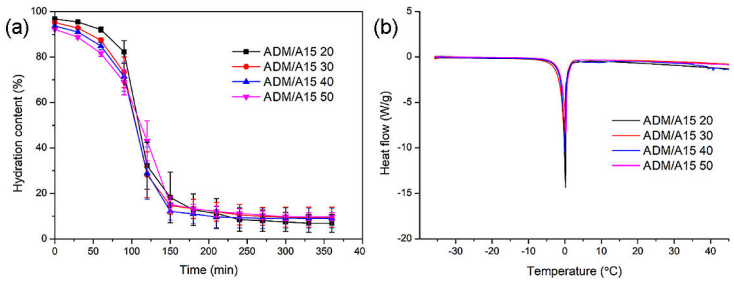

Figure 27. (a) The water dehydration kinetic curves of **ADM**/**A15** supramolecular hydrogels with different concentrations (n=3). Data are expressed as mean values ± SD; (b) DSC curves of **ADM**/**A15** supramolecular hydrogels with different concentrations.

Where ΔH is the melting enthalpy of this type of water, assumed to be the same as that of bulk water ($\Delta H = 333.5 J\ g^{-1}$), and Q is the heat absorbed during the melting process, which was calculated according to the area of the endothermic peak. The mass of non-freezable bound water was obtained from the difference between the mass of absorbed water and that of the total mass of freezable water.[166,167] The non-freezable bound water content increased to approximately 36.6 % with higher **ADM**/**A15** concentrations in the hydrogel (Table 7). This high level of non-freezable bound water underscores the strong water retention capability of the system, suggesting the hydrogel's potential for ultrasensitive water-sensing applications.

Table 7. DSC data summary of **ADM**/**A15** supramolecular hydrogels with different concentrations calculated from heating cycle.

	ADM/A15 20	ADM/A15 30	ADM/A15 40	ADM/A15 50
SUM WATER (%)	96.75	95.19	93.69	92.22
FREEZABLE WATER (%)	64.76	62.59	59.28	55.67
UNFREEZABLE WATER (%)	31.99	32.60	34.41	36.55

4.3.5 Rheology and self-healing of **ADM**/**A15** supramolecular hydrogel

The rheological properties of **ADM**/**A15** supramolecular hydrogels were evaluated by conducting dynamic rheology tests. We measured both the storage modulus (G') and loss modulus (G'') across varying strains (in an amplitude sweep) and frequencies (in a frequency sweep). In frequency sweep, both G' and G'' exhibited a gradual increase with the frequency, with G' consistently surpassing G'' across the entire measured frequency range (Figure 28a). This pattern indicates that **ADM**/**A15** hydrogel behaves as a solid-like material with a stable gel state. During the amplitude

sweep, G’ and G’’ remained constant below the yield stress, suggesting that the hydrogel’s droplet structure remained intact under stress (Figure 28b). Beyond the yield stress, G’ began to decrease, signifying the transition of the hydrogel to a free-flowing state.

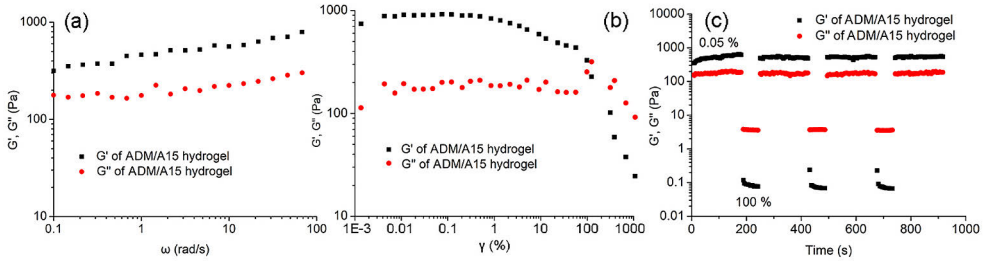

Figure 28. Rheology properties of supramolecular hydrogel. (a) Frequency sweep showing storage modulus (G’) and loss modulus (G’’) of **ADM** (30 mM)/**A15** supramolecular hydrogel; (b) amplitude sweep showing storage modulus (G’) and loss modulus (G’’) of **ADM** (30 mM)/**A15** supramolecular hydrogel; (c) cyclic strain sweeps of **ADM** (30 mM)/**A15** supramolecular hydrogel.

In the cyclic strain sweep (Figure 28c), when a small amplitude oscillatory shear (γ = 0.05%) was applied to the sample, G’ remained higher than G’’, maintaining stability over time and indicating the preservation of a fully crosslinked network. However, upon applying a strain beyond the linear viscoelastic limit (γ = 100 %), G’ and G’’ were inverted with a significant reduction, marking the transition to the sol state due to network disruption. Remarkably, after returning to a low strain (γ = 0.05 %), the sample immediately restored the gel-like state (G’ > G’’) with no notable decline observed throughout the cycles. This behaviour, typical of hydrogels with reversible non-covalent crosslinking, is rarely observed in small molecule hydrogels, as the dynamics of crosslinking formation is relatively slow. The rapid self-healing mechanism of **ADM**/**A15** hydrogel is probably facilitated by the reformation of reversible droplets within the gel network.

4.3.6 Mechanical property of **ADM/A15** film

To explore the further application of this material, we prepared **ADM**/**A15** film by drop-coating its hydrogel on a PTFE plate. The structure of **ADM**/**A15** film was characterized by PXRD, and there was only a broad peak appeared, indicating the amorphous structure of the film (Figure 29a). Then, the surface morphology of **ADM**/**A15** film was measured by using FT-SEM. As shown in Figure 29b, the surface of the film was covered with nanosheets approximately 120 nm in width and 2 μm in length, suggesting a dense structure.

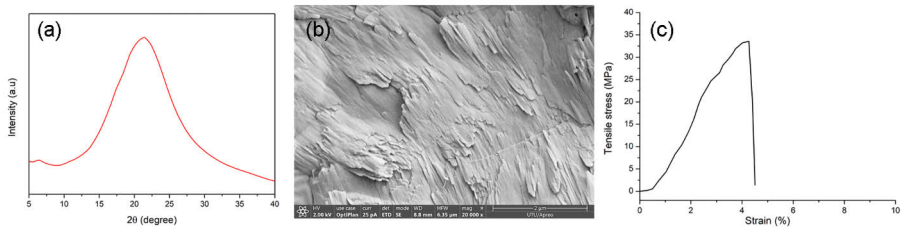

Figure 29. (a) PXRD of **ADM/A15** film; (b) FE-SEM images of **ADM/A15** film; (c) tensile-stress curves of **ADM/A15** film (thickness is 20.5 μm).

The mechanical property of **ADM/A15** was measured by conducting the tensile-stress tests. **ADM/A15** thin film (thickness was 20.5 μm) exhibited an ultimate tensile strength of 33.4 MPa and strain of 4.27 % at the break, and Young's modulus of 782.2 MPa (Figure 29c). Despite being assembled from small molecules through noncovalent interactions, the mechanical stiffness of material's is comparable to that of conventional polymers.[168]

4.3.7 Humidity responsiveness of **ADM/A15** film

Due to the hydrophilic nature of **ADM/A15**, the film could sense small moisture fluctuation even from a finger, indicating its potential to fabricate a moisture-driven device (Figure 30a). Then, the bending performance of **ADM/A15** film was investigated at different RH. The film bent over 180° within 6 s at 85 % RH and achieved a 60° angle in 20 s, even with a minimal RHs change of 5 %, showcasing immediate moisture responsiveness (Figure 30b). The deformation speed increased with higher ΔRH, which was attributed to the greater water adsorption capacity of the film at higher RH (Figure 30c). These results indicated that the instant response to moisture change of **ADM/A15** film makes it potential to be used as a humidity actuator.

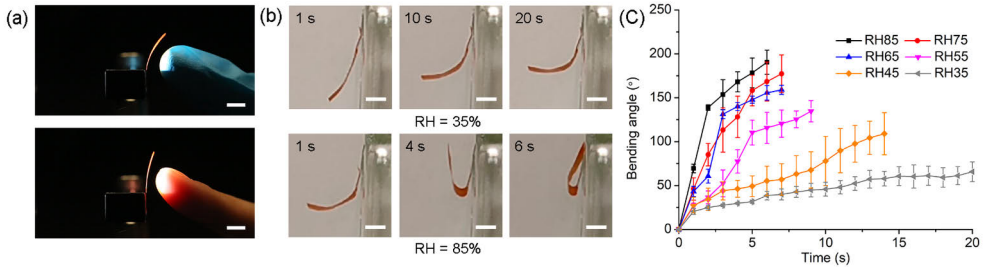

Figure 30. Humidity-responsive properties of **ADM/A15** supramolecular elastic film. (a) Photo of **ADM/A15** sensing small moisture fluctuations (fingers, response time ≈ 2 s). Scale bar: 1 cm; (b) photo of bending angle changes of **ADM/A15** film at different RH. Scale bar: 0.5 cm; (c) bending angle change vs time of **ADM/A15** film from RH = 35 % to 85 %.

4.3.8 Humidity actuator made of **ADM/A15** bilayer film

To create hygroscopic gradients, **ADM**/**A15**/PI bilayer films were fabricated by solvent evaporation. This step was necessary as the hydrophobic PI film could only allow one side of **ADM**/**A15** film to absorb water in a moisture environment, resulting in regular directional deformation.

Various shapes of **ADM**/**A15**/PI actuators were designed, and the movements at different RH were recorded by a camera. A helix-shaped bilayer film actuator demonstrated reversible bending and unbending upon changing the humidity (Figure 31a). Other shapes, i.e., crosses and stars, folded and flattened when exposed to water vapor, and recovered to their original shapes when the humidity level dropped (Figure 31b-c). Similarly, flower-shaped actuators exhibited natural-like opening and closing movements under varying RH levels (Figure 31d).

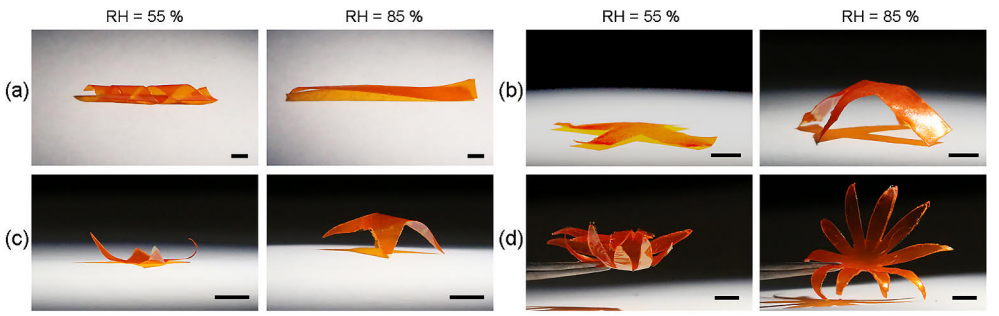

Figure 31. Moisture-driven actuators made of **ADM**/**A15**/PI bilayer film in different shape. (a) helical strip; (b) cross shape; (c) star shape; (d) flower-shape. Scale bar: 0.5 cm.

4.3.9 Electricity generator made of **ADM/A15** film

To further utilize the periodic deformation of **ADM**/**A15** film driven by humidity change, the film was coupled with a commercial piezoelectric PVDF membrane transducer to fabricate a power generator (Figure 32a), which could convert the kinetic energy from cyclic mechanical motion into electricity. Under periodic variations of RH from 30% to 70%) in the environment, the **ADM**/**A15**/PVDF actuator could repeatedly bend and unbend, resulting in producing the continuous output of an electrical voltage signal. As shown in Figure 32b, each cycle produced an open-circuit voltage of up to 30 mV for the peak output of absorption in a short time, and at least 20 cycles could be executed without an obvious decay. These results highlight the potential of **ADM**/**A15** film for the development of moisture-responsive devices and actuators that can harvest energy from the atmosphere.

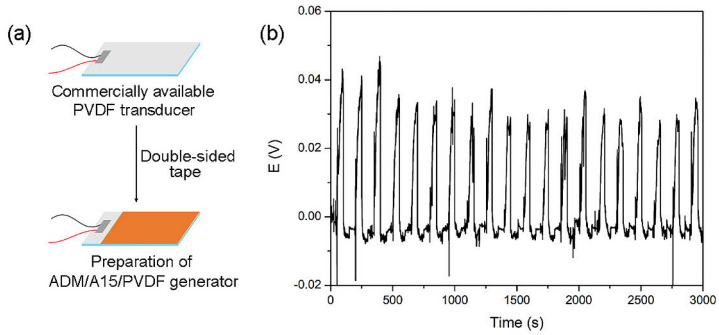

Figure 32. (a) Preparation of **ADM**/**A15**/PVDF generator; (b) open-circuit voltage signals generated by **ADM**/**A15**/PVDF at moist air exposure intervals.

4.3.10 Conclusion

In this chapter, we introduced an approach using multivalent ionic hierarchical self-assembly to create small molecule-based colloidal hydrogels. Initially, the positively charged linear surfactant **A15** threaded through the negatively charged azobenzene macrocycle **ADM** owing to hydrophobic effects. Driven by electrostatic forces and hydrogen bonding, the **ADM**/**A15** complexes then underwent supramolecular polymerization, leading to the formation of condensed droplets that separated from the water solution phase. Owing to their negative charges, these droplets did not coalesce into the bulk phase but instead self-assembled into a colloidal hydrogel. The thermal sensitivity, recyclability, and self-healing properties of the **ADM**/**A15** hydrogel are characterized, which are attributable to the reconfiguration of the droplets within the gel network. The hydrogels were also used to create extremely humidity-sensitive actuators that could be crafted into various devices. These devices demonstrate the capability of periodic control over deformation through humidity changes, enabling unidirectional motion. Furthermore, we showcased the potential for converting mechanical energy into electrical energy as a proof of concept, illustrating the possibility of energy harvesting from environmental humidity.

5 Summary

In this thesis, a series of building blocks with different functional groups were designed and synthesized. They were employed to synthesize functional macrocycles via dynamic combinatorial chemistry (DCC), which were utilized to construct different systems separately. The specific results are as follows:

In part 1, the azobenzene-derived dithiol building block **1** (disulfide exchange), β-cyclodextrin derived aldehyde **CD**, and adipic dihydrazide **L** (hydrazone exchange) were prepared in a DCL, where a "handcuffs" catenane **4-L-2CD**, consisting of a disulfide-bonded tetrameric macrocycle and a linear hydrazone **L-2CD**, became the dominant product. The thermodynamic and kinetic analysis suggested that the two minor species (**4** and **L-2CD**) functioned as templates for each other's co-amplification through noncovalent binding, resulting in a mutualistic relationship in synthesis. Moreover, the inert reaction (hydrazone formation) could be powered on by another active reaction (disulfide exchange) in the pair of orthogonal reactions in a DCL. Such a reciprocal synthesis stands for a way of coevolution of species in complex chemical systems, not only lending robust support to the molecular mutualism in DCC but also exploring the untapped potential of minor products from different reactions.

In part 2, the arginine functionalized building block **2** was used to self-synthesize into disulfide-bonded macrocycles (**2_3+2_4**), which could load DOX via assembly to form **2_3+2_4**/DOX nanofibers. The nanofibers encapsulated siRNA via electrostatic interaction to form **2_3+2_4**/DOX/siRNA nanoparticles, the nanostructures of which were explored. Due to the existence of arginine groups and disulfide bonds, **2_3+2_4**/DOX/siRNA co-delivery system exhibited redox- and pH-responsive controllable release, good biocompatibility, and better cellular endocytosis, which make it enhanced synergistic therapeutic effects against MDR cancer cells. Compared with traditional polymeric carriers, this strategy provides a one-pot method to load drugs and genes into nanoparticles to fight MDR cancer cells, revealing the possibility of a dynamic covalent macrocycle mediated delivery system in the clinical therapies.

In part 3, the anionic azobenzene-derived macrocycle (**ADM**) prepared from DCL and the bolaform surfactant pentadecane-1,15-bis(trimethylammonium

bromide) (**A15**) were employed to immobilize discrete coacervate droplets in a cell-like compartment embedded hydrogel in a multivalent ionic hierarchical self-assembly strategy. The complex structure of **ADM**/**A15** and the formation of coacervate droplets via liquid-liquid phase separation was demonstrated. The **ADM**/**A15** hydrogel exhibited thermal responsiveness, recyclability, and self-healing, attributed to the reconstruction of the droplets in the gel network system. Then, the humidity-responsive **ADM**/**A15** film was prepared from its hydrogel, of which rapid humidity response performance at different RH could drive repeatable mechanical movement. Hence, various shapes of bilayer humidity actuators (**ADM**/**A15**/PI) were fabricated that can programmable move triggered by humidity variation. Furthermore, a new type of autonomous energy transducer was designed by coupling **ADM**/**A15** film with a commercial piezoelectric PVDF membrane transducer, resulting in the transducing of mechanical energy into electricity continuously.

Overall, dynamic covalent macrocycles from DCC have garnered significant interest in a wide variety of research fields, ranging from artificial receptors, catalysts, to pharmaceutical chemistry and supramolecular materials. This thesis endeavours to construct several systems consisting of dynamic covalent macrocycles through DCC. These systems, based on functional disulfide macrocycles, have successfully explored molecular mutualism in synthetic chemistry, facilitated drug and gene co-delivery to fight against cancer cells, and the creation of heterogeneous hydrogels and smart materials. This research serves as a gateway to investigating the production of disulfide macrocycles from DCC for potential applications in various fields.

Acknowledgements

This thesis is based on experimental work performed in the MediCity Research Laboratory and Laboratory of Organic Chemistry and Chemical Biology at the Department of Chemistry, University of Turku, Finland, during the years of January 2018 to May 2024. The financial support from the Finnish Cultural Foundation, Academy of Finland, Finnish National Agency for Education, and Doctoral Programme in Exact Sciences are gratefully acknowledged.

First and foremost, I wish to express my deepest gratitude to my supervisor Dr. Jianwei Li for giving me an opportunity to pursue a doctoral degree under his guidance. I am truly impressed by his immense knowledge and experience in the field of dynamic combinatorial chemistry. Whenever I had troubles or faced problems in my research, I could knock on his door or send an email to him irrespective of time without any doubt. I would like to thank him for his continuous encouragement, thoughtful suggestions, support, and patience during these years, trust in me, and for being a great supervisor.

I am also very much grateful to my second PhD supervisor, Professor Tuomas Lönnberg for his constant guidance and help. In addition, I thank my research director, Prof. Pasi Virta for being so supportive throughout these years.

I am grateful to Professor Leonard Prins and Associate Professor Rienk Eelkema for carefully evaluating my thesis. Their valuable comments helped to improve this thesis. I am thankful to Professor Riina Aav for accepting to be my opponent.

I wish to thank all my colleagues who have been always supportive. My gratitude goes to all present and former co-workers in the MediCity Research Laboratory for maintaining a work-leisure balancing environment. I wish to thank Jinghui Yang, Xin Wang, Dr. Xiaoxia Wu, Dr. Jingjing Yu, Dr. Yu Cao, Dawei Qi, Xuncheng Shi, Dr. Qin Li, Caihong Lin, and Chong Chen. Thank you for your help and advice and for creating a pleasant working atmosphere in the lab. I am very grateful to Katri Kulmala for providing valuable help at any time. I am very grateful to Annika Kankare, Pasi Viljakainen, Mikael Wasberg and Kim Sundfors for providing valuable help with chemicals and instruments maintenance. I also wish to thank Dr. Anastassios C. Papageorgiou for PXRD measurement, Markus Peurla for TEM

imaging, and Dr. Jouko Sandholm for CLSM. I wish to thank Valtteri Viloma and Dr. Dominik Eichin for giving me guidance on Western blotting.

I also want to thank all the current and former members of the Bioorganic Group with whom I have had the honor to work in the first year: Aapo Aho, Dr. Antti Äärelä, Dr. Asmo Aro-Heinilä, Dr. Dattatraya Ukale, Dr. Heidi Korhonen, Dr. Lange Saleh, Dr. Madhuri Hande, Dr. Mikko Ora, Dr. Päivi Poijärvi-Virta, Dr. Petja Rosenqvist, Dr. Sajal Maity, Dr. Satu Mikkola, Dr. Tharun Kotammagari, Tommi Österlund, Dr. Ville Tähtinen, Dr. Vijay Gulumkar. I wish to thank Dr. Tuomas Karskela, Dr. Jari Sinkkonen, Dr. Jani Rahkila and Adj. Prof. Alex Dickens from the Instrument Center/CCMA for their help with the NMR and MS instruments, and thank Professor Jukka Lukkari for giving me instructions on electrochemical measurement. Besides, I am very grateful to Kari Loikas, Kirsi Laaksonen, Mauri Nauma and Tiina Buss for providing valuable help with chemicals, instruments and IT systems.

I take this opportunity to thank Associate Professor Hao Zeng, Jianfeng Yang, Zixuan Deng, Dr. Yi Han, Dr. Hongshuang Guo, Dr. Qi Yang, Leilei Song, Bingnan Zhou who were able to help me at Tampere University. I also give my warm thanks to all my friends in Turku for helping me have non-work-related thoughts and to relax from time to time.

I also give my warm thanks to my old friends Chao Ma and Yang Qi in China with whom I have stayed close despite the long distance between our current locations. And especially to my boyfriend, Chao Zhu, whom I have trusted when I have had doubts and who has rejoiced with me whenever there was a reason. Thank you for your special patience, support, love, and waiting for me.

A huge thank you is reserved for my elder cousin Yonghai Lv and his families: Mirva Kärki, Julian, and Joel. It has always been happy and fun to spend time with you at weekends. Mirva's pizza and pie are the best food in the world.

Last but not least, my special thanks to my grandmother Xinling. Unfortunately, you are not in the world to share this milestone, but I am very grateful for your love, care, and continuous support throughout my life. My warmest thanks are devoted to my parents, Yuquan and Xuemei. Thank you for your endless love, support, and care throughout my life!

Turku, August, 2024

Yonglei Lyu

List of References

[1] Lowe, G. Combinatorial chemistry. *Chem. Soc. Rev.* **1995**, *24* (5), 309-317. DOI: https://doi.org/10.1039/CS9952400309.

[2] Otto, S.; Furlan, R. L. E.; Sanders, J. K. M. Dynamic combinatorial chemistry. *Drug Discovery Today* **2002**, *7* (2), 117-125. DOI: https://doi.org/10.1016/s1359-6446(01)02086-4.

[3] Liu, R.; Li, X.; Lam, K. S. Combinatorial chemistry in drug discovery. *Curr. Opin. Chem. Biol.* **2017**, *38*, 117-126. DOI: https://doi.org/10.1016/j.cbpa.2017.03.017.

[4] Brouwer, A. J.; van der Linden, H. J.; Liskamp, R. M. J. Combinatorial Chemistry for Ligand Development in Catalysis: Synthesis and Catalysis Screening of Peptidosulfonamide Tweezers on the Solid Phase. *J. Org. Chem.* **2000**, *65* (6), 1750-1757. DOI: https://doi.org/10.1021/jo991628z.

[5] Fonseca, M. a. H. a.; List, B. Combinatorial chemistry and high-throughput screening for the discovery of organocatalysts. *Curr. Opin. Chem. Biol.* **2004**, *8* (3), 319-326. DOI: https://doi.org/10.1016/j.cbpa.2004.04.013.

[6] Corbett, P. T.; Leclaire, J.; Vial, L.; West, K. R.; Wietor, J.-L.; Sanders, J. K. M.; Otto, S. Dynamic Combinatorial Chemistry. *Chem. Rev.* **2006**, *106* (9), 3652-3711. DOI: https://doi.org/10.1021/cr020452p.

[7] Lehn, J.-M.; Eliseev, A. V. Dynamic combinatorial chemistry. *Science* **2001**, *291* (5512), 2331-2332. DOI: https://doi.org/10.1126/science.1060066.

[8] Lehn, J.-M. Constitutional Dynamic Chemistry: Bridge from Supramolecular Chemistry to Adaptive Chemistry. In *Constitutional Dynamic Chemistry*; 2012; pp 1-32. DOI: https://doi.org/10.1007/128_2011_256.

[9] Lehn, J.-M. From supramolecular chemistry towards constitutional dynamic chemistry and adaptive chemistry. *Chem. Soc. Rev.* **2007**, *36* (2), 151-160. DOI: https://doi.org/10.1039/B616752G.

[10] Otto, S.; Furlan, R. L. E.; Sanders, J. K. M. Selection and amplification of hosts from dynamic combinatorial libraries of macrocyclic disulfides. *Science* **2002**, *297* (5581), 590-593. DOI: https://doi.org/10.1126/science.1072361.

[11] Giuseppone, N.; Lehn, J.-M. Protonic and Temperature Modulation of Constituent Expression by Component Selection in a Dynamic Combinatorial Library of Imines. *Chem. Eur. J.* **2006**, *12* (6), 1715-1722. DOI: https://doi.org/10.1002/chem.200501038.

[12] Jouault, N.; Nguyen, R.; Rawiso, M.; Giuseppone, N.; Buhler, E. SANS, SAXS, and light scattering investigations of pH-responsive dynamic combinatorial mesophases. *Soft Matter* **2011**, *7* (10), 4787-4800. DOI: https://doi.org/10.1039/C1SM05164D.

[13] Berl, V.; Huc, I.; Lehn, J.-M.; DeCian, A.; Fischer, J. Induced Fit Selection of a Barbiturate Receptor from a Dynamic Structural and Conformational/Configurational Library. *Eur. J. Org. Chem.* **1999**, *1999* (11), 3089-3094. DOI: https://doi.org/10.1002/(SICI)1099-0690(199911)1999:11<3089::AID-EJOC3089>3.0.CO;2-4.

[14] Cai, M.; Shi, X.; Sidorov, V.; Fabris, D.; Lam, Y-F.; Davis, J T. Cation-directed self-assembly of lipophilic nucleosides: the cation's central role in the structure and dynamics of a hydrogen-bonded assembly. *Tetrahedron* **2002**, *58*, 661-671. DOI: https://doi.org/10.1016/S0040-4020(01)01101-2.

[15] Corbett, P. T.; Sanders, J. K. M.; Otto, S. Competition between Receptors in Dynamic Combinatorial Libraries: Amplification of the Fittest. *J. Am. Chem. Soc.* **2005**, *127* (26), 9390-9392. DOI: https://doi.org/10.1021/ja0509026.

[16] Grote, Z.; Scopelliti, R.; Severin, K. Adaptive Behavior of Dynamic Combinatorial Libraries Generated by Assembly of Different Building Blocks. *Angew. Chem. Int. Ed.* **2003**, *42* (32), 3821-3825. DOI: https://doi.org/10.1002/anie.200351623.

[17] Ludlow, R. F.; Otto, S. Systems chemistry. *Chem. Soc. Rev.* **2008**, *37* (1), 101-108. DOI: https://doi.org/10.1039/B611921M.

[18] Roberts, S. L.; Furlan, R. L. E.; Otto, S.; Sanders, J. K. M. Metal-ion induced amplification of three receptors from dynamic combinatorial libraries of peptide-hydrazones. *Org. Biomol. Chem.* **2003**, *1* (9), 1625-1633. DOI: https://doi.org/10.1039/B300956D.

[19] Goral, V.; Nelen, M. I.; Eliseev, A. V.; Lehn, J.-M. Double-level "orthogonal" dynamic combinatorial libraries on transition metal template. *Proc. Natl. Acad. Sci. U.S.A.* **2001**, *98* (4), 1347-1352. DOI: https://doi.org/10.1073/pnas.98.4.1347.

[20] Bhat, V. T.; Caniard, A. M.; Luksch, T.; Brenk, R.; Campopiano, D. J.; Greaney, M. F. Nucleophilic catalysis of acylhydrazone equilibration for protein-directed dynamic covalent chemistry. *Nat. Chem.* **2010**, *2* (6), 490-497. DOI: https://doi.org/10.1038/nchem.658.

[21] Vial, L.; Ludlow, R. F.; Leclaire, J.; Pérez-Fernández, R.; Otto, S. Controlling the Biological Effects of Spermine Using a Synthetic Receptor. *J. Am. Chem. Soc.* **2006**, *128* (31), 10253-10257. DOI: https://doi.org/10.1021/ja062536b.

[22] Severin, K. The Advantage of Being Virtual-Target-Induced Adaptation and Selection in Dynamic Combinatorial Libraries. *Chem. Eur. J.* **2004**, *10* (10), 2565-2580. DOI: https://doi.org/10.1002/chem.200305660.

[23] Oh, K.; Jeong, K.-S.; Moore, J. S. Folding-driven synthesis of oligomers. *Nature* **2001**, *414* (6866), 889-893. DOI: https://doi.org/10.1038/414889a.

[24] Zhang, J.; Jing, B.; Tokutake, N.; Regen, S. L. Transbilayer Complementarity of Phospholipids. A Look beyond the Fluid Mosaic Model. *J. Am. Chem. Soc.* **2004**, *126* (35), 10856-10857. DOI: https://doi.org/10.1021/ja046892a.

[25] Pal, A.; Malakoutikhah, M.; Leonetti, G.; Tezcan, M.; Colomb-Delsuc, M.; Nguyen, V. D.; van der Gucht, J.; Otto, S. Controlling the Structure and Length of Self-Synthesizing Supramolecular Polymers through Nucleated Growth and Disassembly. *Angew. Chem. Int. Ed.* **2015**, *54* (27), 7852-7856. DOI: https://doi.org/10.1002/anie.201501965.

[26] Carnall, J. M. A.; Waudby, C. A.; Belenguer, A. M.; Stuart, M. C. A.; Peyralans, J. J.-P.; Otto, S. Mechanosensitive Self-Replication Driven by Self-Organization. *Science* **2010**, *327* (5972), 1502-1506. DOI: https://doi.org/10.1126/science.1182767.

[27] Otto, S.; Furlan, R. L. E.; Sanders, J. K. M. Dynamic Combinatorial Libraries of Macrocyclic Disulfides in Water. *J. Am. Chem. Soc.* **2000**, *122* (48), 12063-12064. DOI: https://doi.org/10.1021/ja005507o.

[28] Black, S. P.; Sanders, J. K. M.; Stefankiewicz, A. R. Disulfide exchange: exposing supramolecular reactivity through dynamic covalent chemistry. *Chem. Soc. Rev.* **2014**, *43* (6), 1861-1872. DOI: https://doi.org/10.1039/C3CS60326A.

[29] Carey, F. A.; Sundberg, R. J., *Advanced Organic Chemistry: Part A: Structure and Mechanisms*. Springer Science & Business Media, 2007.

[30] Dirksen, A.; Dirksen, S.; Hackeng, T. M.; Dawson, P. E. Nucleophilic Catalysis of Hydrazone Formation and Transimination: Implications for Dynamic Covalent Chemistry. *J. Am. Chem. Soc.* **2006**, *128* (49), 15602-15603. DOI: https://doi.org/10.1039/10.1021/ja067189k.

[31] Roberts, S. L.; Furlan, R. L. E.; Cousins, G. R. L.; Sanders, J. K. M. Simultaneous selection, amplification and isolation of a pseudo-peptide receptor by an immobilised N-methyl ammonium ion template. *Chem. Commun.* **2002**, (9), 938-939. DOI: https://doi.org/10.1039/B201465C.

[32] Liu, J.; West, K. R.; Bondy, C. R.; Sanders, J. K. M. Dynamic combinatorial libraries of hydrazone -linked pseudo-peptides: dependence of diversity on building block structure and chirality. *Org. Biomol. Chem.* **2007**, *5* (5), 778-786. DOI: https://doi.org/10.1039/B617217B.

[33] Crego Calama, M.; Timmerman, P.; N. Reinhoudt, D.; Hulst, R.; Fokkens, R.; M. M. Nibbering, N. Libraries of non-covalent hydrogen-bonded assemblies; combinatorial synthesis of supramolecular systems. *Chem. Commun.* **1998**, (9), 1021-1022. DOI: https://doi.org/10.1039/A801028E.

[34] Telfer, S. G.; Yang, X.-J.; Williams, A. F. Complexes of 5,5′-aminoacido-substituted 2,2′-bipyridyl ligands: control of diastereoselectivity with a pH switch and a chloride-responsive combinatorial library. *Dalton Trans.* **2004**, (5), 699-705. DOI: https://doi.org/10.1039/B315232D.

[35] Campos-Fernández, C. S.; Schottel, B. L.; Chifotides, H. T.; Bera, J. K.; Bacsa, J.; Koomen, J. M.; Russell, D. H.; Dunbar, K. R. Anion Template Effect on the Self-Assembly and Interconversion of Metallacyclophanes. *J. Am. Chem. Soc.* **2005**, *127* (37), 12909-12923. DOI: https://doi.org/10.1021/ja052108q.

[36] Stone, M. T.; Moore, J. S. Supramolecular Chelation Based on Folding. *J. Am. Chem. Soc.* **2005**, *127* (16), 5928-5935. DOI: https://doi.org/10.1021/ja050713n.

[37] Stulz, E.; Scott, S. M.; Bond, A. D.; Teat, S. J.; Sanders, J. K. M. Selection and Amplification of Mixed-Metal Porphyrin Cages from Dynamic Combinatorial Libraries. *Chem. Eur. J.* **2003**, *9* (24), 6039-6048. DOI: https://doi.org/10.1002/chem.200305265.

[38] Stulz, E.; Scott, S. M.; Ng, Y.-F.; Bond, A. D.; Teat, S. J.; Darling, S. L.; Feeder, N.; Sanders, J. K. M. Construction of Multiporphyrin Arrays Using Ruthenium and Rhodium Coordination to Phosphines. *Inorg. Chem.* **2003**, *42* (20), 6564-6574. DOI: https://doi.org/10.1021/ic034699w.

[39] A. Brady, P.; K. M. Sanders, J. Thermodynamically-controlled cyclisation and interconversion of oligocholates: metal ion templated 'living' macrolactonisation. *J. Chem. Soc., Perkin Trans. 1,* **1997**, (21), 3237-3254. DOI: https://doi.org/10.1039/A703390G.

[40] Hasenknopf, B.; Lehn, J.-M.; Boumediene, N.; Dupont-Gervais, A.; Van Dorsselaer, A.; Kneisel, B.; Fenske, D. Self-Assembly of Tetra- and Hexanuclear Circular Helicates. *J. Am. Chem. Soc.* **1997**, *119* (45), 10956-10962. DOI: https://doi.org/10.1021/ja971204r.

[41] Lehn, J.-M. Dynamic Combinatorial Chemistry and Virtual Combinatorial Libraries. *Chem. Eur. J.* **1999**, *5* (9), 2455-2463. DOI: https://doi.org/10.1002/(SICI)1521-3765(19990903)5:9<2455::AID-CHEM2455>3.0.CO;2-H.

[42] Swann, P. G.; Casanova, R. A.; Desai, A.; Frauenhoff, M. M.; Urbancic, M.; Slomczynska, U.; Hopfinger, A. J.; Le Breton, G. C.; Venton, D. L. Nonspecific protease-catalyzed hydrolysis/synthesis of a mixture of peptides: Product diversity and ligand amplification by a molecular trap. *Pept. Sci.* **1996**, *40* (6), 617-625. DOI: https://doi.org/10.1002/(SICI)1097-0282(1996)40:6<617::AID-BIP3>3.0.CO;2-Z.

[43] Klekota, B.; Hammond, M. H.; Miller, B. L. Generation of novel DNA-binding compounds by selection and amplification from self-assembled combinatorial libraries. *Tetrahedron Lett.* **1997**, *38* (50), 8639-8642. DOI: https://doi.org/10.1016/S0040-4039(97)10374-4.

[44] Shepodd, T. J.; Petti, M. A.; Dougherty, D. A. Molecular recognition in aqueous media: donor-acceptor and ion-dipole interactions produce tight binding for highly soluble guests. *J. Am. Chem. Soc.* **1988**, *110* (6), 1983-1985. DOI: https://doi.org/10.1021/ja00214a063.

[45] Forman, J. E.; Barrans, R. E., Jr.; Dougherty, D. A. Circular dichroism studies of molecular recognition with cyclophane hosts in aqueous media. *J. Am. Chem. Soc.* **1995**, *117* (36), 9213-9228. DOI: https://doi.org/10.1021/ja00141a014.

[46] Ngola, S. M.; Kearney, P. C.; Mecozzi, S.; Russell, K.; Dougherty, D. A. A Selective Receptor for Arginine Derivatives in Aqueous Media. Energetic Consequences of Salt Bridges That Are Highly Exposed to Water. *J. Am. Chem. Soc.* **1999**, *121* (6), 1192-1201. DOI: https://doi.org/10.1021/ja982499r.

[47] Corbett, P. T.; Tong, L. H.; Sanders, J. K. M.; Otto, S. Diastereoselective Amplification of an Induced-Fit Receptor from a Dynamic Combinatorial Library. *J. Am. Chem. Soc.* **2005**, *127* (25), 8902-8903. DOI: https://doi.org/10.1021/ja050790i.

[48] Bakker, J. M.; Langford, S. J.; Latter, M. J.; Lee, K. A.; Woodward, C. P. Template-directed assembly of a macrocyclic porphyrin tetramer using olefin metathesis. *Aust. J. Chem.* **2005**, *58* (11), 757-761. DOI: https://doi.org/10.1071/CH05262.

[49] Mullins, A. G.; Pinkin, N. K.; Hardin, J. A.; Waters, M. L. Achieving High Affinity and Selectivity for Asymmetric Dimethylarginine by Putting a Lid on a Box. *Angew. Chem. Int. Ed.* **2019**, *58*, 5282-5285. DOI: https://doi.org/10.1002/ange.201814645.

[50] Brisig, B.; Sanders, J. K. M.; Otto, S. Selection and Amplification of a Catalyst from a Dynamic Combinatorial Library. *Angew. Chem. Int. Ed.* **2003**, *42* (11), 1270-1273. DOI: https://doi.org/10.1002/ange.200390297.

[51] Vial, L.; Sanders, J. K. M.; Otto, S. A catalyst for an acetal hydrolysis reaction from a dynamic combinatorial library. *New J. Chem.* **2005**, *29* (8), 1001-1003. DOI: https://doi.org/10.1039/B505316A.

[52] He, M.; Lehn, J. M. Metal Cation-Driven Dynamic Covalent Formation of Imine and Hydrazone Ligands Displaying Synergistic Co-catalysis and Auxiliary Amine Effects. *Chem. Eur. J.* **2021**, 27, 7516-7524. DOI: https://doi.org/10.1002/chem.202100662.

[53] Pillai, O.; Panchagnula, R. Polymers in drug delivery. *Curr. Opin. Chem. Biol.* **2001**, *5* (4), 447-451. DOI: https://doi.org/10.1016/S1367-5931(00)00227-1.

[54] Sung, Y. K.; Kim, S. W. Recent advances in polymeric drug delivery systems. *Biomaterials Research* **2020**, *24* (1), 12. DOI: https://doi.org/10.1186/s40824-020-00190-7.

[55] Mitchell, M. J.; Billingsley, M. M.; Haley, R. M.; Wechsler, M. E.; Peppas, N. A.; Langer, R. Engineering precision nanoparticles for drug delivery. *Nat. Rev. Drug Discovery* **2021**, *20* (2), 101-124. DOI: https://doi.org/10.1038/s41573-020-0090-8.

[56] Peyret, A.; Ibarboure, E.; Pippa, N.; Lecommandoux, S. Liposomes in Polymersomes: Multicompartment System with Temperature-Triggered Release. *Langmuir* **2017**, *33* (28), 7079-7085. DOI: https://doi.org/10.1021/acs.langmuir.7b00655.

[57] Xu, Z. P.; Zeng, Q. H.; Lu, G. Q.; Yu, A. B. Inorganic nanoparticles as carriers for efficient cellular delivery. *Chem. Eng. Sci.* **2006**, *61* (3), 1027-1040. DOI: https://doi.org/10.1016/j.ces.2005.06.019.

[58] Jain, R. K.; Stylianopoulos, T. Delivering nanomedicine to solid tumors. *Nat. Rev. Clin. Oncol.* **2010**, *7* (11), 653-664. DOI: https://doi.org/10.1038/nrclinonc.2010.139.

[59] Knop, K.; Hoogenboom, R.; Fischer, D.; Schubert, U. S. Poly(ethylene glycol) in Drug Delivery: Pros and Cons as Well as Potential Alternatives. *Angew. Chem. Int. Ed.* **2010**, *49* (36), 6288-6308. DOI: https://doi.org/10.1002/anie.200902672.

[60] Amaldoss, M. J. N.; Yang, J.-L.; Koshy, P.; Unnikrishnan, A.; Sorrell, C. C. Inorganic nanoparticle-based advanced cancer therapies: Promising combination strategies. *Drug Discovery Today* **2022**, *27* (12), 103386. DOI: https://doi.org/10.1016/j.drudis.2022.103386.

[61] Ulrich, S. Growing Prospects of Dynamic Covalent Chemistry in Delivery Applications. *Acc. Chem. Res.* **2019**, *52* (2), 510-519. DOI: https://doi.org/10.1021/acs.accounts.8b00591.

[62] Tong, R.; Tang, L.; Ma, L.; Tu, C.; Baumgartner, R.; Cheng, J. Smart chemistry in polymeric nanomedicine. *Chem. Soc. Rev.* **2014**, *43* (20), 6982-7012. DOI: https://doi.org/10.1039/C4CS00133H.

[63] Zhu, Q.; Saeed, M.; Song, R.; Sun, T.; Jiang, C.; Yu, H. Dynamic covalent chemistry-regulated stimuli-activatable drug delivery systems for improved cancer therapy. *Chin. Chem. Lett.* **2020**, *31* (5), 1051-1059. DOI: https://doi.org/10.1016/j.cclet.2019.12.002.

[64] Cao, Y.; Yang, J.; Eichin, D.; Zhao, F.; Qi, D.; Kahari, L.; Jia, C.; Peurla, M.; Rosenholm, J. M.; Zhao, Z.; Jalkanen, S.; Li, J. Self-Synthesizing Nanorods from Dynamic Combinatorial Libraries against Drug Resistant Cancer. *Angew. Chem. Int. Ed.* **2021**, *60* (6), 3062-3070. DOI: https://doi.org/10.1002/anie.202010937.

[65] Hu, J.; Gupta, S. K.; Ozdemir, J.; Beyzavi, H. Applications of Dynamic Covalent Chemistry Concept toward Tailored Covalent Organic Framework Nanomaterials: A Review. *ACS Appl. Nano Mater.* **2020**, *3* (7), 6239-6269. DOI: https://doi.org/10.1021/acsanm.0c01327.

[66] Rogge, S. M. J.; Bavykina, A.; Hajek, J.; Garcia, H.; Olivos-Suarez, A. I.; Sepúlveda-Escribano, A.; Vimont, A.; Clet, G.; Bazin, P.; Kapteijn, F.; Daturi, M.; Ramos-Fernandez, E. V.; Llabrés i Xamena, F. X.; Van Speybroeck, V.; Gascon, J. Metal-organic and covalent organic frameworks as single-site catalysts. *Chem. Soc. Rev.* **2017**, *46* (11), 3134-3184. DOI: https://doi.org/10.1039/C7CS00033B.

[67] Hu, H.; Yan, Q.; Ge, R.; Gao, Y. Covalent organic frameworks as heterogeneous catalysts. *Chin. J. Catal.* **2018**, *39* (7), 1167-1179. DOI: https://doi.org/10.1016/S1872-2067(18)63057-8.

[68] Zhang, T.; Xing, G.; Chen, W.; Chen, L. Porous organic polymers: a promising platform for efficient photocatalysis. *Mater. Chem. Front.* **2020**, *4* (2), 332-353. DOI: https://doi.org/10.1039/C9QM00633H.

[69] Wang, Z.; Zhang, S.; Chen, Y.; Zhang, Z.; Ma, S. Covalent organic frameworks for separation applications. *Chem. Soc. Rev.* **2020**, *49* (3), 708-735. DOI: https://doi.org/10.1039/C9CS00827F.

[70] Fu, J.; Liu, J.-Y.; Zhang, G.-H.; Zhu, Q.-H.; Wang, S.-L.; Qin, S.; He, L.; Tao, G.-H. Boost of Gas Adsorption Kinetics of Covalent Organic Frameworks via Ionic Liquid Solution Process. *Small* **2023**, *19* (39), 2302570. DOI: https://doi.org/10.1002/smll.202302570.

[71] Zhu, J.; Wen, W.; Tian, Z.; Zhang, X.; Wang, S. Covalent organic framework: A state-of-the-art review of electrochemical sensing applications. *Talanta* **2023**, *260*, 124613. DOI: https://doi.org/10.1016/j.talanta.2023.124613.

[72] Hosseini Monjezi, B.; Kutonova, K.; Tsotsalas, M.; Henke, S.; Knebel, A. Current Trends in Metal–Organic and Covalent Organic Framework Membrane Materials. *Angew. Chem. Int. Ed.* **2021**, *60* (28), 15153-15164. DOI: https://doi.org/10.1002/anie.202015790.

[73] Qian, H.-L.; Wang, Y.; Yan, X.-P. Covalent organic frameworks for environmental analysis. *TrAC, Trends Anal. Chem.* **2022**, *147*, 116516. DOI: https://doi.org/10.1016/j.trac.2021.116516.

[74] He, X.; Jiang, Z.; Akakuru, O. U.; Li, J.; Wu, A. Nanoscale covalent organic frameworks: from controlled synthesis to cancer therapy. *Chem. Commun.* **2021**, *57* (93), 12417-12435. DOI: https://doi.org/10.1039/D1CC04846E.

[75] Yazdani, H.; Shahbazi, M.-A.; Varma, R. S. 2D and 3D Covalent Organic Frameworks: Cutting-Edge Applications in Biomedical Sciences. *ACS Appl. Bio Mater.* **2022**, *5* (1), 40-58. DOI: https://doi.org/10.1021/acsabm.1c01015.

[76] Côté, A. P.; Benin, A. I.; Ockwig, N. W.; O'Keeffe, M.; Matzger, A. J.; Yaghi, O. M. Porous, Crystalline, Covalent Organic Frameworks. *Science* **2005**, *310*, 1166. DOI: https://doi.org/10.1126/science.1120411.

[77] Spitler, E. L.; Dichtel, W. R. Lewis acid-catalysed formation of two-dimensional phthalocyanine covalent organic frameworks. *Nat. Chem.* **2010**, *2* (8), 672-677. DOI: https://doi.org/10.1038/nchem.695.

[78] Uribe-Romo, F. J.; Hunt, J. R.; Furukawa, H.; Klöck, C.; O'Keeffe, M.; Yaghi, O. M. A Crystalline Imine-Linked 3-D Porous Covalent Organic Framework. *J. Am. Chem. Soc.* **2009**, *131*, 4570-4571. DOI: https://doi.org/10.1021/ja8096256.

[79] Uribe-Romo, F. J.; Doonan, C. J.; Furukawa, H.; Oisaki, K.; Yaghi, O. M. Crystalline Covalent Organic Frameworks with Hydrazone Linkages. *J. Am. Chem. Soc.* **2011**, *133*, 11478-11481. DOI: https://doi.org/10.1021/ja204728y.

[80] Giri, A.; Shreeraj, G.; Dutta, T. K.; Patra, A. Transformation of an Imine Cage to a Covalent Organic Framework Film at the Liquid–Liquid Interface. *Angew. Chem. Int. Ed.* **2023**, *62* (23), e202219083. DOI: https://doi.org/10.1002/ange.202219083.

[81] Miyata, T. Preparation of smart soft materials using molecular complexes. *Polym. J.* **2010**, *42* (4), 277-289. DOI: https://doi.org/10.1038/pj.2010.12.

[82] Du, X.; Zhou, J.; Shi, J.; Xu, B. Supramolecular Hydrogelators and Hydrogels: From Soft Matter to Molecular Biomaterials. *Chem. Rev.* **2015**, *115* (24), 13165-13307. DOI: https://doi.org/10.1021/acs.chemrev.5b00299.

[83] Peppas, N. A., *Hydrogels in Medicine and Pharmacy*. CRC press Boca Raton, FL, 1986.

[84] DeRossi, D.; Kajiwara, K.; Osada, Y.; Yamauchi, A., Polymer gels. In *Fundamentals and Biomedical Applications;* 1991.

[85] Miyata, T., Gels and interpenetrating polymer networks. In *Supramolecular design for biological applications*, CRC Press, 2002, pp 109-150. eBook ISBN 9780429121982.

[86] Pal, A.; Malakoutikhah, M.; Leonetti, G.; Tezcan, M.; Colomb-Delsuc, M.; Nguyen, V. D.; van der Gucht, J.; Otto, S. Controlling the Structure and Length of Self-Synthesizing Supramolecular Polymers through Nucleated Growth and Disassembly. *Angew. Chem. Int. Ed.* **2015**, *54* (27), 7852-7856. DOI: https://doi.org/10.1002/anie.201501965.

[87] Li, J.; Carnall, J. M. A.; Stuart, M. C. A.; Otto, S. Hydrogel formation upon photoinduced covalent capture of macrocycle stacks from dynamic combinatorial libraries. *Angew. Chem. Int. Ed.* **2011**, *50* (36), 8384-8386. DOI: https://doi.org/10.1002/anie.201103297.

[88] Nguyen, V. D.; Pal, A.; Snijkers, F.; Colomb-Delsuc, M.; Leonetti, G.; Otto, S.; van der Gucht, J. Multi-step control over self-assembled hydrogels of peptide-derived building blocks and a polymeric cross-linker. *Soft Matter* **2016**, *12* (2), 432-440. DOI: https://doi.org/10.1039/C5SM02088C.

[89] Yu, J.; Qi, D.; Mäkilä, E.; Lassila, L.; Papageorgiou, A. C.; Peurla, M.; Rosenholm, J. M.; Zhao, Z.; Vallittu, P.; Jalkanen, S.; Jia, C.; Li, J. Small-Molecule-based Supramolecular Plastics Mediated by Liquid-Liquid Phase Separation. *Angew. Chem. Int. Ed.* **2022**, *61* (39), e202204611. DOI: https://doi.org/10.1002/ange.202204611.

[90] Holland, J. N.; Bronstein, J. L. Mutualism. In *Encyclopedia of Ecology*, Jørgensen, S. E.; Fath, B. D., Eds. Academic Press, Oxford, 2008, pp 2485-2491.

[91] Lanier, K. A.; Petrov, A. S.; Williams, L. D. The Central Symbiosis of Molecular Biology: Molecules in Mutualism. *J. Mol. Evol.* **2017**, *85* (1), 8-13. DOI: https://doi.org/10.1007/s00239-017-9804-x.

[92] Frenkel-Pinter, M.; Haynes, J. W.; Mohyeldin, A. M.; C, M.; Sargon, A. B.; Petrov, A. S.; Krishnamurthy, R.; Hud, N. V.; Williams, L. D.; Leman, L. J. Mutually stabilizing interactions between proto-peptides and RNA. *Nat. Commun.* **2020**, *11* (1), 3137. DOI: https://doi.org/10.1038/s41467-020-16891-5.

[93] Gilbert, W. Origin of life: The RNA world. *Nature* **1986**, *319* (6055), 618-618. DOI: https://doi.org/10.1038/319618a0.

[94] Higgs, P. G.; Lehman, N. The RNA World: molecular cooperation at the origins of life. *Nat. Rev. Genet.* **2015**, *16* (1), 7-17. DOI: https://doi.org/10.1038/nrg3841.

[95] Ruiz-Mirazo, K.; Briones, C.; de la Escosura, A. Prebiotic Systems Chemistry: New Perspectives for the Origins of Life. *Chem. Rev.* **2014**, *114* (1), 285-366. DOI: https://doi.org/10.1021/cr2004844.

[96] Leslie E, O. Prebiotic chemistry and the origin of the RNA world. *Crit. Rev. Biochem. Mol. Biol.* **2004**, *39* (2), 99-123. DOI: https://doi.org/10.1080/10409230490460765.

[97] Neveu, M.; Kim, H.-J.; Benner, S. A. The "Strong" RNA World Hypothesis: Fifty Years Old. *Astrobiology* **2013**, *13* (4), 391-403. DOI: https://doi.org/10.1089/ast.2012.0868.

[98] Rha, A. K.; Das, D.; Taran, O.; Ke, Y.; Mehta, A. K.; Lynn, D. G. Electrostatic Complementarity Drives Amyloid/Nucleic Acid Co-Assembly. *Angew. Chem. Int. Ed.* **2020**, *59* (1), 358-363. DOI: https://doi.org/10.1002/anie.201907661.

[99] Herschlag, D.; Khosla, M.; Tsuchihashi, Z.; Karpel, R. L. An RNA chaperone activity of non-specific RNA binding proteins in hammerhead ribozyme catalysis. *EMBO J.* **1994**, *13* (12), 2913-2924. DOI: https://doi.org/10.1002/j.1460-2075.1994.tb06586.x.

[100] Bergstrom, R. C.; Mayfield, L. D.; Corey, D. R. A bridge between the RNA and protein worlds? *Chem. Biol.* **2001**, *8* (2), 199-205. DOI: https://doi.org/10.1016/S1074-5521(01)00004-7.

[101] Carny, O.; Gazit, E. Creating Prebiotic Sanctuary: Self-Assembling Supramolecular Peptide Structures Bind and Stabilize RNA. *Origins Life Evol. Biospheres* **2011**, *41* (2), 121-132. DOI: https://doi.org/10.1007/s11084-010-9219-9.

[102] Tagami, S.; Attwater, J.; Holliger, P. Simple peptides derived from the ribosomal core potentiate RNA polymerase ribozyme function. *Nat. Chem.* **2017**, *9* (4), 325-332. DOI: https://doi.org/10.1038/nchem.2739.

[103] Islam, S.; Bučar, D.-K.; Powner, M. W. Prebiotic selection and assembly of proteinogenic amino acids and natural nucleotides from complex mixtures. *Nat. Chem.* **2017**, *9* (6), 584-589. DOI: https://doi.org/10.1038/nchem.2703.

[104] Patel, B. H.; Percivalle, C.; Ritson, D. J.; Duffy, C. D.; Sutherland, J. D. Common origins of RNA, protein and lipid precursors in a cyanosulfidic protometabolism. *Nat. Chem.* **2015**, *7* (4), 301-307. DOI: https://doi.org/10.1038/nchem.2202.

[105] Lyu, Y., Hu, Y., Yang, J., Wang, X., Li, J. Mutualistic Synthesis from Orthogonal Dynamic Covalent Reactions. *Angew. Chem. Int. Ed.* **2024**, e202412020. DOI: https://doi.org/10.1002/anie.202412020.

[106] Li, J.; Nowak, P.; Fanlo-Virgós, H.; Otto, S. Catenanes from catenanes: quantitative assessment of cooperativity in dynamic combinatorial catenation. *Chem. Sci.* **2014**, *5* (12), 4968-4974. DOI: https://doi.org/10.1039/C4SC01998A.

[107] Petter, R. C.; Salek, J. S.; Sikorski, C. T.; Kumaravel, G.; Lin, F. T. Cooperative binding by aggregated mono-6-(alkylamino)-beta-cyclodextrins. *J. Am. Chem. Soc.* **1990**, *112* (10), 3860-3868. DOI: https://doi.org/10.1021/ja00166a021.

[108] Liu, Y.; Fan, Z.; Zhang, H.-Y.; Yang, Y.-W.; Ding, F.; Liu, S.-X.; Wu, X.; Wada, T.; Inoue, Y. Supramolecular Self-Assemblies of β-Cyclodextrins with Aromatic Tethers: Factors Governing the Helical Columnar versus Linear Channel Superstructures. *J. Org. Chem.* **2003**, *68* (22), 8345-8352. DOI: https://doi.org/10.1021/jo034632q.

[109] Dirksen, A.; Dawson, P. E. Rapid Oxime and Hydrazone Ligations with Aromatic Aldehydes for Biomolecular Labeling. *Bioconjugate Chem.* **2008**, *19* (12), 2543-2548. DOI: 10.1021/bc800310p.

[110] Rayo, J.; Amara, N.; Krief, P.; Meijler, M. M. Live Cell Labeling of Native Intracellular Bacterial Receptors Using Aniline-Catalyzed Oxime Ligation. *J. Am. Chem. Soc.* **2011**, *133* (19), 7469-7475. DOI: 10.1021/ja200455d.

[111] Kool, E. T.; Park, D.-H.; Crisalli, P. Fast Hydrazone Reactants: Electronic and Acid/Base Effects Strongly Influence Rate at Biological Ph. *J. Am. Chem. Soc.* **2013**, *135* (47), 17663-17666. DOI: https://doi.org/10.1021/ja407407h.

[112] Armspach, D.; Ashton, P. R.; Moore, C. P.; Spencer, N.; Stoddart, J. F.; Wear, T. J.; Williams, D. J. The Self-Assembly of Catenated Cyclodextrins. *Angew. Chem. Int. Ed.* **1993**, *32*, 854-858. DOI: https://doi.org/10.1002/anie.199308541.

[113] Lim, C. W.; Sakamoto, S.; Yamaguchi, K.; Hong, J.-I. Versatile Formation of [2]Catenane and [2]Pseudorotaxane Structures; Threading and Noncovalent Stoppering by a Self-Assembled Macrocycle. *Org. Lett.* **2004**, *6* (7), 1079-1082. DOI: https://doi.org/10.1021/ol036127l.

[114] Ng, A. W. H.; Lai, S. K.-M.; Yee, C.-C.; Au-Yeung, H. Y. Macrocycle Dynamics in a Branched [8]Catenane Controlled by Three Different Stimuli in Three Different Regions. *Angew. Chem. Int. Ed.* **2022**, *61* (1), e202110200. DOI: https://doi.org/10.1002/anie.202110200.

[115] Ng, A. W. H.; Leung, Y. H.; Au-Yeung, H. Y. Dynamics of mechanically bonded macrocycles in radial hetero[4]catenane isomers. *Org. Chem. Front.* **2021**, *8* (10), 2182-2189. DOI: https://doi.org/10.1039/D0QO01658F.

[116] Zhang, D.; Nie, Y.; Saha, M. L.; He, Z.; Jiang, L.; Zhou, Z.; Stang, P. J. Photoreversible [2] Catenane via the Host–Guest Interactions between a Palladium Metallacycle and β-Cyclodextrin. *Inorg. Chem.* **2015**, *54* (24), 11807-11812. DOI: https://doi.org/10.1021/acs.inorgchem.5b01987.

[117] Onagi, H.; Carrozzini, B.; Cascarano, G. L.; Easton, C. J.; Edwards, A. J.; Lincoln, S. F.; Rae, A. D. Separated and Aligned Molecular Fibres in Solid State Self-Assemblies of Cyclodextrin

[2]Rotaxanes. *Chem. Eur. J.* **2003**, *9* (24), 5971-5977. DOI: https://doi.org/10.1002/chem.200305279.

[118] Ludlow, R. F.; Liu, J.; Li, H.; Roberts, S. L.; Sanders, J. K. M.; Otto, S. Host–Guest Binding Constants Can Be Estimated Directly from the Product Distributions of Dynamic Combinatorial Libraries. *Angew. Chem. Int. Ed.* **2007**, *46* (30), 5762-5764. DOI: https://doi.org/10.1002/anie.200700292.

[119] Hunt, R. A. R.; Ludlow, R. F.; Otto, S. Estimating Equilibrium Constants for Aggregation from the Product Distribution of a Dynamic Combinatorial Library. *Org. Lett.* **2009**, *11* (22), 5110-5113. DOI: https://doi.org/10.1021/ol901656x.

[120] Yang, S.; Schaeffer, G.; Mattia, E.; Markovitch, O.; Liu, K.; Hussain, A. S.; Ottelé, J.; Sood, A.; Otto, S. Chemical Fueling Enables Molecular Complexification of Self-Replicators. *Angew. Chem. Int. Ed.* **2021**, *60*, 11344-11349. DOI: https://doi.org/10.1002/ange.202016196.

[121] Liu, B.; Wu, J.; Geerts, M.; Markovitch, O.; Pappas, C. G.; Liu, K.; Otto, S. Out-of-Equilibrium Self-Replication Allows Selection for Dynamic Kinetic Stability in a System of Competing Replicators. *Angew. Chem. Int. Ed.* **2022**, *61*, e202117605. DOI: https://doi.org/10.1002/anie.202117605.

[122] Saraswathy, M.; Gong, S. Different strategies to overcome multidrug resistance in cancer. *Biotechnol. Adv.* **2013**, *31* (8), 1397-1407. DOI: https://doi.org/10.1016/j.biotechadv.2013.06.004.

[123] Szakács, G.; Paterson, J. K.; Ludwig, J. A.; Booth-Genthe, C.; Gottesman, M. M. Targeting multidrug resistance in cancer. *Nat. Rev. Drug Discovery* **2006**, *5* (3), 219-234. DOI: https://doi.org/10.1038/nrd1984.

[124] Ye, Q.; Liu, K.; Shen, Q.; Li, Q.; Hao, J.; Han, F.; Jiang, R.-W. Reversal of Multidrug Resistance in Cancer by Multi-Functional Flavonoids. *Front. Oncol.* **2019**, *9*. DOI: https://doi.org/10.3389/fonc.2019.00487.

[125] Kathawala, R. J.; Gupta, P.; Ashby, C. R.; Chen, Z.-S. The modulation of ABC transporter-mediated multidrug resistance in cancer: A review of the past decade. *Drug Resistance Updates* **2015**, *18*, 1-17. DOI: https://doi.org/10.1016/j.drup.2014.11.002.

[126] Gottesman, M. M.; Fojo, T.; Bates, S. E. Multidrug resistance in cancer: role of ATP–dependent transporters. *Nat. Rev. Cancer* **2002**, *2* (1), 48-58. DOI: https://doi.org/10.1038/nrc706.

[127] Sarkadi, B.; Homolya, L.; Szakács, G.; Váradi, A. Human Multidrug Resistance ABCB and ABCG Transporters: Participation in a Chemoimmunity Defense System. *Physiol. Rev.* **2006**, *86* (4), 1179-1236. DOI: https://doi.org/10.1152/physrev.00037.2005.

[128] Subhan, M. A.; Attia, S. A.; Torchilin, V. P. Advances in siRNA delivery strategies for the treatment of MDR cancer. *Life Sci.* **2021**, *274*, 119337. DOI: https://doi.org/10.1016/j.lfs.2021.119337.

[129] Kesharwani, S. S.; Kaur, S.; Tummala, H.; Sangamwar, A. T. Overcoming multiple drug resistance in cancer using polymeric micelles. *Expert Opin. Drug Delivery* **2018**, *15* (11), 1127-1142. DOI: https://doi.org/10.1080/17425247.2018.1537261.

[130] Creixell, M.; Peppas, N. A. Co-delivery of siRNA and therapeutic agents using nanocarriers to overcome cancer resistance. *Nano Today* **2012**, *7* (4), 367-379. DOI: https://doi.org/10.1016/j.nantod.2012.06.013.

[131] Sun, H.; Yarovoy, I.; Capeling, M.; Cheng, C. Polymers in the Co-delivery of siRNA and Anticancer Drugs for the Treatment of Drug-resistant Cancers. *Top. Curr. Chem.* **2017**, *375* (2), 24. DOI: https://doi.org/10.1007/978-3-319-77866-2_12.

[132] Shen, J.; Zhang, W.; Qi, R.; Mao, Z.-W.; Shen, H. Engineering functional inorganic–organic hybrid systems: advances in siRNA therapeutics. *Chem. Soc. Rev.* **2018**, *47* (6), 1969-1995. DOI: https://doi.org/10.1039/C7CS00479F.

[133] Mirzavi, F.; Barati, M.; Soleimani, A.; Vakili-Ghartavol, R.; Jaafari, M. R.; Soukhtanloo, M. A review on liposome-based therapeutic approaches against malignant melanoma. *Int. J. Pharm.* **2021**, *599*, 120413. DOI: https://doi.org/10.1016/j.ijpharm.2021.120413.

[134] Cheng, Y.; Ji, Y. RGD-modified polymer and liposome nanovehicles: Recent research progress for drug delivery in cancer therapeutics. *Eur. J. Pharm. Sci.* **2019**, *128*, 8-17. DOI: https://doi.org/10.1016/j.ejps.2018.11.023.

[135] Liechty, W. B.; Kryscio, D. R.; Slaughter, B. V.; Peppas, N. A. Polymers for Drug Delivery Systems. *Annu. Rev. Chem. Biomol. Eng.* **2010**, *1* (1), 149-173. DOI: https://doi.org/10.1146/annurev-chembioeng-073009-100847

[136] Ghasemiyeh, P.; Mohammadi-Samani, S. Polymers Blending as Release Modulating Tool in Drug Delivery. *Front. Mater.* **2021**, *8*, 752813. DOI: https://doi.org/10.3389/fmats.2021.752813.

[137] Lyu, Y.; Wu, X.; Papageorgiou, A. C.; Yang, J.; Wang, X.; Qi, D.; Li, J. Dynamic covalent macrocycles co-delivering genes and drugs against drug-resistant cancer. *Cell Rep. Phys. Sci.* **2022**, *3* (11), 101150. DOI: https://doi.org/10.1016/j.xcrp.2022.101150.

[138] Mansfeld, F. M.; Feng, G.; Otto, S. Photo-induced molecular-recognition-mediated adhesion of giant vesicles. *Org. Biomol. Chem.* **2009**, *7* (20), 4289-4295. DOI: https://doi.org/10.1039/B910197G.

[139] Zhang, T.; Song, W.; Zhao, J.; Liu, J. Full Solution-Phase Synthesis of Acetyl Hexapeptide-3 by Fragments Coupling Strategy. *Ind. Eng. Chem. Res.* **2017**, *56* (41), 11697-11704. DOI: https://doi.org/10.1021/acs.iecr.7b03299.

[140] Aigouy, T.; Costeseque, P.; Sempere, R.; Senac, T.; Jaud, J.; Anglerot, D. *Acta Crystallogr.* **1995**, B 51, 55–61. DOI: https://doi.org/10.1107/S010876819400159X.

[141] Gulmez, F.; Yercan, A.; Kocaaga, B.; Guner, F. S. pH-sensitive castor oil/PEG-based polyurethane films for drug delivery. *J. Drug Delivery Sci. Technol.* **2021**, *61*, 102160. DOI: https://doi.org/10.1016/j.jddst.2020.102160.

[142] Motaali, S.; Pashaeiasl, M.; Akbarzadeh, A.; Davaran, S. Synthesis and characterization of smart N-isopropylacrylamide-based magnetic nanocomposites containing doxorubicin anti-cancer drug. *Artif. Cells, Nanomed., Biotechnol.* **2017**, *45* (3), 560-567. DOI: https://doi.org/10.3109/21691401.2016.1161640.

[143] Rao, Z.; Ge, H.; Liu, L.; Zhu, C.; Min, L.; Liu, M.; Fan, L.; Li, D. Carboxymethyl cellulose modified graphene oxide as pH-sensitive drug delivery system. *Int. J. Biol. Macromol.* **2018**, *107*, 1184-1192. DOI: https://doi.org/10.1016/j.ijbiomac.2017.09.096.

[144] Mura, S.; Nicolas, J.; Couvreur, P. Stimuli-responsive nanocarriers for drug delivery. *Nat. Mater.* **2013**, *12* (11), 991-1003. DOI: https://doi.org/10.1038/nmat3776.

[145] Kennedy, L.; Sandhu, J. K.; Harper, M.-E.; Cuperlovic-Culf, M. Role of Glutathione in Cancer: From Mechanisms to Therapies. *Biomolecules* **2020**, *10* (10), 1429. DOI: https://doi.org/10.3390/biom10101429.

[146] Wang, J.; Abbas, M.; Wang, J.; Spruijt, E. Selective amide bond formation in redox-active coacervate protocells. *Nat. Commun.* **2023**, *14*, 8492. DOI: https://doi.org/10.1038/s41467-023-44284-x.

[147] Tian, D.; Hao, R.; Zhang, X.; Shi, H.; Wang, Y.; Liang, L.; Liu, H.; Yang, H. Multi-compartmental MOF microreactors derived from Pickering double emulsions for chemo-enzymatic cascade catalysis. *Nat. Commun.* **2023**, *14*, 3226. DOI: https://doi.org/10.1038/s41467-023-38949-w.

[148] Weng, Y.; Song, Z.; Chen, C.-H.; Tan, H. Hybrid hydrogel reactor with metal–organic framework for biomimetic cascade catalysis. *Chem. Eng. J.* **2021**, *425*, 131482. DOI: https://doi.org/10.1016/j.cej.2021.131482.

[149] Singh, S.; Mukherjee, T. K. Coacervate-Based Plexcitonic Assembly toward Peroxidase-like Activity and Ultrasensitive Glucose Sensing. *ACS Appl. Mater. Interfaces* **2023**, *15*, 25524. DOI: https://doi.org/10.1021/acsami.3c02863.

[150] Jobdeedamrong, A.; Cao, S.; Harley, I.; Crespy, D.; Land-fester, K.; Caire da Silva, L. Assembly of biomimetic microreactors using caged-coacervate droplets. *Nanoscale* **2023**, *15*, 2561. DOI: https://doi.org/10.1039/D2NR05101J.

[151] Huang, H.; Fang, Y.; Weng, Y.; Liu, H. Mater. Photo-/electro-chromic underwater adhesive coacervate from self-assembly of zwitterions and polyoxometalate. *Today Chem*. **2023**, *32*, 101670. DOI: https://doi.org/10.1016/j.mtchem.2023.101670.

[152] Tang, J.; Yao, C.; Gu, Z.; Jung, S.; Luo, D.; Yang, D. Super-Soft and Super-Elastic DNA Robot with Magnetically Driven Navigational Locomotion for Cell Delivery in Confined Space. *Angew. Chem. Int. Ed.* **2020**, *59*, 2490. DOI: https://doi.org/10.1002/ange.201913549.

[153] Teo, M. Y.; Kee, S.; RaviChandran, N.; Stuart, L.; Aw, K. C.; Stringer, J. Enabling Free-Standing 3D Hydrogel Microstructures with Microreactive Inkjet Printing. *ACS Appl. Mater. Interfaces* **2020**, *12*, 1832. DOI: https://doi.org/10.1021/acsami.9b17192.

[154] Liu, H.-T.; Wang, H.; Wei, W.-B.; Liu, H.; Jiang, L.; Qin, J.-H. A Microfluidic Strategy for Controllable Generation of Water-in-Water Droplets as Biocompatible Microcarriers. *Small* **2018**, *14*, 1801095. DOI: https://doi.org/10.1002/smll.201801095.

[155] Morimoto, Y.; Kiyosawa, M.; Takeuchi, S. Three-dimensional printed microfluidic modules for design changeable coaxial microfluidic devices. *Sens. Actuators, B* **2018**, *274*, 491. DOI: https://doi.org/10.1016/j.snb.2018.07.151.

[156] Yu, J.; Park, S. A.; Kim, W. D.; Ha, T.; Xin, Y. Z.; Lee, J.; Lee, D. Current Advances in 3D Bioprinting Technology and Its Applications for Tissue Engineering. *Polymers* **2020**, *12*(12), 2958. DOI: https://doi.org/10.3390/polym12122958.

[157] Michaeli, I.; Overbeek, J. T. G.; Voorn, M. J. Phase separation of polyelectrolyte solutions. *J. Polym. Sci.* **1957**, *23*, 443. DOI: https://doi.org/10.1002/pol.1957.1202310337.

[158] Yewdall, N. A.; André, A. A. M.; Lu, T.; Spruijt, E. Coacervates as models of membraneless organelles. *Curr. Opin. Colloid Interface Sci.* **2021**, *52*, 101416. DOI: https://doi.org/10.1016/j.cocis.2020.101416.

[159] Sing, C. E.; Perry, S. L. Recent progress in the science of complex coacervation. *Soft Matter* **2020**, *16*, 2885. DOI: https://doi.org/10.1039/D0SM00001A.

[160] Taylor, P. Ostwald ripening in emulsions: estimation of solution thermodynamics of the disperse phase. *Adv. Colloid Interface Sci.* **2003**, *106*, 261. DOI: https://doi.org/10.1016/S0001-8686(03)00113-1.

[161] Leal-Calderon, F.; Poulin, P. Progress in understanding emulsion metastability and surface forces. *Curr. Opin. Colloid Interface Sci.* **1999**, *4*, 223. DOI: https://doi.org/10.1016/S1359-0294(99)00038-2.

[162] Kabalnov, A. Ostwald Ripening and Related Phenomena. *J. Dispersion Sci. Technol.* **2001**, *22*, 1. DOI: https://doi.org/10.1081/DIS-100102675.

[163] Zwicker, D.; Hyman, A. A.; Jülicher, F. Suppression of Ostwald ripening in active emulsions. *Phys. Rev. E* **2015**, *92*, 012317. DOI: https://doi.org/10.1103/PhysRevE.92.012317.

[164] Donau, C.; Boekhoven, J. The chemistry of chemically fueled droplets. *Trends Chem*. **2023**, *5*, 45. DOI: https://doi.org/10.1016/j.trechm.2022.11.003.

[165] Bergmann, A. M.; Bauermann, J.; Bartolucci, G.; Donau, C.; Stasi, M.; Holtmannspötter, A.-L.; Jülicher, F.; Weber, C. A.; Boekhoven, J. Liquid spherical shells are a non-equilibrium steady state of active droplets. *Nat. Commun.* **2023**, *14*, 6552. DOI: https://doi.org/10.1038/s41467-023-42344-w.

[166] Ping, Z. H.; Nguyen, Q. T.; Chen, S. M.; Zhou, J. Q.; Ding, Y. D. States of water in different hydrophilic polymers-DSC and FTIR studies. *Polymer* **2001**, *42*, 8461. DOI: https://doi.org/10.1016/S0032-3861(01)00358-5.

[167] Li, W.; Xue, F.; Cheng, R. States of water in partially swollen poly(vinyl alcohol) hydrogels. *Polymer* **2005**, *46*, 12026. DOI: https://doi.org/10.1016/j.polymer.2005.09.016.

[168] Kujawa, W.; Olewnik-Kruszkowska, E.; Nowaczyk, J. Concrete Strengthening by Introducing Polymer-Based Additives into the Cement Matrix-A Mini Review. *Materials* **2021**, *14*(20), 6071. DOI: https://doi.org/10.3390/ma14206071.

TURUN
YLIOPISTO
UNIVERSITY
OF TURKU

Painosalama, Turku, Finland 2024

ISBN 978-951-29-9830-2 (PRINT)
ISBN 978-951-29-9831-9 (PDF)
ISSN 0082-7002 (Print)
ISSN 2343-3175 (Online)